NTNU

Norwegian University of
Science and Technology

Electrochemical characterization of $YMnO_3$ in alkaline solution

Identifying the characteristic voltammogram
and developing the experimental procedure

Kristian Fredrik
Thorbjørnsen

Chemical Engineering and Biotechnology
Submission date: June 2016
Supervisor: Sverre Magnus Selbach, IMTE
Co-supervisor: Svein Sunde, IMTE
Didrik Småbråten, IMTE

Norwegian University of Science and Technology
Department of Materials Science and Engineering

Preface

The work in this thesis was carried out at the Norwegian University of Science and Technology (NTNU). The work is a continuation of the materials science specialization project fall 2015, and was carried out between January and June 2016. The idea behind the project was proposed by Associate Professor Sverre M. Selbach, and is based on the work of Bergum et al. (*Dalton Transactions* 2011)[1], Mefford et al. (*Nature Materials* 2014)[2], Nesdal (2013)[3], Frydenlund (2014)[4] and Reidulf (2014)[5]. The experimental work was performed by the author. Since this work is a continuation of the specialization project[6], parts of the literature review have been reused and improved. Originally, the aim of this work was to electrochemically characterize $YMnO_3$ in alkaline solution. However, due to complications in the experimental work, significant time and effort was devoted into developing the method itself.

Acknowledgements

I want to thank my supervisors, associate professor Sverre M. Selbach, professor Svein Sunde and PhD candidate Didrik Småbråten for providing me with guidance. I also want to thank staff engineers Magnus B. Følstad and Anita Storsve, senior engineers Kristin Høydalsvik and Yingda Yu and PhD candidate Thomas Holm for helping me in the lab. I want to thank professor Ann Mari Svensson and associate professor Frode Seland for answering any question I had, thus helping me develop my experimental setup. I also want to thank research scientist Julian R. Tolchard from Sintef for answering any question I had whenever I met him in the hallways. My final thank you goes to the ceramic oxides group for providing feedback on my presentations.

Trondheim
June 17, 2016

Kristian Fredrik Klepp Thorbjørnsen

Abstract

Electrochemical intercalation of oxygen into oxide structures has been studied ever since it was first observed in 1990[7]. A recent paper investigated using electrochemical intercalation of oxygen into vacancies in $LaMnO_3$ for charge storage and pseudocapacitive applications[2]. It was found that oxygen was inserted into the structure via a redox reaction. The findings offered a new paradigm for electrochemical charge storage. Hexagonal manganites have attracted a lot of attention the past years due to their multiferrioc properties and tailorable defect-chemistry. The hexagonal manganite $YMnO_3$ has a significant potential for electrochemical storage of oxygen due to the possibility for incorporation of highly mobile interstitial oxygen anions into the lattice. The combination of oxygen vacancies and highly mobile interstitial species could give even better pseudocapacitive properties than $LaMnO_3$.

In order to electrochemically characterize $YMnO_3$, an electrode with $YMnO_3$ has to be prepared. This work investigated different electrode preparation methods, as well as the electrochemical response from each electrode prepared. Previous work showed unstable electrochemical measurements as well as poor reproducibility that could be attributed to the electrode. Deposition of particles as a thin film onto a glassy carbon rotating disc electrode suffers from poor adhesion between the glassy carbon substrate and the film. In this work, both bulk and nanocrystalline particles of titanium-doped $YMn_{1-x}Ti_xO_{3\pm\delta}$ as well as nanoparticles of $YMnO_3$ loaded onto mesoporous carbon was used to evaluate the rotating disc electrode setup. This setup was compared to an inverted setup where gravity was used to improve the contact force between particles and glassy carbon. The adhesive properties between glassy carbon and the thin films were qualitatively evaluated, and the electrochemical response was measured using cyclic voltammetry. The resulting voltammograms were separated into their faradic and non-faradic components, and the different methods were evaluated as to whether a redox reaction had been observed. We also investigated whether a sintered pellet in a flat specimen electrode could be used instead of particles deposited on a substrate. A thin film did not adhere sufficiently well to the glassy carbon surface. We attempted to use unmodified Nafion™ as a binder, but as expected this membrane was incompatible with the alkaline solution. Although no definite conclusion could be made as to whether oxygen intercalation occurred, the electrochemical response was promising. We concluded that the voltammogram of $YMnO_3$ in alkaline solution is characterized by one oxidation peak and two reduction peaks. The inverted setup is suitable for purely electrochemical characterization, but due to the lack of adhesion between the thin films and the glassy carbon substrate, we conclude that a pellet mounted in a flat specimen electrode should be used for further work. From this, a comprehensive suggestion for further work is presented.

Sammendrag

Elektrokjemisk interkalering av oksygen inn i oksider har vært studert helt siden det ble observert for første gang i 1990[7]. Det ble funnet at oksygen ble interkalert inn i strukturen via en redox-reaksjon. En nylig publisert studie undersøkte muligheten for å utnytte elektrokjemisk interkalering av oksygen inn i vakanser i $LaMnO_3$ til ladningslagring og pseudokapasitive formål. Funnene åpnet opp et nytt paradigme for elektrokjemisk ladningslagring. Heksagonale manganitter har fått mye oppmerksomhet de siste årene grunnet deres multiferroiske egenskaper og justerbare defektkjemi. Den heksagonale manganitten $YMnO_3$ har et stort potensiale for elektrokjemisk ladningslagring grunnet evnen til å inkorporere meget mobile interstitielle oksygenioner i strukturen. Kombinasjonen og oksygenvakanser og mobile interstitielle ioner kan potensielt gi enda bedre pseudokapasitive egenskaper enn $LaMno_3$.

For å karakterisere $YMnO_3$ elektrokjemisk må en elektrode med $YMnO_3$ prepareres. Dette arbeidet har undersøkt ulike måter å preparere en elektrode, samt den elektrokjemiske responsen fra hver elektrode. Tidligere arbeid har vist ustabile målinger og lav reproduserbarhet, som muligens kan skyldes elektroden. Deponering av partikler som en tynn film på en roterende disk-elektrode av glasskarbon lider av dårlig heft mellom karbonet og filmen. I dette arbeid har både bulk og nanokrystalline partikler av $YMn_{1-x}Ti_xO_{3\pm\delta}$, samt nanopartikler av $YMnO_3$ iblandet mesoporøst karbon blitt brukt til å undersøke bruk av en roterende disk-elektrode. Denne typen elektrode ble sammenligned med et oppned-oppsett hvor tyngdekraften forbedret kontaktkraften mellom tynnfilmen og glasskarbonet. Heften mellom glasskarbonet og tynnfilmene ble vurdert kvalitativt, og den elektrokjemiske responsen ble målt med syklisk voltammetri. De resulterende voltammogrammene ble separert inn i faradiske og ikke-faradiske komponenter, og de ulike metodene ble vurdert med tanke på om en redoksreaksjon hadde funnet sted. Det ble også undersøkt om en sintret pellet av $YMn_{1-x}Ti_xO_{3\pm\delta}$ festet i en flat-prøve prøveholder kunne brukes som elektrode i stedet for partikler deponert på et substrat. Tynnfilmene hadde for lav heft til glasskarbonet. Det ble prøvd å bruke umodifisert Nafion™ som bindemiddel, men som forventet var ikke membranen kompatibel med den basiske løsningen. Vi kan ikke med sikkerhet konkludere om interkalering av oksygen ble observert, men den elektrokjemiske responsen var lovende. Vi konkluderte med at det sykliske voltammogrammet til $YMnO_3$ i basisk løsning kan kjennetegnes ved en oksidasjonstopp og to reduksjonstopper. Det inverterte oppsetter er egnet for ren elektrokjemisk karakterisering, men grunnet den manglende heften mellom glasskarbonet og tynnfilmen konkluderer vi med at en pellet fested i en flat-prøve prøveholder burde brukes til videre arbeid. Ut i fra dette presenteres det et detaljert forslag til videre arbeid.

List of abbreviations

All abbreviations used in this work are given in Table 1, in alphabetical order.

Table 1: List of abbreviations used in this work.

Abbreviation	Meaning
Ag/AgCl	Silver chloride reference electrode
CE	Counter electrode
CV	Cyclic voltammetry
EDS	Energy-dispersive X-ray spectroscopy
GC	Glassy carbon
MC	Mesoporous carbon
RDE	Rotating disc electrode
RE	Reference electrode
SEM	Scanning electron microscope
ST3	Starbon™300
ST8	Starbon™800
TGA	Thermogravimetric analysis
WE	Working electrode
XPS	X-ray photo-electron spectroscopy
XRD	X-ray diffraction

Contents

Chapter 1

Introduction

Supercapacitors fill the void between batteries and traditional electrostatic capacitors in terms of power- and energy density, and are divided into either electrical double-layer capacitors or pseudocapacitors. Electrical double-layer capacitors typically have a very large specific capacity, thanks to materials such as high area carbon powders[8]. Metal oxides such as RuO_2, MnO_2 and $Ni(OH)_2$ display high pseudocapacitance, with an energy density of up to an order of magnitude higher than the electrical double-layer carbon counterparts. This is thanks to fast reversible redox reactions at the electrode-electrolyte interface[2].

The mechanism behind electrochemical charge storage by reversible cation intercalation have been widely studied and is a well-known phenomenon[9], used in e.q. rechargeable batteries. Electrochemical oxidation and reduction of perovskites and related structures has been researched since before 1975[10], and in 1996 it was confirmed that the surface exchange of oxygen also extended into the bulk of the material[7]. Although oxygen intercalation is a known phenomenon, it has typically only been used for synthesis of highly oxidized materials[2, 11]. A recent paper [2] investigated the possibility of utilizing intercalation of oxygen for electrochemical charge storage in the perovskite $LaMnO_3$. The findings opened up a new paradigm for electrochemical charge storage.

In a perovskite such as $LaMnO_3$, for which the dominating point defects are oxygen vacancies, oxygen intercalation occurs by incorporation of oxygen into vacant sites with a corresponding oxidation of manganese. The capacity for oxygen storage is then given by the number of available oxygen sites, and the charge/discharge-rate is limited by the diffusion rate of oxygen species. In contrast to the perovskite polymorphs, hexagonal manganites such as $YMnO_3$ also have the possibility for incorporation of highly mobile interstitial oxygen species into the structure. The potential for a higher oxygen capacity as well as diffusion rate makes $YMnO_3$ a promising candidate for pseudocapacitive applications.

Based on [2], it was in previous work attempted to characterize nanocrystalline particles of $YMnO_3$ loaded onto mesoporous carbon by cyclic voltammetry in KOH. The particles were deposited onto a glassy carbon rotating disc electrode as a thin film. The results were promising, though inconclusive. It appeared that the thin film did not adhere well to the glassy carbon surface, and that modifications to the method had to be done. Normally, Nafion™ would be used as a binder between the glassy carbon substrate and the thin film. However, Nafion™ will block anion transport in highly alkaline conditions, rendering its usage counter-productive Other alternatives exist, but the use of solvents like NMP will be avoided in this thesis in order to reduce the usage of toxic substances. An adequately small amount of Nafion™ could, however, provide sufficient adhesive properties whilst at the same time leaving most of the active surface in contact with the electrolyte.

Aim of work

The aim of this work is to electrochemically characterize $YMnO_3$ in alkaline solution. Electrodes of $YMnO_3$ will be prepared by different methods, and the electrochemical response will be measured using cyclic voltammetry. Both thin film methods and sintered pellets will be evaluated. The ultimate goal is to identify the characteristic voltammogram of $YMnO_3$ in KOH, and to suggest a detailed plan for further work. Even though $YMnO_3$ is used in this work, the results can be transferred over to other materials, as the same principles apply. Due to the improved properties when doping $YMnO_3$ with Ti^{4+}, both mechanical and electrical, $YMn_{1-x}Ti_xO_{3\pm\delta}$ will also be used.

Chapter 2

Literature review

2.1 Crystal structure

$YMnO_3$ belongs to a class of ternary manganites, $RMnO_3$ (R = Y, Sc, In, Ho,...,Lu)[1], which will crystallize into either an orthorhombic perovskite or a hexagonal phase. The hexagonal and orthorhombic polymorphs lie close in Gibbs energy, thus the phase obtained during synthesis depends on synthesis conditions and the R-cation[1]. The $RMnO_3$-manganites are stable in the perovskite phase for $0.855 < t < 1$, and in the hexagonal phase for $t < 0.855$[12]. At ambient conditions $YMnO_3$ will crystallize into the hexagonal phase with space group $P6_3cm$[1]. The tolerance factor of orthorhombic $YMnO_3$ can be calculated using Equation (2.1).

$$t = \frac{r_Y + r_O}{\sqrt{2}(r_{Mn} + r_O)} \tag{2.1}$$

If orthorhombic $YMnO_3$ is evaluated using the Shannon radii for 6-coordinated high spin Mn^{3+} and 8-coordinated Y^{3+}[13] [(a)], the tolerance factor is $t = 0.836$, which corresponds to the hexagonal phase being the most stable. Oxidation of Mn^{3+} to Mn^{4+} will decrease the ionic radius from 0.645 Å to 0.53 Å, shifting the tolerance factor towards $t = 0.886$. Crystallization in an oxygen atmosphere has been shown to yield the orthorhombic rather than hexagonal phase[14]. However, if the hexagonal phase had already been formed, annealing would not yield the orthorhombic phase. The same work evaluated the tolerance factor using a modified approach. The radii for 9-coordinated A-site cations was used to calculate the corresponding tolerance factor $t_9 = 0.86$[14].

The hexagonal phase can be described as Y^{3+} that are 7-coordinated by oxygen, placed between layers of MnO_5 trigonal bipyramids as seen in Figure 2.1. Y^{3+} is asymmetrically displaced along the c-axis. The MnO_5 trigonal bipyramids are tilted with respect to the c-axis and ab-plane[1]. Mn^{3+} is coordinated by three in-plane, and two apical oxygen ions[1]. At elevated temperatures, above 1250 K, the symmetry is increased so that all the MnO_5 bipyramids are aligned along the c-axis and all the Y^{3+} are aligned in the ab-plane, with a corresponding change in space group from $P6_3cm$ to the centrosymmetric $P6_3/mmc$[15].

[(a)] $r_{Y^{3+}} = 1.019$, $r^{HS}_{Mn^{3+}} = 0.645$, $r_{O^{2-}} = 1.4$

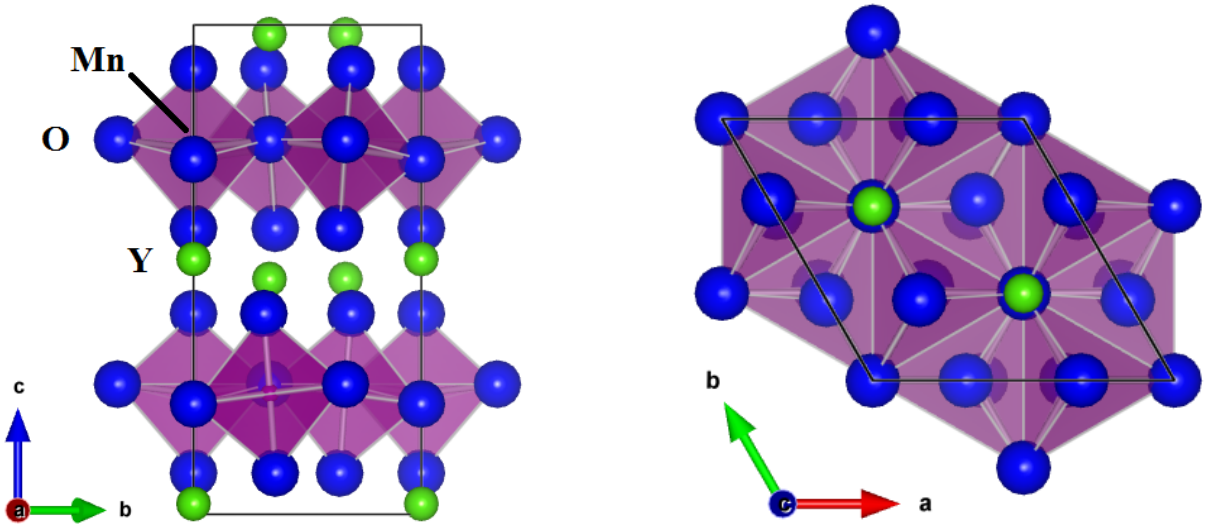

(a) $YMnO_3$ as seen from the a-direction

(b) $YMnO_3$ as seen from the c-direction

Figure 2.1: $YMnO_3$ may be described as alternating layers of Y^{3+}(green) and corner-sharing MnO_5 trigonal bipyramids. The hexagonal structure is clearly visualized in Figure 2.1b. Images generated by VESTA [16].

2.2 Phase composition and stability

Although no precise phase diagram exist, a theoretical one has been constructed from thermodynamical calculations[17]. Figure 2.2 indicates that hexagonal $YMnO_3$ is stable between 1062 K and 2067 K. At T =2067 K, it will melt incongruently to a liquid and $\alpha-Y_2O_3$. Below a temperature of 1062 K, hexagonal $YMnO_3$ should decompose into YMn_2O_5 and Y_2O_3. However, it is kinetically stabilized at low temperatures because the cation mobility is insufficient for phase decomposition, as this requires diffusion of cation species. Hence, the hexagonal phase of $YMnO_3$ is metastable.

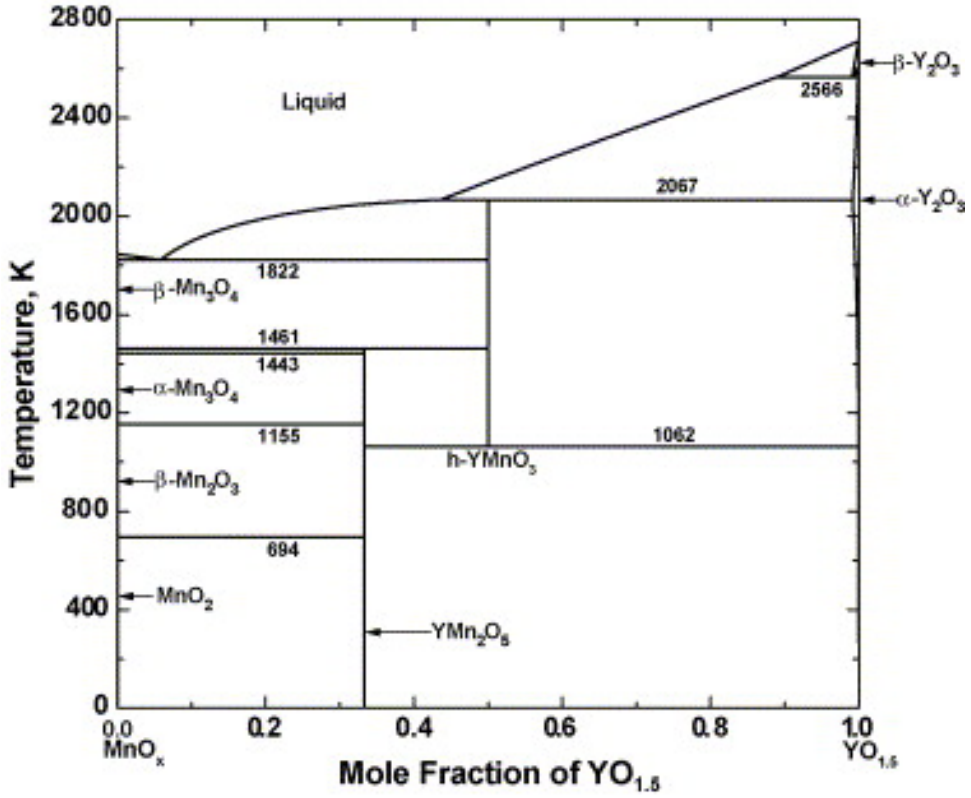

Figure 2.2: Phase diagram of the Mn-Y-O system. Created by [17], from thermodynamical calculations.

The lack of an experimentally constructed phase diagram is followed up my the same lack of a pourbaix diagram. Although a pourbaix diagram for $YMnO_3$ do not exist, that of manganese in Figure 2.3[18], may be used to evaluate the behaviour in alkaline conditions when a potential is applied. At $E = 0$V, synthesis conditions can be used to evaluate the stability. Hexagonal $YMnO_3$ can be synthesized by hydrothermal synthesis, and has previously been synthesized phase pure with 2.5M sodium hydroxide as mineralizer[19]. $LaMnO_3$ has been electrochemically characterized in KOH up to 6M[2]. Other manganites has also been synthesized in alkaline conditions[19]. Thus, hexagonal $YMnO_3$ should be stable even at high pH values. At negative potentials however, hydroxide ions may be adsorbed.

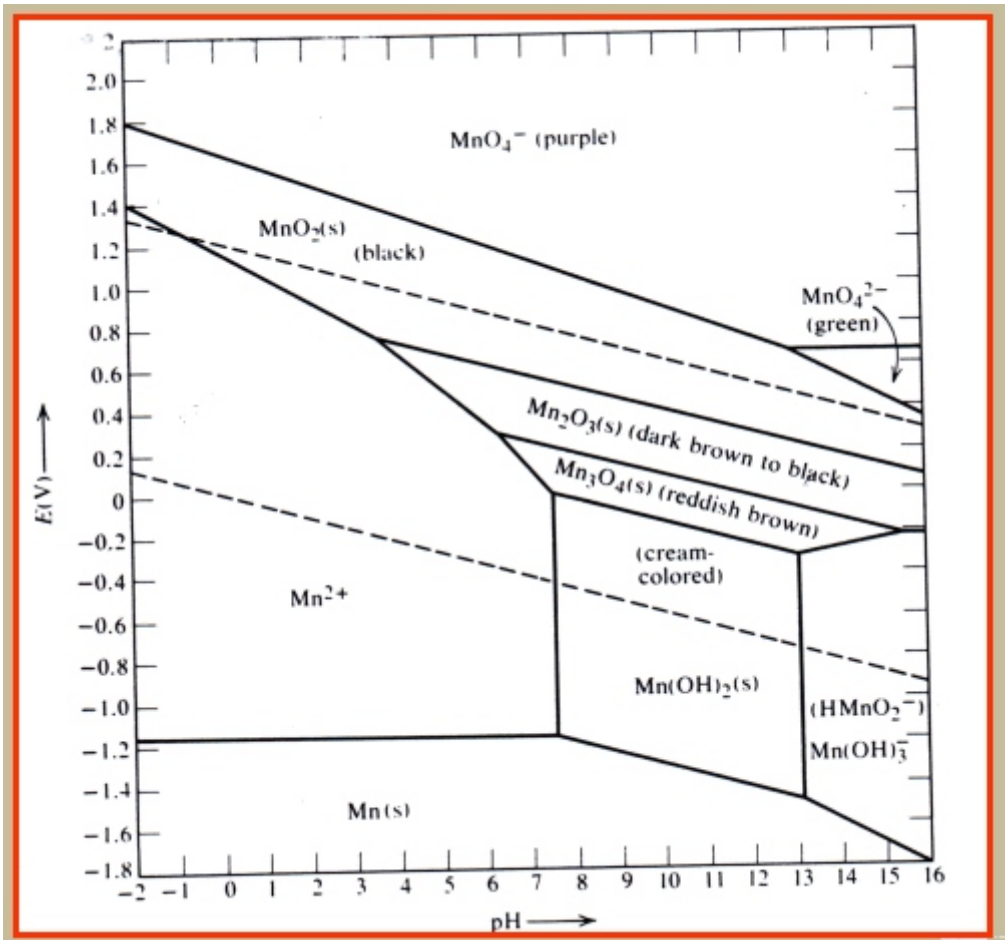

Figure 2.3: A pourbaix-diagram for manganese. Potential is versus a standard hydrogen electrode. Taken from [18]

2.3 Band structure and conductivity

$YMnO_3$ is an insulator with a band gap of 1.5 eV[20], an electrical conductivity around $10^{-6}\,Scm^{-1}$ and an activation energy for electronic conduction of 0.36 eV[21] . The electron structure of Y^{3+} is that of empty $4d$ and $5s$ orbitals, whereas the $4s$ and $4p$ orbitals are full ($4s^2 4p^6 4d^0$)[22]. Mn^{3+} is characterized by a partially filled $3d$ orbital ($3d^4 4s^0$)[22]. In the hexagonal phase, Mn^{3+} is in a trigonal bipyramidal configuration, with a corresponding crystal field splitting as shown in Figure 2.4a. Both the d_{xz} and d_{yz} orbitals are directed in between O^{2-} ions and are quite localized. The d_{xy} and $d_{x^2-y^2}$ orbitals are less localized and slightly higher in energy. The empty d_{z^2} orbital which are pointed directly at O^{2-} is fairly localized due to the tilting and displacements in $P6_3cm$ [23].

The mechanism behind electronic conductivity in $YMnO_3$ is proposed to be thermally activated polaron hopping at low temperatures, and migration of oxygen vacancies at higher temperatures[24]. In polaron hopping, a small polaron is transferred between two adjacent Mn^{3+} and Mn^{4+} as shown in Figure 2.4b.

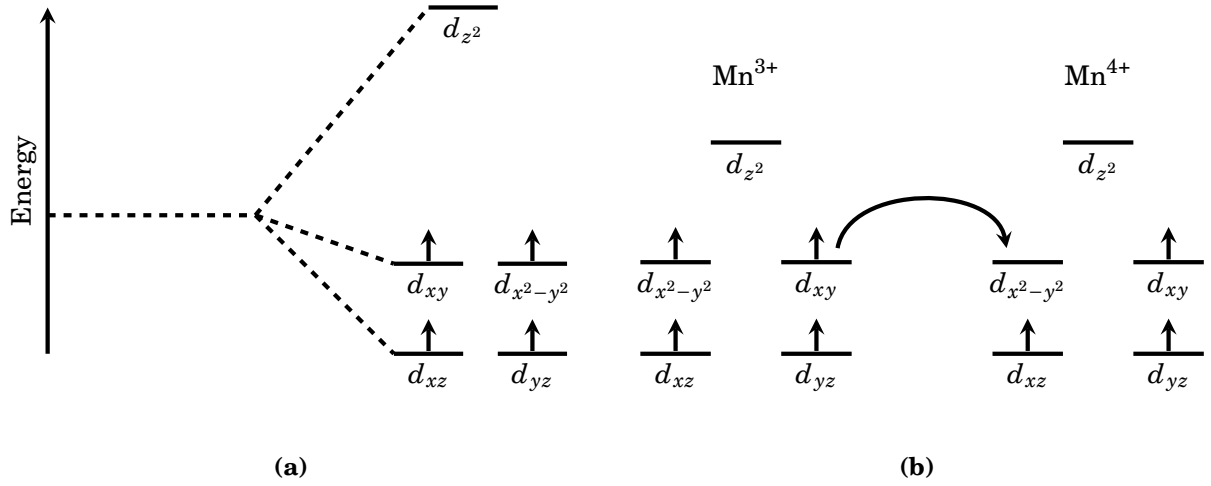

Figure 2.4: Sketch of the trigonal bipyramidal crystal-field splitting of Mn^{3+} in $YMnO_3$ (**a**), and the corresponding polaron-hopping between adjacent Mn^{3+} and Mn^{4+} (**b**).

Since Mn^{3+} can be both reduced and oxidized, the conductivity of $YMnO_3$ can be adjusted to both n- and p-type. An oxidized manganese specie may be viewed as a hole which will induce p-type conductivity, as in Equation (2.2)[3].

$$Mn^{\bullet}_{Mn} \longrightarrow h^{\bullet} + Mn^{x}_{Mn} \tag{2.2}$$

A reduced manganese specie may be viewed as an electron that induces n-type conductivity, as in Equation (2.3).

$$Mn^{'}_{Mn} \longrightarrow e^{-} + Mn^{x}_{Mn} \tag{2.3}$$

The conductivity can be adjusted towards both n- and p-type by atmosphere control, doping or both, as will be elaborated further in Section 2.4. It has been reported electrical conductivity up to $2 \times 10^{-3}\,Scm^{-1}$ at 400 °C for Ti^{4+} content of x= 0.15 in $YMn_{1-x}Ti_xO_3$[25] and $3.23 \times 10^{-2}\,Scm^{-1}$ at 20 °C for Ca^{2+} content of x= 0.20 in $Y_{1-x}Ca_xMnO_3$[21].

2.4 Defect Chemistry

Due to thermodynamic considerations, all crystalline materials contain imperfections (defects). Gibbs free energy is minimized at a defect concentration above zero. Hence, there is an equilibrium concentration of defects that increases with temperature[26, page 84]. If the imperfection is limited to one structural or lattice site and its immediate vicinity, it is termed a point defect. Both point, line and planar defects exist. Point defects are the vacancy or miss-placement of one or more ions in the lattice, as in Figure 2.5. This may be used to tailor the functional properties of oxide ceramics.

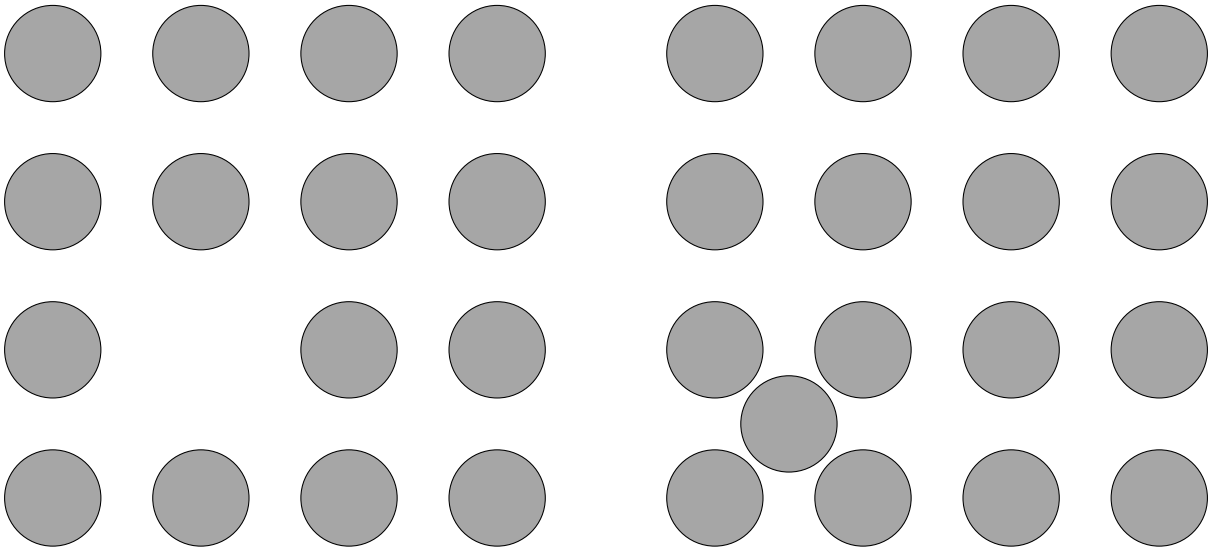

(a) Vacant site **(b)** Interstitial species

Figure 2.5: Principle sketch of a vacant site (2.5a) and an interstitial specie (2.5b)

2.4.1 Intrinsic defects

Metal oxides where one or more of the cations can be oxidized and/or reduced may exhibit oxygen non-stoichiometry. In $YMnO_3$, both oxygen excess and deficiency is possible. Due to the inherent existence of defects, even stoichiometric $YMnO_3$ will have point defects. The following Sections 2.4.1 and 2.4.1 will elaborate further into the intrinsic defect chemistry of $YMnO_3$.

Oxygen vacancies

The loss of oxygen due to e.q. a low partial oxygen pressure as in Equation (2.4) will change the stoichiometry of the material. This also includes the stoichiometry of negative and positive charges. As demonstrated by the Kröger-Vink notation in Equation (2.5), the loss of oxygen will be compensated for by the reduction of two manganese centers.

$$YMnO_3 \overset{YMnO_3}{\rightleftharpoons} \frac{\delta}{2} O_2(g) + YMnO_{3-\delta} \tag{2.4}$$

$$O_O^x + 2Mn_{Mn}^x \overset{YMnO_3}{\rightleftharpoons} \frac{1}{2} O_2(g) + V_O^{\bullet\bullet} + 2Mn_{Mn}^{'} \tag{2.5}$$

Combining Equations (2.4) and (2.5) gives Equation (2.6).

$$YMnO_3 \overset{YMnO_3}{\rightleftharpoons} Y\left[Mn_{(1-2\delta)}Mn'_{2\delta}\right]O_{(3-\delta)} + \frac{\delta}{2}O_2(g) \tag{2.6}$$

The corresponding equilibrium constant may be expressed as:

$$K_{V_O} = p_{O_2}^{1/2}\left[V_O^{\bullet\bullet}\right]\left[Mn'_{Mn}\right]^2 \tag{2.7}$$

Interstitial oxygen

The same should be true for interstitial oxygen. The net negative charge provided by an interstitial oxygen should be compensated for by oxidation of manganese, as shown by Equation (2.8), written in Kröger-Vink notation in Equation (2.9)

$$YMnO_3 + \frac{\delta}{2}O_2(g) \overset{YMnO_3}{\rightleftharpoons} YMnO_{3+\delta} \tag{2.8}$$

$$\frac{1}{2}O_2(g) + 2Mn^x_{Mn} \overset{YMnO_3}{\rightleftharpoons} O_i'' + 2Mn^{\bullet}_{Mn} \tag{2.9}$$

One interstitial oxygen corresponds to two oxidized manganese, which results in Equation (2.10).

$$YMnO_3 + \frac{\delta}{2}O_2(g) \overset{YMnO_3}{\rightleftharpoons} Y\left[Mn_{(1-2\delta)}Mn^{\bullet}_{2\delta}\right]O_{(3+\delta)} \tag{2.10}$$

The corresponding equilibrium constant may be written as in Equation (2.11):

$$K_{O_i} = \frac{\left[O_i''\right]\left[Mn^{\bullet}_{Mn}\right]^2}{p_{O_2}^{1/2}} \tag{2.11}$$

Oxygen frenkel defect

An oxygen ion may also leave the lattice and appear in an interstitial site, as in Equation (2.12). This vacancy-interstitial pair is known as a frenkel defect.

$$O^x_O \rightleftharpoons O_i'' + V_O^{\bullet\bullet} \tag{2.12}$$

The corresponding equilibrium constant would be as in Equation (2.13)

$$K_{O_f} = \left[O_i''\right]\left[V_O^{\bullet\bullet}\right] \tag{2.13}$$

Cation vacancies

It has been shown[27] that oxygen excess in $LaMnO_{3+\delta}$ can be expressed in terms of cation vacancies, as in Equation (2.14), where $\gamma = \frac{\delta}{3+\delta}$.

$$LaMnO_3 + \frac{\delta}{2}O_2(g) \overset{LaMnO_3}{\rightleftharpoons} La_{1-\gamma}Mn_{1-\gamma}O_3 \tag{2.14}$$

If this is assumed to be true for $YMnO_3$, then the intercalation of oxygen may be viewed as the formation of cation vacancies, as in Equation (2.15)

$$YMnO_3 + \frac{\delta}{2}O_2(g) \overset{YMnO_3}{\rightleftharpoons} Y_{1-\gamma}Mn_{1-\gamma}O_3 \tag{2.15}$$

However, this would only be true for the incorporation of oxygen into lattice sites. The excess oxygen may be though of as an expansion of the lattice, with the corresponding vacant cation sites. For the formation of interstitial oxygen which enters in between lattice sites, an expression for such will be as in Equation (2.10).

Depending on the surrounding atmosphere, the charge generated by a cation vacancy may be compensated for by either oxidation of manganese or the formation of oxygen vacancies. In oxidizing conditions, as would be provided by a high oxygen partial pressure, the amount of oxygen vacancies formed is small. This can be seen from Equation (2.7). Charge should then be compensated by oxidation of manganese as written in Kröger-Vink notation in Equation (2.16).

$$\frac{1}{2}Mn_2O_3 + 2\,Mn_{Mn}^{x} + \frac{3}{4}(g) \overset{YMnO_3}{\rightleftharpoons} V_Y^{'''} + 3\,Mn_{Mn}^{\bullet} + 3\,O_O^{x} \tag{2.16}$$

As for the opposite case, charge compensation in a reducing atmosphere should occur by oxygen vacancy formation, as in Equation (2.17).

$$\frac{1}{2}Mn_2O_3 \overset{YMnO_3}{\rightleftharpoons} V_Y^{'''} + \frac{3}{2}V_O^{\bullet\bullet} + \frac{3}{2}O_O^{x} + Mn_{Mn}^{x} \tag{2.17}$$

2.4.2 n-doping

Substitution of the manganese-site in $YMnO_3$ by a higher valency cation, e.g. Ti^{4+}, will generate a formal positive charge. The surpluss charge will be compensated by either interstitial oxygen, cation vacancies or reduction of manganese, depending on synthesis conditions. The Kröger-Vink notation for such is shown in Equations (2.18) to (2.20), respectively.

$$2\,TiO_2 \xrightarrow{YMnO_3} 2\,Ti_{Mn}^{\bullet} + 3\,O_O^{x} + O_i^{''} \tag{2.18}$$

$$3\,TiO_2 \xrightarrow{YMnO_3} 3\,Ti_{Mn}^{\bullet} + 6\,O_O^{x} + V_{Mn}^{'''} \tag{2.19}$$

$$TiO_2 + \frac{1}{2}Mn_2O_3 \xrightarrow{YMnO_3} Ti_{Mn}^{\bullet} + Mn_{Mn}^{'} + 3\,O_O^{x} + \frac{1}{4}O_2(g) \tag{2.20}$$

Although theoretically possible, the formation of cation vacancies is unlikely. As seen in Equation (2.3), the reduction of manganese will generate n-type conductivity, which may be achieved by e.q. heat treating the doped material in a reducing atmosphere. The specific case of Ti^{4+} substitution will be elaborated further in Section 2.5.

2.4.3 p-doping

Doping with a lower valency cation, e.g. Ca^{2+}, will generate a formal negative charge. Charge compensation will occur through anion vacancies, interstitial cations or oxidation of manganese, depending on synthesis conditions. By evaluation of the Shannon radii[13], it is assumed that

Ca^{2+} will enter the Y^{3+} sites. The Kröger-Vink notation for said possibilities is shown in Equations (2.21) to (2.23), respectively.

$$2\,CaO \xrightarrow{YMnO_3} 2\,Ca_Y^{'} + 2\,O_O^x + V_O^{\bullet\bullet} \tag{2.21}$$

$$3\,CaO \xrightarrow{YMnO_3} 2\,Ca_Y^{'} + 3\,O_O^x + Ca_i^{\bullet\bullet} \tag{2.22}$$

$$CaO + \frac{1}{2}Mn_2O_3 + \frac{1}{4}O_2(g) \xrightarrow{YMnO_3} Ca_Y^{'} + 3\,O_O^x + Mn_{Mn}^{\bullet} \tag{2.23}$$

The formation of interstitial cations is in principle possible, but highly unlikely. It has been reported a phase transition from the hexagonal to the orthorhombic phase when the Ca^{2+} content exceeds $x = 0.22$ in $Y_{1-x}Ca_xMnO_3$ [21]. This is in agreement with the larger ionic radii of 8-coordinated Ca^{2+} compared to Y^{3+}[(b)] , which will increase the tolerance factor towards the orthorhombic phase. If the formation of oxygen vacancies are unfavoured, as in oxidizing conditions, the lower valency of Ca^{2+} should be compensated by oxidation of Mn^{3+} to Mn^{4+}, further shifting the material towards the orthorhombic phase. In agreement with Equation (2.2),the oxidation of manganese creates p-type conductivity.

2.4.4 Yttrium deficiency

In an yttrium deficit sample if $YMnO_3$, the charge compensation for the missing yttrium would have to come from either oxidation of manganese or the formation of oxygen vacancies, as in Equations (2.24) and (2.25)

$$\frac{x}{2}Y_2O_3 + \frac{1}{2}Mn_2O_3 \rightleftharpoons Y_{1-x}\left[Mn_{(1-3x)}^{3+}Mn_{3x}^{4+}\right]O_3 \tag{2.24}$$

$$\frac{x}{2}Y_2O_3 + \frac{1}{2}Mn_2O_3 \rightleftharpoons Y_{(1-x)}MnO_{(3-\frac{3x}{2})} \tag{2.25}$$

It has been suggested that the introduction of oxygen deficiency increases the sinterability of $YMnO_3$ [28]. The same work also suggested that titanium substitution on the manganese site inhibits sintering of the material.

2.5 Ti^{4+} substitution

The tetravalent cation Ti^{4+} may be used as a doping element in $YMnO_3$ to induce n-type conductivity. With a Shannon radii of r=0.51 Å[13] for 5-coordinated Ti^{4+}, it will enter the manganese site as in the Kröger-Vink Equation (2.20).

Oxygen will follow the equilibrium in Equation (2.9). Hence, the equilibrium between oxygen and manganese in $YMn_{1-x}Ti_xO_{3\pm\delta}$ may be written as in Equation (2.26)

$$2\,Mn_{Mn}^{'} + \frac{1}{2}O_2(g) \rightleftharpoons 2\,Mn_{Mn}^x + O_i^{''} \tag{2.26}$$

As seen in Equation (2.3), an increased amount of manganese species being reduced to Mn^{2+} will improve the n-type conductivity. The extra electron in Mn^{2+} will enter the localized, high energy d_{z^2} orbital, as depicted in Figure 2.6.

(b) 1.12 Å and 1.019 Å, respectively[13]

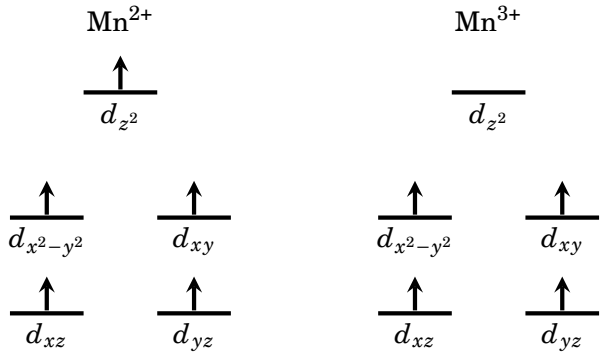

Figure 2.6: Trigonal bipyramidal crystal field splitting of Mn^{2+} and Mn^{3+}

At higher temperatures, the equilibrium in Equation (2.26) will be shifted to the left, thus increasing the n-type conductivity. As mentioned earlier, the conductivity has been measured up to $2 \times 10^{-3}\,\mathrm{S cm^{-1}}$ At 400 °C for 0 = 0.15 in bulk $YMn_{1-x}Ti_xO_{3\pm\delta}$ [25].

Other work[25, 3] has proposed that Ti^{4+} stabilizes excess oxygen, and that charge compensation from Ti^{4+} substitution occurs through the incorporation of interstitial oxygen rather than reduction of manganese.

Even though the multiferrioc properties of $YMnO_3$ is of great interest, bulk polycrystalline samples suffers from microcracking and porosity, which strongly affects the ferroelectric response[29]. In the range 600−1000 °C a volume change of 3.7 % combined with an anisotropic thermal expansion in the $a-$ and $c-$directions results in microcracks. For doping levels $x < 0.175$, the c/a-ratio has been shown to decrease and consequently decrease microcrack density from 3.2 % for undoped $YMnO_3$ to 0.9 % for $YMn_{1-x}Ti_xO_{3\pm\delta}$ with $x = 0.1$[29]. At doping levels x>0.175 in $YMn_{1-x}Ti_xO_{3\pm\delta}$, there is a phase transition from the ferroelectric hexagonal phase to a paraelectric rhombohedral phase[29]. When analysing a sample with X-ray diffraction, it can be seen that the peak around 2θ =23° will disappear completely at x=0.15[30], as seen in Figure 2.7

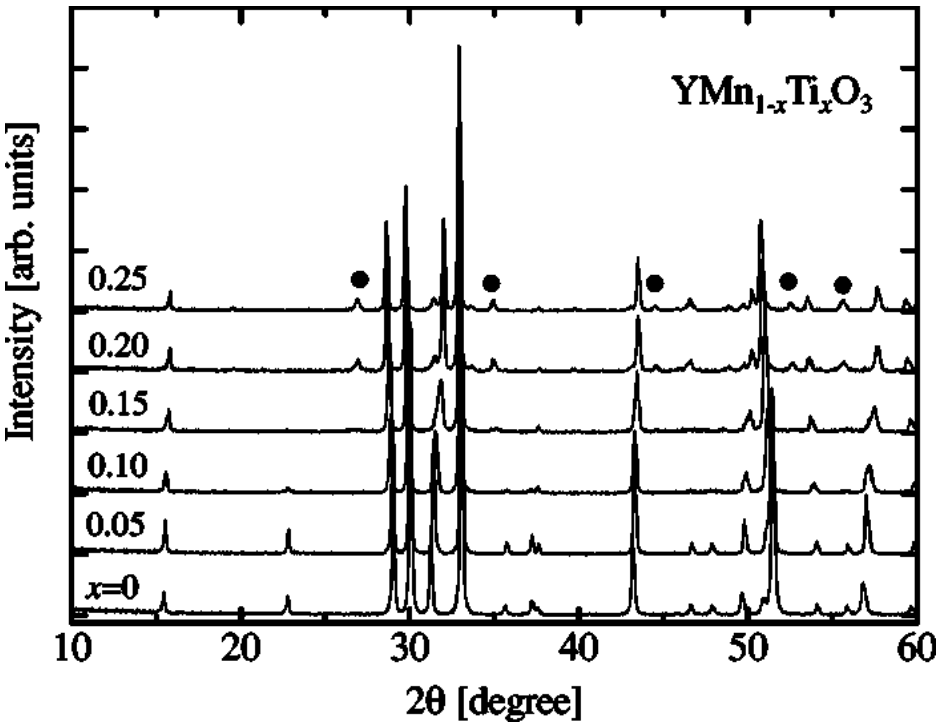

Figure 2.7: X-ray diffraction pattern of $YMn_{1-x}Ti_xO_{3\pm\delta}$ with x from 0 to 0.25. The peak at 23° disappear at x=15, and a new peak is visible around 27°. Figure taken from [30].

2.6 Charge storage in pseudocapacitor electrodes

There are three general mechanisms for charge storage in pseudocapacitors[2]. At metal- and metal oxide surfaces, ions may adsorb as a monolayer on the electrode surface. A second possibility is redox reactions at the electrode surface, such as protonation of an oxide as shown in Equation (2.27)[9].

$$MO_2 + xH^+ + xe^- \rightleftharpoons MO_{2-x}OH_x \tag{2.27}$$

Thirdly, ions may be intercalated into the bulk of the electrode material. This process is fast and reversible, and charge may be stored as either cations [31] or anions[2].

2.6.1 Oxygen Intercalation

Insertion of cations like Li^+ and Na^+ into a host lattice is easy, due to their small size[7]. Insertion of large anions like oxygen, is not. The oxidation of metal cations in the host lattice causes the lattice to shrink, thus making the insertion of large anions even harder[7]. Even though electrochemical oxidation of non-stoichiometric perovskites and related structures has been researched since before 1975[10], intercalation of oxygen into the lattice was first observed in 1990[7] by [11]. The method has typically been used to synthesize highly oxidized materials.

A recent paper[2] investigated the role of oxygen vacancies in charge storage in $LaMnO_{3\pm\delta}$. By using cyclic voltammetry, it was found that oxygen was intercalated into the bulk of the structure by oxidation of manganese centers. A hydroxide specie adsorbed at a surface vacancy would transfer it's proton to a neighbouring hydroxide specie, and then diffuse into a vacant site. As in Equation (2.6), an oxygen vacancy in an undoped hexagonal manganite is accompanied by two reduced manganese centers. The initial filling of vacancies was accompanied by oxidation of Mn^{2+} to Mn^{3+} and was visible as a peak in the voltammogram.

Further intercalation of excess oxygen was followed by oxidation of Mn^{3+} to Mn^{4+} and was visible as a separate peak at lower potentials. The excess oxygen was also accompanied by diffusion of manganese to the surface. The first step was mainly observed for an oxygen deficit sample. The second step, can be described by Equation (2.28).

$$OH^-_{ads} + OH^-_{aq} + 2Mn^x_{Mn} + V^{\bullet\bullet}_O \overset{LaMnO_3}{\rightleftharpoons} O^x_O + H_2O + 2Mn^{\bullet}_{Mn} + 2e^- \tag{2.28}$$

Figure 2.8 is a cyclic voltammogram of $LaMnO_3$ taken from [2]. The reversible intercalation of oxygen is visible as a peak at $\sim E_{1/2} = -0.25\,V$ vs Ag/AgCl in (**a**). The pseudocapacitance can be seen as nearly rectangular curves with a redox peak. The rectangular shape of the curve is due to the electrical double layer capacitance, whereas the peaks are due to reversible intercalation of oxygen.

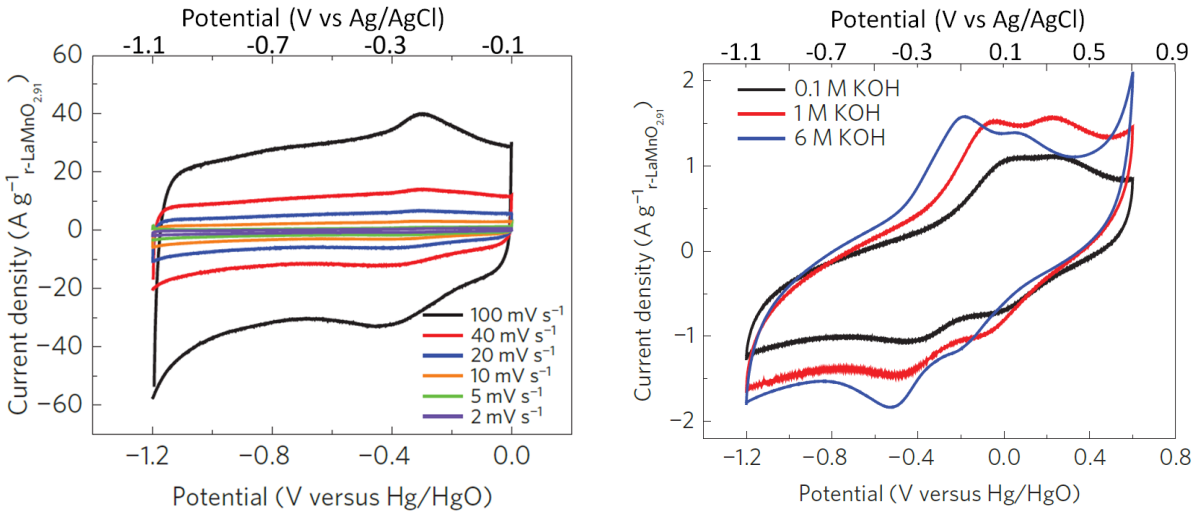

Figure 2.8: Cyclic voltammograms of oxygen-deficit $LaMnO_{2.91}$ in 1 M (**a**) Ar(g) purged KOH. The oxidation if Mn^{2+} to Mn^{3+} and further to Mn^{4+} is visible as two peaks in (**b**), which is unsupported particles. In (**a**), the current and capacitance contribution from the mesoporous carbon has been subtracted out. An axis for potential vs Ag/AgCl has been added. Figure taken from [2].

2.6.2 Intercalation of oxygen in $YMnO_3$

The crystal structure of hexagonal $YMnO_3$ is much less densely packed than the perovskite counterparts. In perovskites, the main oxygen point defect are vacancies which are entropy stabilized. In hexagonal manganites, the spacious structure allows for incorporation of highly mobile interstitial oxygen. Recent density functional theory calculations [32] show that interstitial oxygen are enthalpy stabilized. Hence, as according to $\Delta G = \Delta H - T\Delta S$, O''_i should be stabilized at low temperatures, whereas vacancies are stabilized at higher temperatures. Consequently, in addition to intercalation into vacancies as in Equation (2.28), oxygen may also be intercalated into $YMnO_3$ interstitially, through a similar mechanism as shown in Equation (2.29)

$$OH^-_{ads} + OH^-_{aq} + 2Mn^x_{Mn} \overset{YMnO_3}{\rightleftharpoons} O''_i + H_2O + 2Mn^{\bullet}_{Mn} + 2e^- \tag{2.29}$$

Although oxygen most likely intercalates as oxygen species, the possibility of hydroxide ions, as in Equation (2.30) should also be considered.

$$OH^-_{ads} + Mn^x_{Mn} \overset{YMnO_3}{\rightleftharpoons} OH_i^{'} + Mn^{\bullet}_{Mn} + e^- \tag{2.30}$$

The possibility of formation of oxygen excess $YMnO_{3+\delta}$ is indeed promising, and it has been reported values of δ up to $\delta > 0.25$ in oxidizing conditions[12], as in Equation (2.9).

The theoretical capacity for oxygen intercalation into interstitial sites has reported to be $\delta = 0.33$ in $YMnO_{3+\delta}$[32]. Each layer of Mn-O has the capacity to hold one interstitial oxygen, which oxidizes two out of three manganese. Further interstitial oxygen content would require oxidation of manganese across layers, or oxidation of Mn^{4+} to Mn^{5+}[32].

Oxygen diffusion in perovskite related oxides

Oxygen diffusion coefficients have been measured electrochemically in a number of perovskite related oxides[33], and are usually in the range 10^{-14} to $10^{-11} cm^2 s^{-1}$. A recent study[34] developed a model for estimation of the diffusion coefficient of oxygen in the perovskite $Ca_{0.5}La_{0.5}FeO_{2.618}$, which was used by [2, 35] to estimate the diffusion coefficient in $LaMnO_3$. The model requires galvanostatic measurements (constant current), and was based on diffusion in- and towards a plane sheet due to plate-like particles with a thickness of approximately 250 nm[36]. Despite the lack of galvanostatic measurements in the characterization of $LaMnO_3$[2], the model was used on oval-like particles. No model has been found for diffusion towards- and in spherical particles deposited on a substrate.

2.7 Cyclic voltammetry

In cyclic voltammetry, the current passing through a system is measured while an applied potential is cycled between two set values[37], as illustrated in Figure 2.9a. Figure 2.9b illustrates a cyclic voltammogram for platina, measured in N_2(g) purged 1M KOH at a sweep rate of $100\,mV\,s^{-1}$.

An electrochemical reaction is a redox reaction involving the transfer of electrons from one species to another, as would be the case for intercalation of oxygen in Equations (2.28) to (2.30). In a cyclic voltammogram, this can be detected by a change in the total current passing through the system, visible as peaks in the current versus potential plot.

A general feature observed in the anodic direction of a cyclic voltammogram of non-stoichiometric perovskites, is a plateau corresponding to the oxidation of metal cations, as shown in Figure 2.10.

$YMnO_3$ is an insulator. By using mesoporous carbon (MC) as a support material and a current collector, a larger total surface area of $YMnO_3$ may be achieved. This is illustrated in Figure 2.11.

The choice of mesoporous carbon is not necessarily a straight forward one. Many types of mesoporous carbon are available, and carbon black may also be a viable alternative. Nitrogen-doped ordered mesoporous carbon was used in [2], but the synthesis of such[38] involves either flowing NH_3 at high temperatures (e.g. 1000 °C) or HCN. Both, of which involves high risk elements that should be avoided if possible. Other available types includes Starbon™ which can be bought with the desired surface area and pore diameter [39].

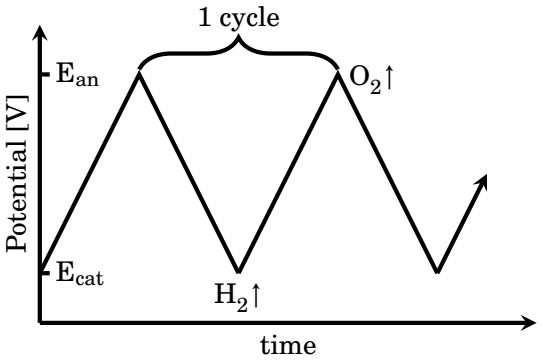

(a) The working principle of cyclic voltammetry. The current passing through a system is measured when an applied potential is cycled between to set values. Figure inspired by [37, page 261]

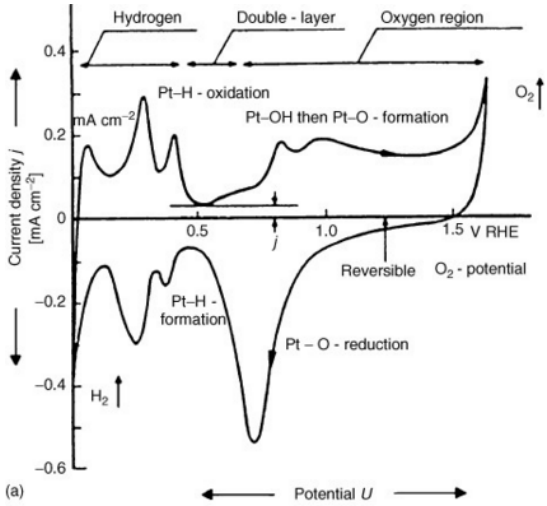

(b) Cyclic voltammogram of polycrystalline platina in N_2(g)-purged 1M KOH at $100\,\mathrm{mV\,s^{-1}}$. Figure taken from[37, page 262]

Figure 2.9: A schematic illustration of the working principle of cyclic voltammetry (2.9a) and a corresponding cyclic voltammogram for polycrystalline platina (2.9b).

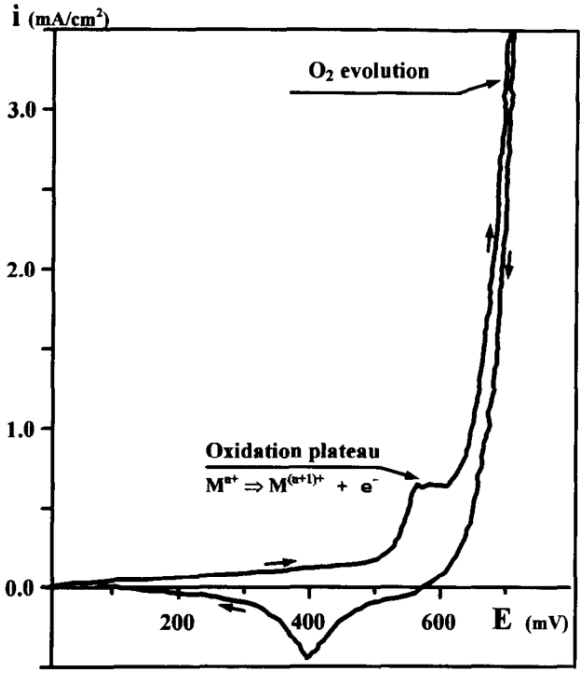

(a) A typical voltammogram showing the oxidation plateau in the anodic direction of a cyclic voltammogram. Taken from[7]

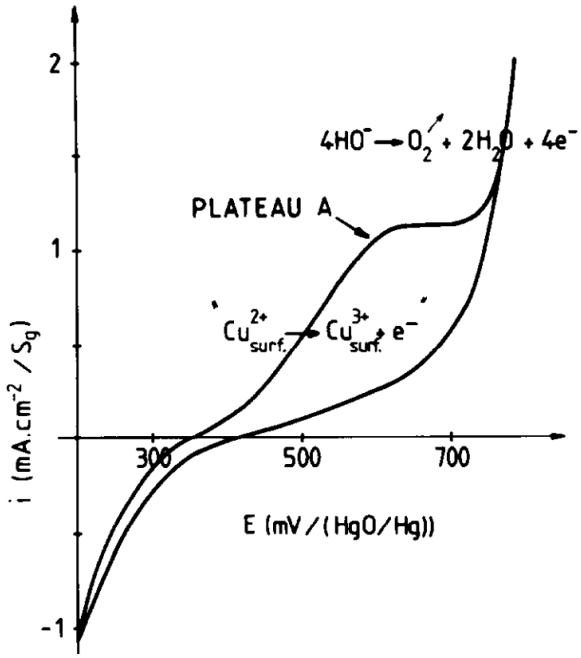

(b) Cyclic voltammogram of La_2CuO_4 in 1 M KOH, taken from[11]

.

Figure 2.10: Examples of the oxidation plateau for non-stoichiometric perovskites that occur right before oxygen evolution in the anodic direction of a cyclic voltammogram.

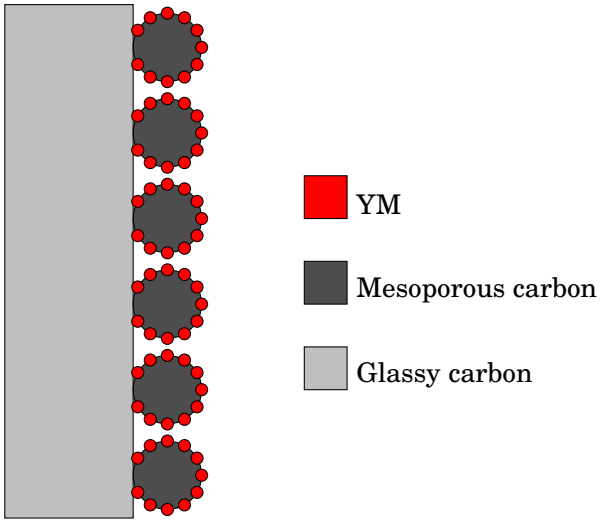

Figure 2.11: Principle schematic of a thin film electrode surface. The mesoporous carbon functions as both support and current collector. The electrode is made from inert, glassy carbon

2.7.1 Separation of faradic and non-faradic currents

The current measured during cyclic voltammetry is the sum of all the currents passing through the system. The current contribution from each specie present, I_i, may be attributed to a faradic current $I_{\mathrm{i,f}}$ and a non-faradic current $I_{\mathrm{i,nf}}$, as in Equation (2.31). In general, faradic currents obey Faraday's law and are proportional to the amount of oxidized and reduced species in a redox reaction[40]. Non-faradic currents are generally not due to electrochemical reactions, but rather charging of the electrochemical double layer and other effects[40, p. 272]. For the three component system of $YMnO_3$ loaded onto mesoporous carbon, deposited o to glassy carbon, the term $I_{i,nf}$ generally refers to the capacitive charging of the double layer on each component. Consequently, the term $I_{i,f}$ refers to any oxidation or reduction reaction that might occur.

$$I = \sum I_{\mathrm{i}} = \sum \left(I_{\mathrm{i,f}} + I_{\mathrm{i,nf}} \right) \tag{2.31}$$

In this work, where $YMnO_3$ (YM) is supported on mesoporous carbon, the current contribution from the carbon may be subtracted by performing a blank experiment, i.e. preparing and characterizing an electrode of mesoporous carbon with no $YMnO_3$ present. The signal from mesoporous carbon (MC) may then be subtracted point-by-point, so that $I_{YM} = I_{\mathrm{tot}} - I_{\mathrm{MC}}$. The resulting current will be the sum of faradic and non-faradic currents[40] from $YMnO_3$.

From the sum if the faradic and non-faradic currents, Equation (2.32) may be expressed[41] where v is the sweep rate in $\mathrm{V\,s^{-1}}$, $\alpha\sqrt{v}$ is the faradic contribution and βv is the non-faradic current.

$$I = I_{\mathrm{nf}} + I_{\mathrm{f}} = \beta v + \alpha\sqrt{v} \tag{2.32}$$

Rewriting Equation (2.32) as Equation (2.33) allows the faradic and non-faradic currents to be separated along the curve by finding the values of α and β for each point on the curve, as long as more than two sweep rates has been employed[40].

$$\frac{I}{\sqrt{v}} = \beta\sqrt{v} + \alpha \tag{2.33}$$

Chapter 3

Experimental procedure

3.1 List of chemicals used

The chemicals used in the solid state synthesis of $YMn_{1-x}Ti_xO_{3\pm\delta}$ and electrochemical characterization are listed in Table 3.1. The properties of the two different types of mesoporous carbon (MC) used as support for nanoparticles are listed in Table 3.2

Table 3.1: List of chemicals used in the solid state synthesis of $YMn_{1-x}Ti_xO_{3\pm\delta}$ and during electrochemical characterization

Chemical	Manufacturer	Note
Bulk Y_2O_3	Sigma Aldrich	>99.99 % trace metal basis
Bulk Mn_2O_3	Sigma Aldrich	>99.99 % trace metal basis
Bulk TiO_2	Sigma Aldrich	>99.99 % trace metal basis
Nafion™-117 Solution	Sigma Aldrich	5% in a mixture of lower aliphatic alcohols and water
KOH	Merck	>85% trace metal basis

Table 3.2: Two different products of mesoporous carbon were used. Also known as graphitized carbon black, Starbon™800 and Starbon™300. The Starbon™No. denotes the temperature in degree celsius of which the mesoporous carbon was prepared. SEM pictures of the two types taken from Sigma Aldrich[42, 43] are given in Figure 3.1. It appear that the particle sizes are approximately equal. According to [39], a higher preparation temperature results in a smaller pores and a higher total pore volume and surface area.

Product number	Starbon™No.	Particle size	Pore size	Surface area
702102	800	>1 µm	$\frac{0.4-0.7 cm^3 g^{-1} mesoporosity}{0-0.25 cm^3 g^{-1} microporosity}$	>500 $m^2 g^{-1}$ (BET)
702110	300	5-50µm (SEM)	>0.2$cm^3 g^{-1}$	>50 $m^2 g^{-1}$ (BET)

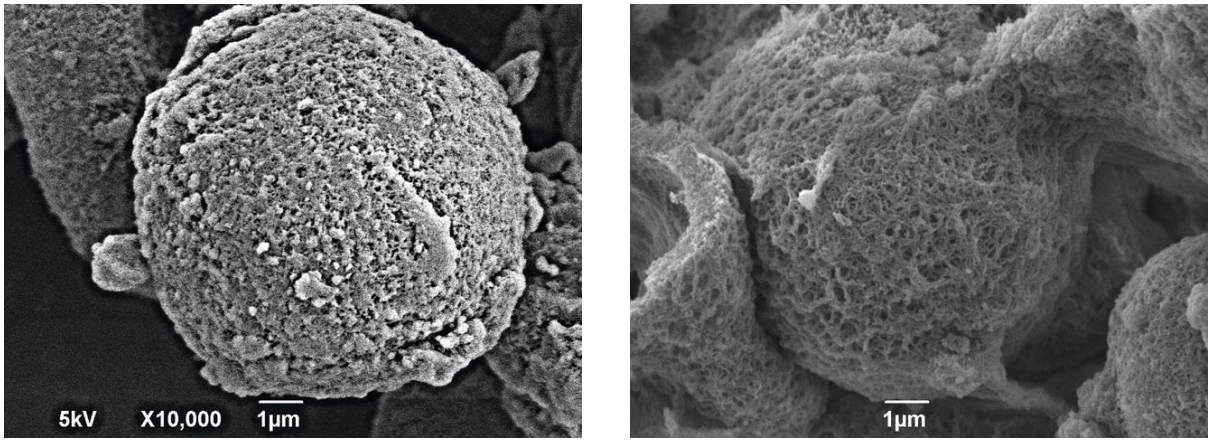

(a) Starbon™800 **(b)** Starbon™300

Figure 3.1: SEM pictures of the two different types of mesoporous carbon, taken by Sigma Aldrich [42, 43].

3.2 Solid State synthesis of $YTi_{0.12}Mn_{0.88}O_{3\pm\delta}$

Bulk powders of Mn_2O_3, Y_2O_3 and TiO_2 were dried in air at 650 °C over night. The powders were mixed in stoichiometric amounts [(a)] and wet-mortared in ethanol. After drying in air, the mortared powder was pressed into 20 mm pellets and discs[(b)] by cold uniaxial double action pressing, with a load of approximately 960 kg (P≈30 MPa). The pressed samples were placed on sacrificial powder on an alumina disc, and sintered in air at 1450 °C for 12 hours, with a heating- and cooling rate of ±200 °C h^{-1}, as shown in Figure 3.2, point **a**. The pressed pellets were crushed and mortared. The mortared powder was sieved in sieves with an opening of 250 µm, 200 µm, 150 µm and 37 µm successively. The sintered discs were polished on grade 800 and 2400 SiC-paper and put aside for use in Section 3.9. Some of the sieved powder was pressed into 20 mm discs by cold uniaxial double action pressing with a load of approximately 1921 kg (P≈60 MPa), placed on sacrificial powder on an alumina disc, and sintered in air at 1400 °C for 10 hours, with a heating- and cooling rate of ±200 °C h^{-1}, as shown in Figure 3.2 point **b**. The sintering time and temperature was reduced on the second sintering in order to avoid excessive grain growth[29].

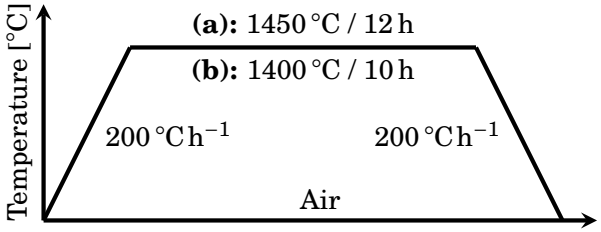

Figure 3.2: The selected heat treatment program for solid state synthesis of $YTi_{0.12}Mn_{0.88}O_{3\pm\delta}$ from binary oxides, denoted **a**. The pressed pellets and discs of binary oxides were sintered in air at 1450 °C for 12 hours, with a heating- and cooling rate at 200 °C h^{-1}. Pressed discs of bulk $YTi_{0.12}Mn_{0.88}O_{3\pm\delta}$ were sintered at 1400 °C for 10 hours (**b**), with a heating- and cooling rate at 200 °C h^{-1}. Time and temperature were reduced for the second sintering to avoid excessive grain growth.

[(a)] 8.4555 g, 13.7508 g and 1.1820 g

[(b)] A disc is a thin pellet 1 – 2mm thick.

3.3 Synthesis of nanocrystalline $YMn_{1-x}Ti_xO_{3\pm\delta}$

Nanocrystalline $YMnO_3$ was synthesized by [1] from an aqueous chemical synthesis route. $Mn(CO_3)_2 \cdot xH_2O$ was added to an aqueous solution of citric acid. $Y(O_2C_2H_3)_3 \cdot xH_2O$ was dissolved in citric acid, and both solutions were mixed in stoichiometric amounts. The solution was held at 150 °C until a gel formed and calcined at 825 °C for 1 h.

Nanocrystalline $YTi_{0.15}Mn_{0.85}O_{3\pm\delta}$ was synthesized by [44] with a modified citric acid method. Ion containing precursors were added in stoichiometric amounts to a beaker containing ethylene glycol. After gelling, drying and calcining, the powder was heat treated at 800 °C for 1 h, resulting in nanoparticles of $YTi_{0.15}Mn_{0.85}O_{3\pm\delta}$.

3.4 X-ray diffraction and Rietveld refinement

Both the bulk and the nanocrystalline powders were analysed by X-ray diffraction with a BRUKER D8 Advance Da-Vinci with a LynxEye Xe detector, using CuK_α radiation. The samples were scanned with an angle 2θ from 10 to 75° with a constant 0.2 mm divergence slit for 120 min. The bulk $YTi_{0.12}Mn_{0.88}O_{3\pm\delta}$ was placed in a standard powder sample holder. The nanoparticles of $YMnO_3$ and $YTi_{0.15}Mn_{0.85}O_{3\pm\delta}$ were deposited on a Si single crystal by adding a small amount to the crystal surface, and using a drop of ethanol do distribute the nanoparticles randomly across the surface. The peaks were matched to the $P6_3cm$ space group for $YMnO_3$ using BRUKER DIFFRAC.EVA 4.0. The XRD-patterns were refined by Rietveld refinement using BRUKER DIFFRAC.SUITE TOPAS 5[45] for unit cell parameters, lattice positions, and crystallite size (nanoparticles). The instrument parameters used are listed in Table 3.3. Starting-parameters used in the refinement were taken from [46, Table IV], and are given in Table 3.4.

Table 3.3: Instrument parameters used in the Rietveld-refinement of the X-ray diffraction patterns

Parameter	Value
Primary radius (mm)	280
Secondary radius (mm)	280
Linear PSD 2Th angular range (°)	3
FDS angle (°)	0.1
Full Axial Convolution	Yes
Filament length (mm)	12
Sample length (mm)	15
Receiving Slit length (mm)	12
Primary Sollers (°)	2.5
Secondary Sollers (°)	2.5

Table 3.4: Starting-parameters used in the Rietveld-refinement of $YMn_{1-x}Ti_xO_{3\pm\delta}$. Space group was no. 185. Unit cell parameters were a=6.14151 Å and c=11.4013 Å. The values are for undoped $YMnO_3$ at T=293 K, taken from [46, Table IV]. Ti^{4+} was added to the Mn-site for the doped particles, and the occupancy-values were adjusted accordingly. x=0.12 for bulk and x=0.15 for nanoparticles.

Site	Np	x	y	z	Atom	Occ	Beq
Y1	2	0.00000	0.00000	0.27280	Y+3	1	1
Y2	4	0.33333	0.66667	0.23250	Y+3	1	1
Mn	6	0.31770	0.00000	0.00000	Mn+3	1-x	1
					Ti+4	x	1
O1	6	0.30740	0.00000	0.16260	O-2	1	1
O2	6	0.64270	0.00000	0.33550	O-2	1	1
O3	2	0.00000	0.00000	0.47440	O-2	1	1
O4	4	0.33333	0.66667	0.01690	O-2	1	1

3.5 Stability test

In order to quickly find out if the hexagonal phase of $YMn_{1-x}Ti_xO_{3\pm\delta}$ is stable at high pH, two parallel experiments were performed as illustrated in Figure 3.3. Bulk powder[(c)] of $YTi_{0.12}Mn_{0.88}O_{3\pm\delta}$ was suspended in 40 mL 3 M KOH in a centrifuge tube for 4 days. The suspension was then centrifuged at 11000rpm for 7 minutes and decanted. Deionized water (DI water) was added, before the tube was shaken vigorously and once more centrifuged This was done 10 times. The centrifuge tube with the washed particles was then placed in a heating cabinet at 50 °C for 24 h. The dried powder was analysed by X-ray diffraction and Rietveld refined, as in Section 3.4. The centrifuge tube with bulk powder was weighted before addition of KOH and after drying.

In the second parallel, nanoparticles of $YTi_{0.15}Mn_{0.85}O_{3\pm\delta}$ were adhered on a piece of carbon tape and analysed by X-ray diffraction as in Section 3.4. The piece of carbon tape with nanoparticles was suspended in 3 M KOH for 4 days. The sample was then washed carefully in DI water.

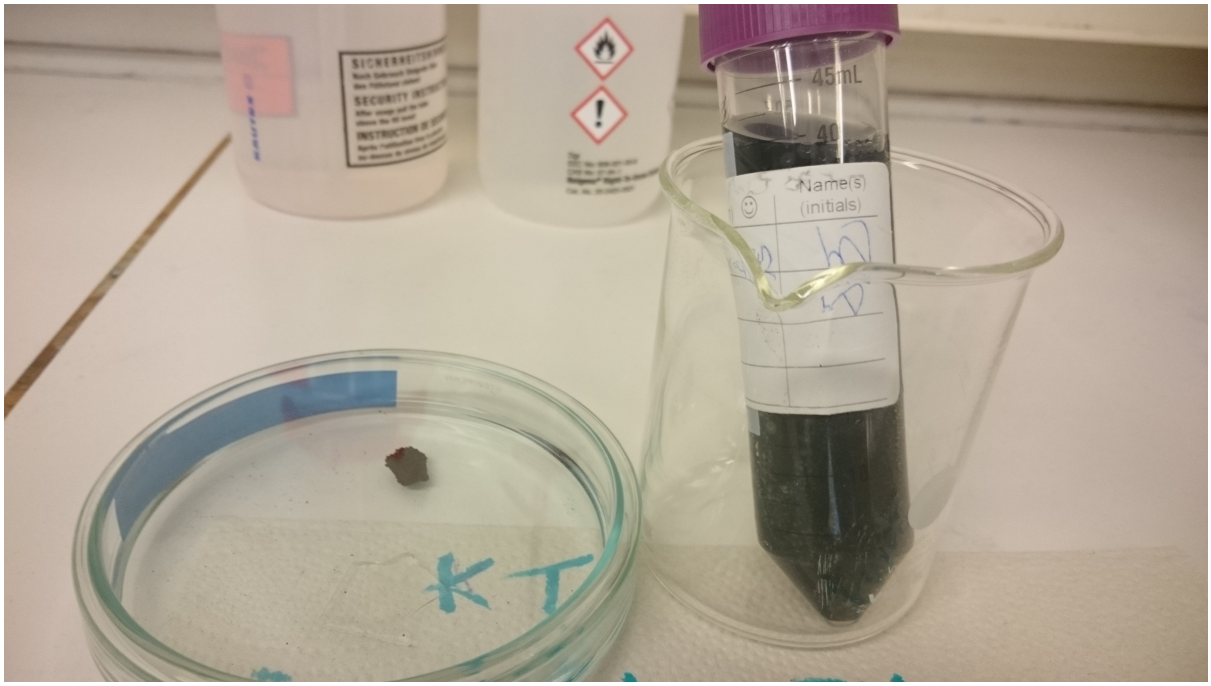

Figure 3.3: Nanoparticles of $YTi_{0.15}Mn_{0.85}O_{3\pm\delta}$ adhered onto carbon tape (left) and bulk $YTi_{0.12}Mn_{0.88}O_{3\pm\delta}$ in suspension (right), both in 3 M KOH. This was left for 4 days.

[(c)] 1.8653 g

3.6 Electrochemical characterization by cyclic voltammetry

Due to the low reproducibility of results, and suspected low adhesion between the deposited particles and glassy carbon surface in earlier work[6], a number of electrode preparation methods were explored in order to evaluate the strengths and weaknesses of each method. The electrochemical response of each electrode was measured using cyclic voltammetry on an aqueous solution of KOH. Those that did not produce presentable results, i.e. methods that did not result in an electrode that could be characterized, are explained in detail in Appendix B. The main difference between the different setups was the design of the working electrode. Out of the three different configurations used, one was using the sintered discs of bulk $YTi_{0.12}Mn_{0.88}O_{3\pm\delta}$ from Section 3.2 as the working electrodes. The principle of the other two methods was to modify a glassy carbon surface by depositing thin films of $YMn_{1-x}Ti_xO_{3\pm\delta}$. The following Sections 3.7 to 3.9 will present the three aforementioned methods in detail.

3.6.1 Equipment

Electrochemical characterization was performed using a three-electrode cell with a working (WE), reference (RE) and counter (CE) electrode. The potential was controlled using a Gamry Instruments Reference 600 potentiostat, which was controlled using the Gamry Framework software [47]. A Radiometer Analytical REF201 (Ag/AgCl) was used as the reference electrode. A simple Pt(s) electrode was used as the counter electrode (CE). In Section 3.7, a glassy carbon rotating disc electrode[(d)] (GCRDE) was used as the working electrode. In Section 3.8, a glassy carbon rod with a diameter of 5 mm was used as the working electrode. Finally, in Section 3.9, a sintered disc of bulk $YTi_{0.12}Mn_{0.88}O_{3\pm\delta}$ (as synthesized in Section 3.2) was used as the working electrode. The difference between the RDE and rod electrodes can be seen in Figure 3.4

For verifying the functionality of the electrochemical setup, it was recorded voltammograms for a platina RDE in 1 M KOH between −1 V and 0.5 V at various sweep rates.

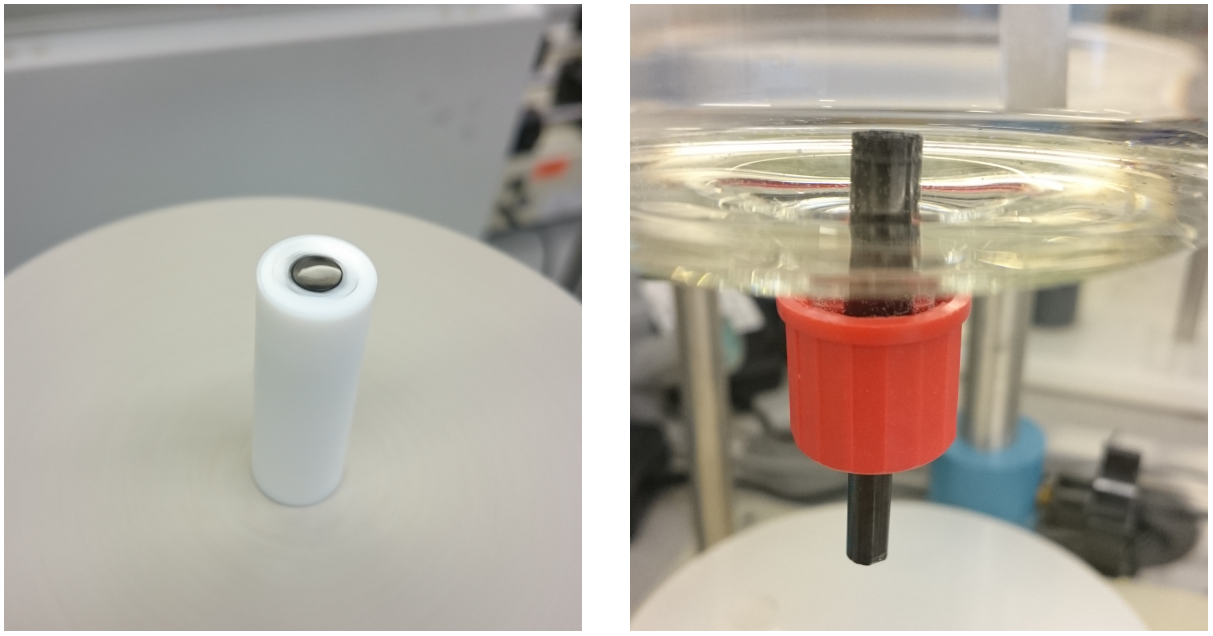

(a) **(b)**

Figure 3.4: Pictures of the glassy carbon RDE (**a**) and rod (**b**) electrodes.

[(d)] Pine Instruments Glassy Carbon HotSpot RDE tip (5 mm disk OD)

3.7 Glassy carbon rotating disc electrode

The 3-electrode cell was assembled as shown in in Figure 3.5. The aforementioned reference and counter electrodes were used, with the glassy carbon RDE as the working electrode. N_2(g) purged 3 M KOH was used as the electrolyte. A few of the electrodes were also scanned in O_2(g) saturated 3 M KOH in order to see if the oxygen reduction reaction could be detected.

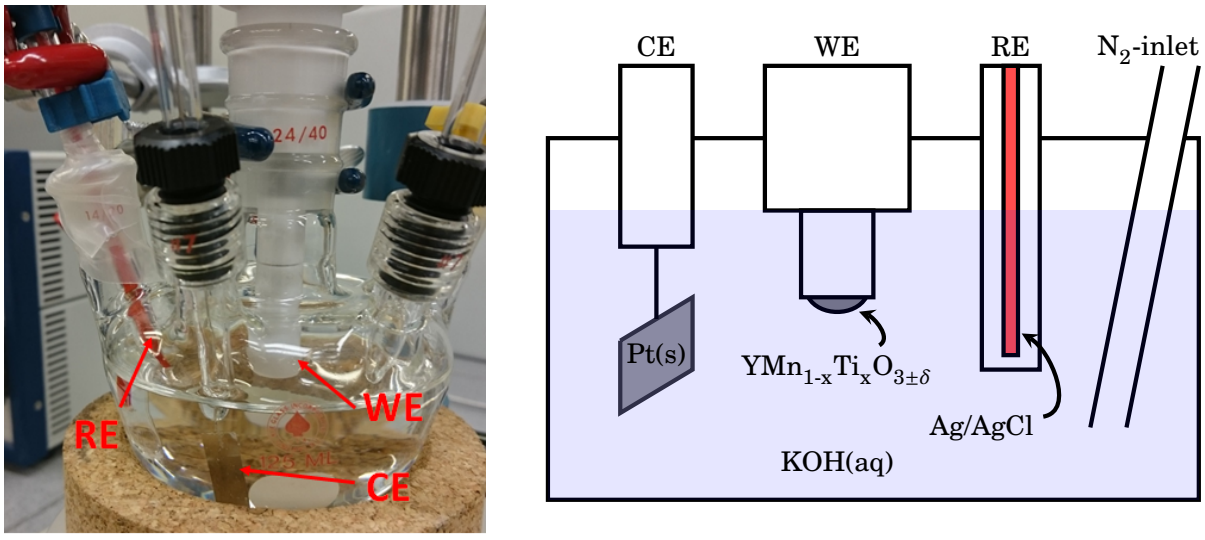

(a) **(b)**

Figure 3.5: A picture (**a**) and a principle sketch (**b**) of the 3-electrode cell used for the glassy carbon rotating disc electrode.

Particles were deposited onto the glassy carbon RDE by spin coating from an ethanol suspension. All the suspensions were sonicated for 30 minutes, before 10 µL were spin coated onto the GCRDE at 200rpm. The glassy carbon electrode was polished to a glassy finish using a 0.05 µm alumina suspension on a polishing cloth and then sonicated, prior to deposition. Different suspensions was used, as will be elaborated further in the following sections. All the electrodes were scanned at various sweep rates.

3.7.1 Unsupported particles

In order to explore the electrochemical response and adhesive properties between $YMn_{1-x}Ti_xO_{3\pm\delta}$ and glassy carbon, two suspensions of either bulk $YTi_{0.12}Mn_{0.88}O_{3\pm\delta}$ or nanocrystalline $YTi_{0.15}Mn_{0.85}O_{3\pm\delta}$ suspended at 20 mg mL^{-1} were used. Electrodes were prepared with mass loadings of 1 mg cm^{-2}. The electrodes were scanned in O_2(g) saturated 3 M KOH. Each electrode was prepared and characterized twice in order to reveal any problems with reproducibility. The bulk electrodes were cycled between −1.8 V and 0.5 V. The cathodic turnaround potential was kept at −0.8 V for the nanocrystalline particles in order to avoid evolution of gaseous hydrogen. The second nanocrystalline electrode was first cycled between −0.4 V and 0.2 V in order to make sure gaseous evolution would not occur, before the first scans between −0.8 V and 0.5 V were repeated. After characterization, the electrodes were gently rinsed with DI-water. The experimental procedure for unsupported particles are summarized in Table 3.5

Table 3.5: Summary of the unsupported films used on the GCRDE. Each film was made by spin coating 10 µL of a 20 mg mL^{-1} suspension at 200rpm.

Electrode no.	Material	Mass loading	Potential window
1	Bulk $YTi_{0.12}Mn_{0.88}O_{3\pm\delta}$	1 mg cm^{-2}	−1.8 V to 0.5 V
2	Bulk $YTi_{0.12}Mn_{0.88}O_{3\pm\delta}$	1 mg cm^{-2}	−1.8 V to 0.5 V
3	Nano $YTi_{0.15}Mn_{0.85}O_{3\pm\delta}$	1 mg cm^{-2}	−0.8 V to 0.5 V
4	Nano $YTi_{0.15}Mn_{0.85}O_{3\pm\delta}$	1 mg cm^{-2}	−0.4 V to 0.2 V
4	Nano $YTi_{0.15}Mn_{0.85}O_{3\pm\delta}$	1 mg cm^{-2}	−0.8 V to 0.5 V

3.7.2 Nanocrystalline $YMnO_3$ supported on mesoporous carbon

As in earlier work[6], nanoparticles of $YMnO_3$ were loaded in to mesoporous carbon type Starbon™800 (ST8) at 30wt% $YMnO_3$ by mortaring, and suspended at 1 mg mL^{-1} in ethanol. An electrode was prepared with a total mass loading of 51 µg cm^{-2}. The electrode was cycled in various potential windows. An electrode was also prepared with only mesoporous carbon at the same mass loading in order to determine the current contribution from the support material.

Two more suspensions were prepared, using mesoporous carbon type Starbon™300 (ST3). The same 30wt% $YMnO_3$ at mesoporous carbon ratio was used, with suspension loadings at 1 mg mL^{-1} and 2 mg mL^{-1} in ethanol. After preparing electrodes with total mass loadings of 51 µg cm^{-2} and 102 µg cm^{-2}, respectively, they were characterized the same way as aforementioned.

The experimental procedure for unsupported particles are summarized in Table 3.6

Table 3.6: Summary of the supported films used on the GCRDE, containing nanoparticles loaded onto mesoporous carbon at 30wt%. Each electrode was made by spin coating 10 µL of a 1 mg mL^{-1} suspension onto the GCRDE at 200rpm. Electrode number 5 was made from a 2 mg mL^{-1} suspension.

Electrode no.	Material	Total mass loading	Potential window
1	$YMnO_3$ @ ST8	51 µg cm^{-2}	−1.5 V to 0.5 V
1	$YMnO_3$ @ ST8	51 µg cm^{-2}	−1.6 V to 0.5 V
1	$YMnO_3$ @ ST8	51 µg cm^{-2}	−1.7 V to 0.5 V
1	$YMnO_3$ @ ST8	51 µg cm^{-2}	−1.9 V to 0.5 V
2	MC ST8	51 µg cm^{-2}	−1.7 V to 0.5 V
3	MC ST8	51 µg cm^{-2}	−1.7 V to 0.5 V
4	$YMnO_3$ @ ST3	51 µg cm^{-2}	−1.5 V to 0.5 V
5	$YMnO_3$ @ ST3	102 µg cm^{-2}	−1.5 V to 0.5 V

3.7.3 Nafion™ as binder

Three suspensions of 20 mg mL^{-1} bulk $YTi_{0.12}Mn_{0.88}O_{3\pm\delta}$ in ethanol were prepared as in Section 3.7.1. A solution of 5wt% Nafion™ was added so that the Nafion™ loadings were approximately 1wt%, 0.05wt% and 0.025wt% Nafion™ in ethanol[(e)]. A fourth suspension was prepared by suspending bulk $YTi_{0.12}Mn_{0.88}O_{3\pm\delta}$ in ethanol containing 0.1wt% Nafion™ at 50 mg mL^{-1}. After sonication, electrodes were prepared with a total mass loading of 1 mg cm^{-2},

[(e)] 100, 5 and 2.5 µL added to 2 mL ethanol. 10 µL for 0.1wt%

or 2.5 $\mathrm{mg\,cm^{-2}}$ for no. 4. The electrodes were cycled in both in O_2(g)-saturated electrolyte (not 1wt%) and after purging with N_2(g) for 20 minutes, with a subsequent gas lid.

A fifth suspension was prepared by loading nanoparticles of undoped $YMnO_3$ onto ordered mesoporous carbon ST3 at 30wt% $YMnO_3$ by mortaring. This was suspended in ethanol containing 0.025wt% Nafion™ at 1 $\mathrm{mg\,mL^{-1}}$. An electrode with a total mass loading of 51 $\mathrm{\mu g\,cm^{-2}}$ was prepared and cycled in N_2(g)-purged 3 M KOH. The electrodes were cycled from −1.5 V to 0.5 V. The nanocrystalline electrode was cycled at two wider ranges as well.

The composition of each suspension is given in Table 3.7

Table 3.7: The suspensions used to evaluate the feasibility of using unmodified Nafion™ polymer as an adhesive agent. Suspensions 1-4 were made with bulk powder of $YTi_{0.12}Mn_{0.88}O_{3\pm\delta}$, whereas no. 5 was made by loading nanoparticles of undoped $YMnO_3$ onto mesoporous carbon ST8 at 30wt% $YMnO_3$ by mortaring. All the suspensions were sonicated for 30 minutes, and then 10 µL was spin coated onto the glassy carbon RDE at 200rpm.

No.	Suspension loading $[\mathrm{mg\,mL^{-1}}]$	Nafion™ content wt% in ethanol	$\frac{\text{Suspension loading}}{\text{wt\% Nafion}}$	Total mass loading $[\mathrm{mg\,cm^{-2}}]$
1	20	0.025	800	1
2	20	0.05	400	1
3	20	1	20	1
4	50	0.1	500	2.5
5	1	0.025	40	0.051

3.8 Glassy carbon rod

In order to improve the contact force between the deposited thin film and the glassy carbon surface, it was attempted to use an inverted setup (This way, gravity would pull the particles down towards the electrode and not away from it). A glassy carbon rod with a diameter of 5 mm was used as the working electrode. The GC rod was electrically insulated on the sides with a shrinking tube. After cleaning and sonicating the surface, the rod was inserted into the cell from beneath. The same suspensions as for the GCRDE without Nafion™ (Sections 3.7.1 and 3.7.2) were used. All the suspensions were sonicated for 30 minutes, and then 10 µL was drop coated onto the exposed surface without rotation. The cell was then carefully filled with 3 M KOH and assembled. A principal sketch and a photography is shown in Figure 3.6. Cyclic voltammetry was performed at various sweep rates, both in O_2(g)-saturated electrolyte and after purging with N_2(g) for 20 minutes, with a subsequent gas lid.

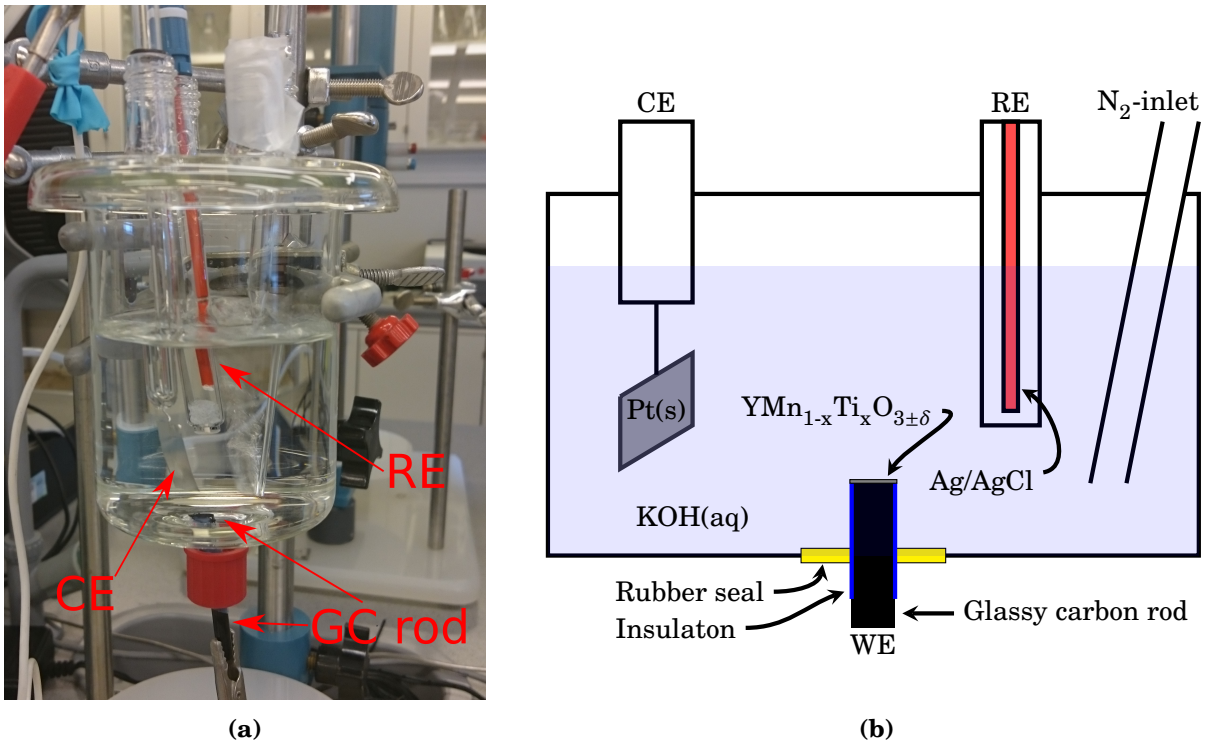

(a) **(b)**

Figure 3.6: A picture (**a**) and an illustration (**b**) of the inverted setup. The primary difference from the rotating disc electrode setup in Section 3.7 was that the electrode surface pointed upwards, so that gravity would improve the contact force between the deposited particles and the electrode surface.

3.8.1 Unsupported particles

The same suspensions as in Section 3.7.1 was used. Bulk $YTi_{0.12}Mn_{0.88}O_{3\pm\delta}$ and nanocrystalline $YTi_{0.15}Mn_{0.85}O_{3\pm\delta}$ suspended at 20 mg mL^{-1} in ethanol. The glassy carbon surface was modified with a total mass loading of 1 mg cm^{-2}. The cell was then carefully filled with 3 M KOH and assembled. It was made two depositions for both the bulk and nanocrystalline materials. The second deposition of bulk particles was cycled at three potential ranges[(f)]. The third set of cycles was performed at low sweep rates. In order to compare the current response of the glassy carbon

[(f)] −0.8 V and 0.5 V, −1.5 V and 0.2 V, −1.2 V and 0.2 V.

rod with- and without $YMn_{1-x}Ti_xO_{3\pm\delta}$ present, cyclic voltammetry was also performed on the rod itself. The nanocrystalline particles were cycled between $-0.8\,V$ and $0.5\,V$

3.8.2 Nanocrystalline $YMnO_3$ supported on mesoporous carbon

The same suspension as in Section 3.7.2 was used, with nanoparticles of $YMnO_3$ loaded onto mesoporous carbon ST8 at 30wt% $YMnO_3$ and suspended at $1\,mg\,mL^{-1}$. The rod electrode was prepared with a total mass loading of $51\,\mu g\,cm^{-2}$ before the cell was carefully filled with N_2(g) purged KOH and assembled. The cell was then purged carefully for 5 more minutes before it was placed under a N_2(g) gas lid. The electrolyte had been purged prior to filling of the cell so that the deposited particles would not be washed away from the glassy carbon during purging. Cyclic voltammetry was performed at various sweep rates with turnaround potentials at $-1.4\,V$ and $0.4\,V$. The current contribution from MC ST8 was also measured by preparing and electrode of the same mass loading that was cycled in the same potential area. This was done for both 1 M and 3 M N_2(g) purged KOH.

3.9 Flat specimen electrode

Sintered discs of bulk $YTi_{0.12}Mn_{0.88}O_{3\pm\delta}$ with a diameter of approximately 20 mm, (as synthesized and polished in Section 3.2) were used as the working electrode. The density and porosity of the discs were approximated after polishing by measuring the height, diameter and weight. A polished disc was placed in a flat specimen electrode with a steel backing plate in order to avoid breaking of the disc. The electrode with the steel backing plate is shown in Figure 3.7. The electrode was placed in the cell as the working electrode. The Pt(s) and Ag/AgCl electrodes were used as the counter and reference electrodes. Cyclic voltammetry was performed with 3 M KOH as the electrolyte.

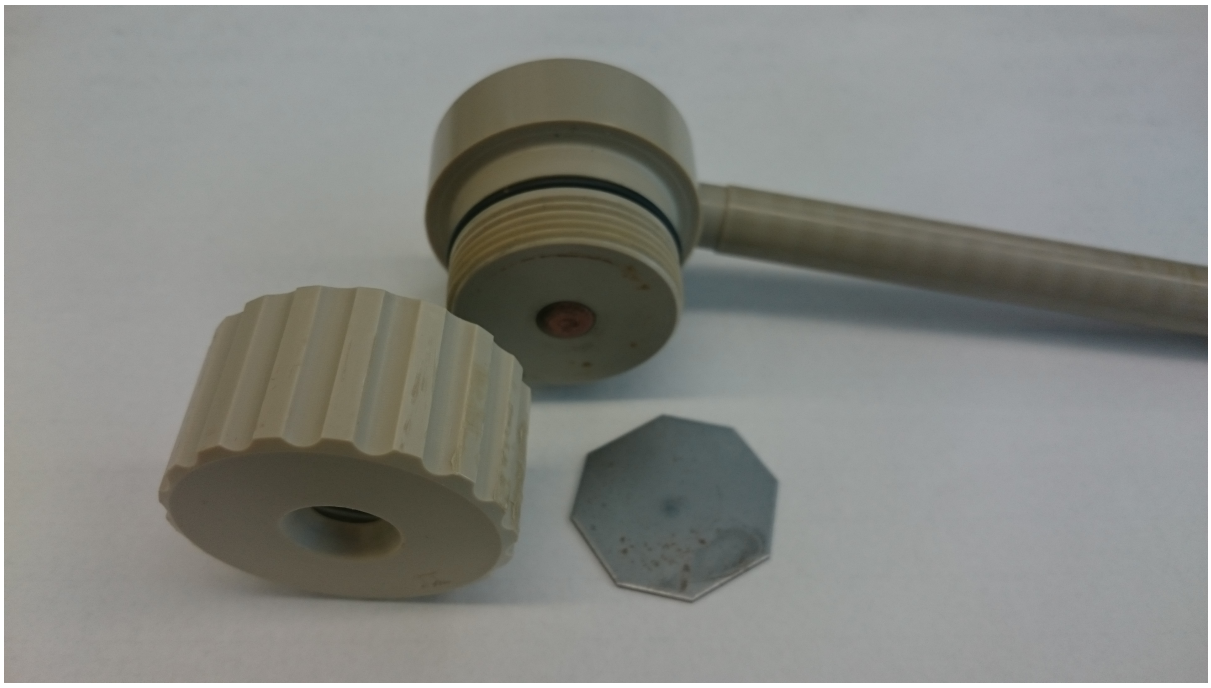

Figure 3.7: The flat specimen electrode, with a steel backing plate.

3.10 SEM and EDS

A polished disc of bulk $YTi_{0.12}Mn_{0.88}O_{3\pm\delta}$ was imaged in a scanning electron microscope (SEM) prior to electrochemical characterization using a Hitachi S-3400 SEM, at low magnification and acceleration voltage. The sieved bulk particles of $YTi_{0.12}Mn_{0.88}O_{3\pm\delta}$ were adhered to a piece of carbon tape and imaged in order to study the morphology and particle size. The glassy carbon RDE electrode was imaged with both bulk $YTi_{0.12}Mn_{0.88}O_{3\pm\delta}$ and nanocrystalline $YTi_{0.15}Mn_{0.85}O_{3\pm\delta}$ deposited at $1\,\mathrm{mg\,cm^{-2}}$ prior to characterization.

A droplet of $YMnO_3$ and mesoporous carbon ST8 was deposited on a small piece of silicon wafer and imaged in a Zeiss Ultra 55 Limited Edition FESEM using the secondary electron detector. The acceleration voltage was 5 kV. This was done in order to find the degree of agglomeration, and how well the oxide was dispersed on the mesoporous carbon surface. Three areas was analysed with EDS at 15 kV in order to confirm the composition of the different particles that could be seen.

3.11 Analysis of the cyclic voltammograms

The current contribution from mesoporous carbon was removed with point-by-point subtraction, using Equation (3.1) where $I(E_t)$ is the current at potential E, which is a function of time t. Each subscript indicates which component the current corresponds to. I_{exp} is the current measured when characterizing $YMnO_3$ loaded onto MC. I_{MC} is then the current measured when characterizing MC without $YMnO_3$ present. Concequently, I_{YM} is the current contribution from $YMnO_3$. The The subtraction was performed using the MATLAB script given in Appendix F.1.

$$I_{YM}(E_t) = I_{\mathrm{exp}}(E_{\mathrm{t}}) - I_{\mathrm{MC}}(E_t) \tag{3.1}$$

Further, the faradic (I_f) and non-faradic (I_{nf}) components of the cyclic voltammograms were separated using Equations (3.2) to (3.5) where I is the current density being separated into it's faradic and non-faradic components, v is the sweep rate in $\mathrm{mV\,s^{-1}}$ and α and β are the faradic- and non-faradic scale factors, respectively. K is the ratio between the faradic and non-faradic currents. It should be pointed out that the currents can be separated regardless of whether the signal from mesoporous carbon has been subtracted. A full derivation of the equations is given in Appendix C.

$$\frac{I}{\sqrt{v}} = \beta\sqrt{v} + \alpha \tag{3.2}$$

$$K = \frac{\beta}{\alpha}\sqrt{v} \tag{3.3}$$

$$I_{nf} = I\frac{K}{1+K} \tag{3.4}$$

$$I_f = I\left(1 - \frac{K}{1+K}\right) \tag{3.5}$$

The value of α and β was found for each point on the curve by linear regression of Equation (3.2), as illustrated in Figure 3.8.

The calculations were performed using MATLAB, with the script given in Appendix F.2.

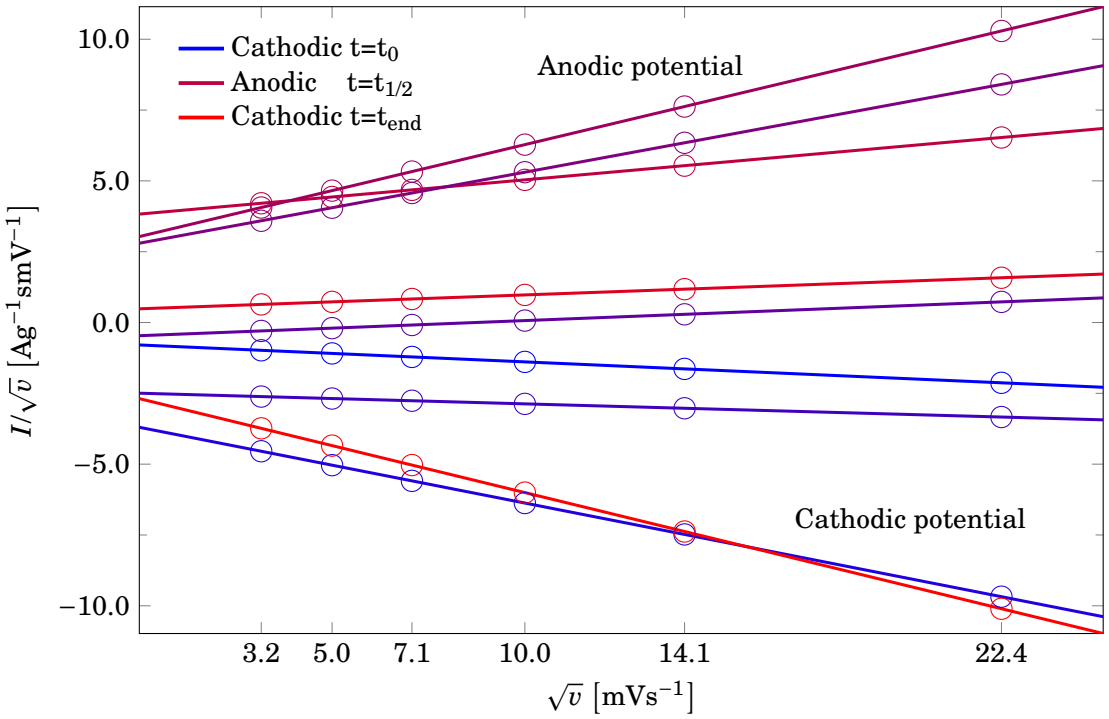

Figure 3.8: Plot of $\frac{I}{\sqrt{v}}$ vs $\sqrt{v}$. The data was taken from the analysis of the results from Section 3.7.2. β is given from the slope of the linear regression, and α is equal to the intersection with the y-axis. Only each 500'th point is shown in this example. The change in colour from blue to red is indicative of the potential moving from the cathodic to the anodic potential, and back again. Whether the slope of the line is negative or positive scales with the sign of the current.

Chapter 4

Results

4.1 Stability in alkaline conditions

Before addition of KOH to the centrifuge tube with bulk $YTi_{0.12}Mn_{0.88}O_{3\pm\delta}$, the total weight was m_1 =16.1191 g. After rinsing the powder with DI water through centrifugation and decanting ten times, and drying at 50 °C over night, the total weight was m_2 =16.1074 g. The smallest particles did not separate from the water phase, as shown in Figure 4.1. These particles were lost. The weight difference before and after the stability test was 0.0117 g. With 1.8653g bulk $YTi_{0.12}Mn_{0.88}O_{3\pm\delta}$ as the initial amount in the centrifuge tube, the weight loss corresponds to a weight percentage of 0.63%.

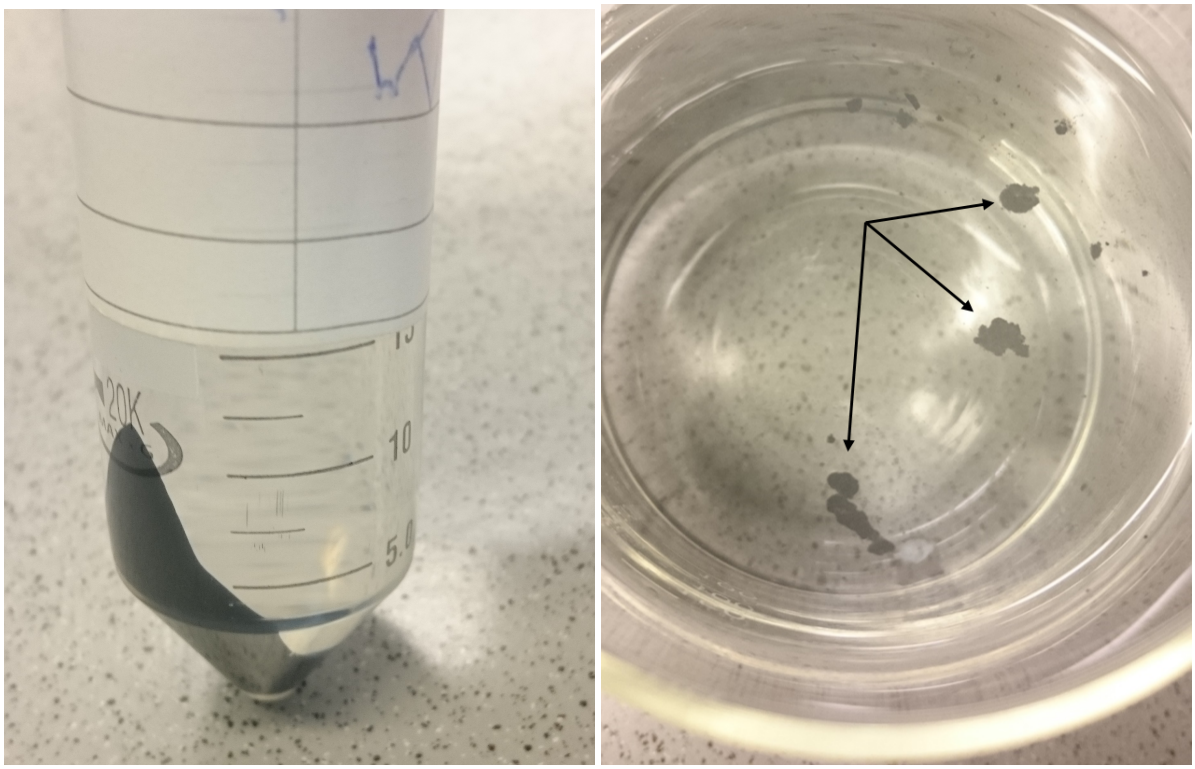

(a) **(b)**

Figure 4.1: The bulk particles after centrifugation of the suspension (**a**). A small amount of particles was lost during decanting (**b**).

Washing of the carbon tape that had been submerged in 3 M KOH for four days resulted in the disintegration of the carbon tape. In Figure 4.2, small pieces of carbon tape can be seen floating around in the DI water. It was not possible to use the material for further XRD analysis.

The X-ray diffraction pattern and Rietveld refinement of $YTi_{0.12}Mn_{0.88}O_{3\pm\delta}$ after the stability test are shown in Section 4.2 and compared to that of as-synthesized bulk power, showing that no phase transition had occurred.

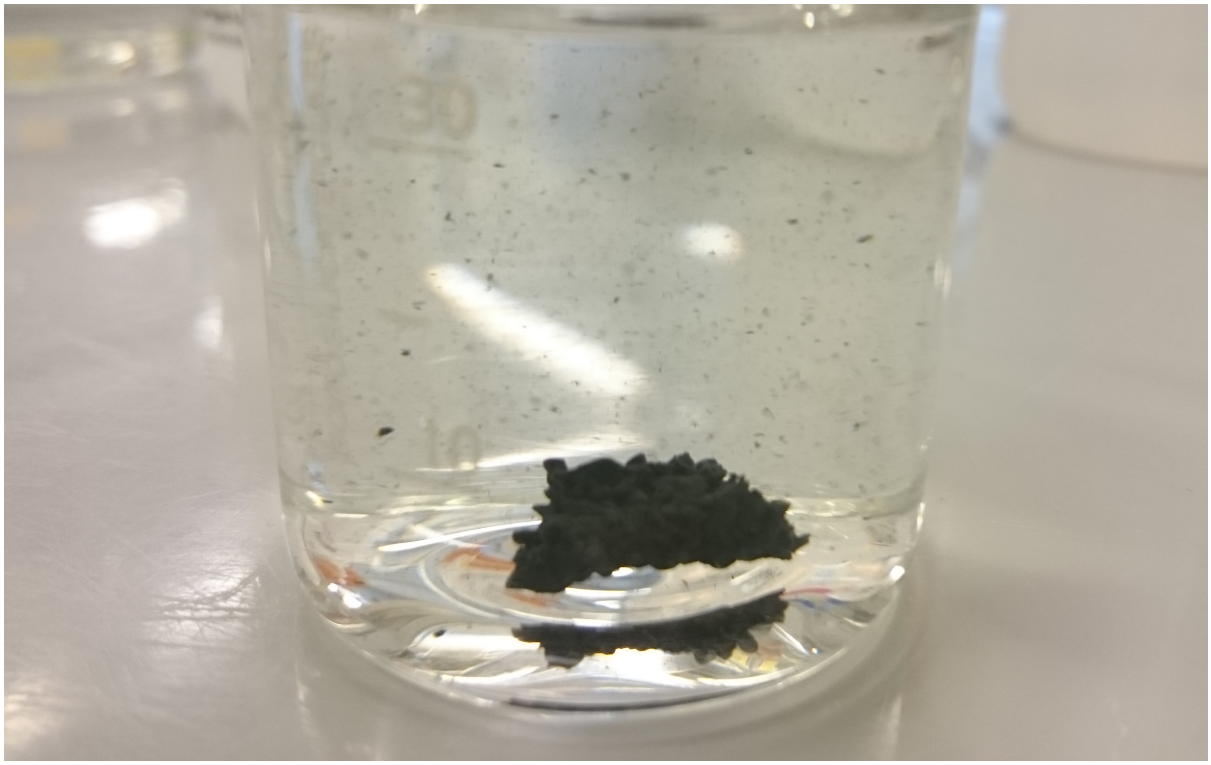

Figure 4.2: The failed attempt at testing the stability of the hexagonal phase of nanocrystalline $YTi_{0.15}Mn_{0.85}O_{3\pm\delta}$ in alkaline conditions. Particles of carbon tape can be seen floating around in the DI water.

4.2 X-ray diffraction and Rietveld refinement

The refined XRD-patterns of bulk $YTi_{0.12}Mn_{0.88}O_{3\pm\delta}$ before and after the stability test are shown in Figure 4.3. The as-measured data are shown together with the refinement in Appendix E. It is evident that no phase transition had occurred when bulk particles were suspended in 3 M KOH for 4 days. As expected from the XRD-pattern in Figure 2.7 the peak at $2\theta \approx 23°$ is almost completely gone when x=0.12 in $YMn_{1-x}Ti_xO_{3\pm\delta}$.

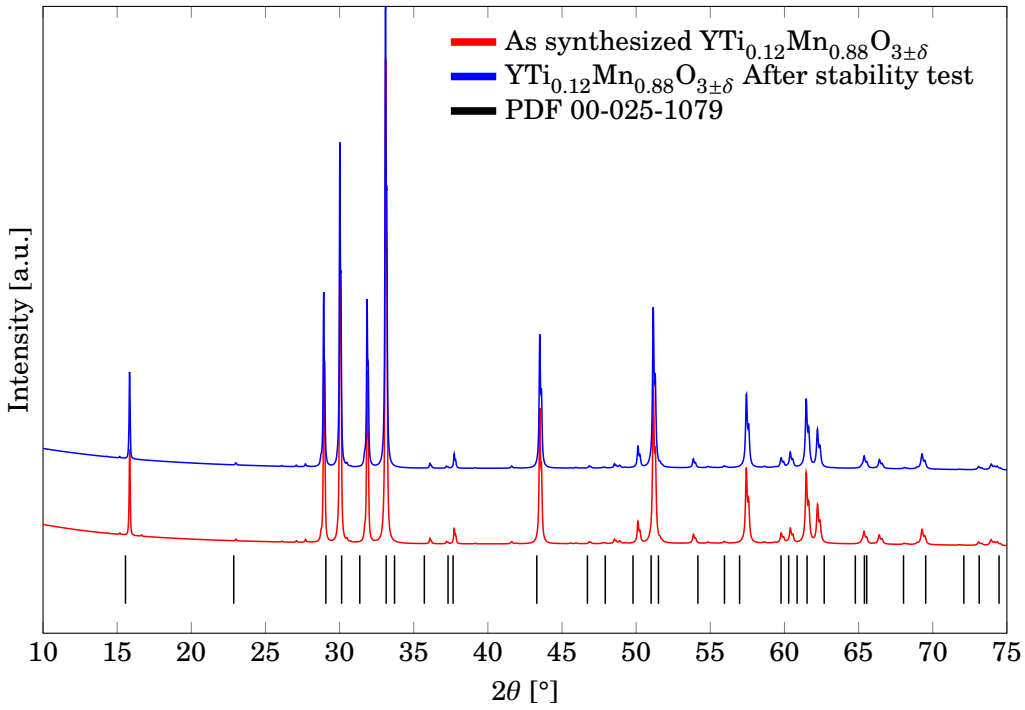

Figure 4.3: Rietveld refined diffraction patterns of bulk $YTi_{0.12}Mn_{0.88}O_{3\pm\delta}$ before and after stability test. Both refinements converged at unit cell parameters a=6.19 Å and c=11.27 Å

The refined atomic positions of the bulk samples are shown in Tables 4.1 and 4.2.

Table 4.1: Rietveld refined lattice sites of bulk $YTi_{0.12}Mn_{0.88}O_{3\pm\delta}$

Site	Np	x	y	z	Atom	Occ	Beq
Y1	2	0.00000	0.00000	0.265(2)	Y+3	1	1
Y2	4	0.33333	0.66667	0.250(2)	Y+3	1	1
Mn	6	0.331(5)	0.00000	0.00000	Mn+3	0.88	1
					Ti+4	0.12	1
O1	6	0.279(10)	0.00000	0.127(4)	O-2	1	1
O2	6	0.678(11)	0.00000	0.339(5)	O-2	1	1
O3	2	0.00000	0.00000	0.465(12)	O-2	1	1
O4	4	0.33333	0.66667	-0.032(7)	O-2	1	1

The refined atomic positions of the nanocrystalline samples are shown in Tables 4.3 and 4.4.

The unit cell parameters of all four samples are given in Table 4.5. The unit cell parameters of bulk $YTi_{0.12}Mn_{0.88}O_{3\pm\delta}$ before and after suspension in 3 M KOH was approximately equal.

The experimental and refined XRD patterns are shown in Appendix E.

Table 4.2: Rietveld refined lattice sites of bulk $YTi_{0.12}Mn_{0.88}O_{3\pm\delta}$ after stability test

Site	Np	x	y	z	Atom	Occ	Beq
Y1	2	0.00000	0.00000	0.2460(9)	Y+3	1	1
Y2	4	0.33333	0.66667	0.2606(8)	Y+3	1	1
Mn	6	0.333(18)	0.00000	0.00000	Mn+3	0.88	1
					Ti+4	0.12	1
O1	6	0.343(10)	0.00000	0.1358(14)	O-2	1	1
O2	6	0.679(10)	0.00000	0.3339(16)	O-2	1	1
O3	2	0.00000	0.00000	0.468(4)	O-2	1	1
O4	4	0.33333	0.66667	-0.026(3)	O-2	1	1

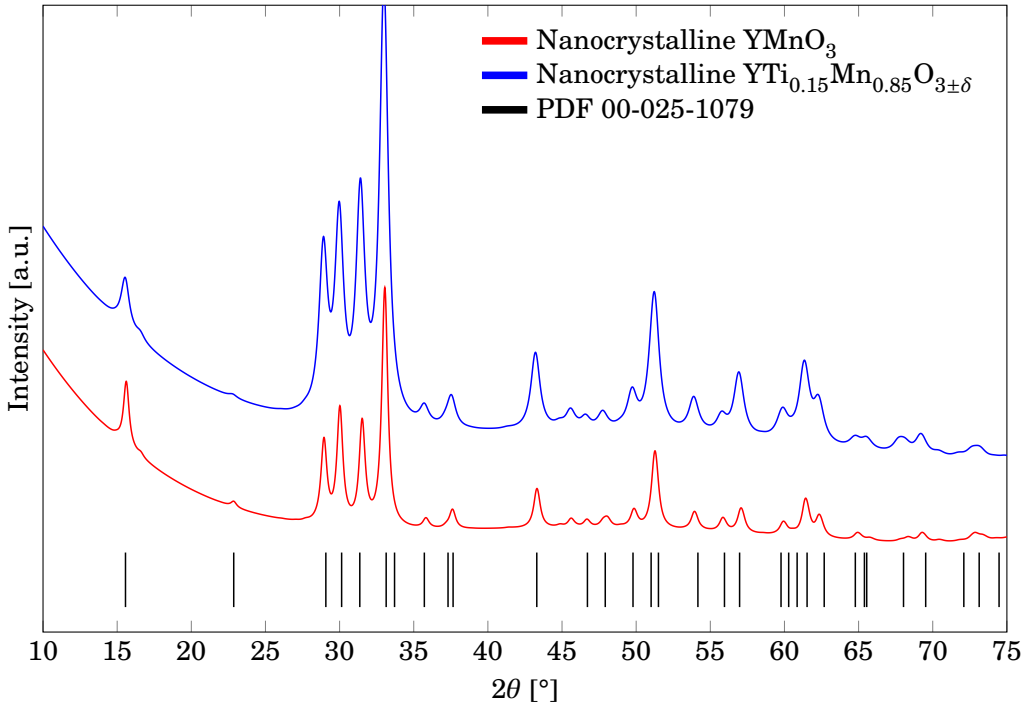

Figure 4.4: Rietveld refined diffraction patterns of nanocrystalline $YMnO_3$ and $YTi_{0.15}Mn_{0.85}O_{3\pm\delta}$, deposited on a Si single crystal. The refinements converged at at unit cell parameters a=6.17 Å, c=11.36 Å and a=6.18 Å, c=11.39 Å, respectively Average crystallite size, by peak shape function was d_L=19.5 nm and d_L = 13.8 nm, respectively.

Table 4.3: Rietveld refined lattice sites of nanocrystalline $YTi_{0.15}Mn_{0.85}O_{3\pm\delta}$

Site	Np	x	y	z	Atom	Occ	Beq
Y1	2	0.00000	0.00000	0.2671(16)	Y+3	1	1
Y2	4	0.33333	0.66667	0.2346(14)	Y+3	1	1
Mn	6	0.2674(19)	0.00000	0.00000	Mn+3	0.85	1
					Ti+4	0.15	1
O1	6	0.337(9)	0.00000	0.177(2)	O-2	1	1
O2	6	0.559(5)	0.00000	0.504(4)	O-2	1	1
O3	2	0.00000	0.00000	0.645(5)	O-2	1	1
O4	4	0.33333	0.66667	-0.013(7)	O-2	1	1

Table 4.4: Rietveld refined lattice sites of nanocrystalline $YMnO_3$

Site	Np	x	y	z	Atom	Occ	Beq
Y1	2	0.00000	0.00000	0.2542(19)	Y+3	1	1
Y2	4	0.33333	0.66667	0.2192(16)	Y+3	1	1
Mn	6	0.303(2)	0.00000	0.00000	Mn+3	1	1
O1	6	0.224(5)	0.00000	0.210(4)	O-2	1	1
O2	6	0.661(10)	0.00000	0.346(3)	O-2	1	1
O3	2	0.00000	0.00000	0.625(7)	O-2	1	1
O4	4	0.33333	0.66667	0.011(3)	O-2	1	1

Table 4.5: The refined unit cell parameters of all the samples used. Each set of parameters correspond to the refined atomic positions in Tables 4.1 to 4.4

Sample	a [Å]	c [Å]	Note
$YTi_{0.12}Mn_{0.88}O_{3\pm\delta}$	6.19241 ± 0.00011	11.2706 ± 0.0002	As synthesized
$YTi_{0.12}Mn_{0.88}O_{3\pm\delta}$	6.19396 ± 0.00017	11.2700 ± 0.0003	After stability test
$YTi_{0.15}Mn_{0.85}O_{3\pm\delta}$	6.1753 ± 0.0014	11.392 ± 0.003	Nanocrystalline
$YMnO_3$	6.1734 ± 0.0012	11.363 ± 0.003	Nanocrystalline

4.3 Cyclic voltammetry

Initially, some time had to be used for troubleshooting of the electrochemical equipment. The troubleshooting process is described in Appendix A. When a voltammogram of a platina RDE in 1 M KOH was successfully recorded (fig. 4.5), the equipment was deemed as functional. The curve had the characteristic shape equal to that in Figure 2.9b and earlier work[6].

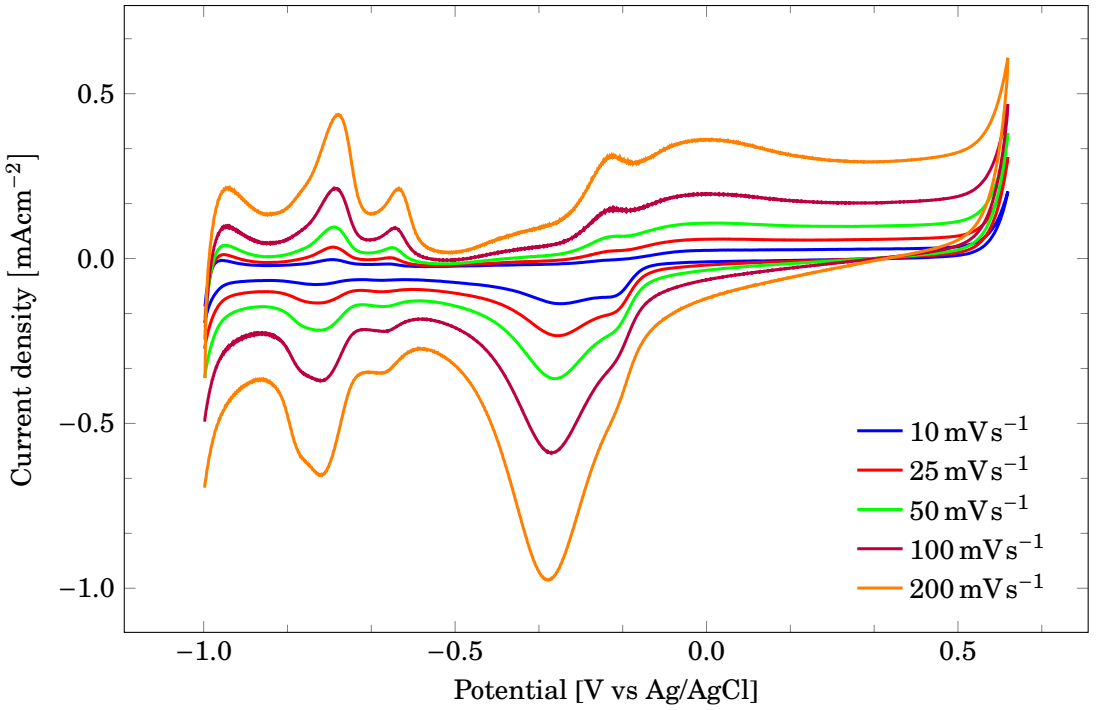

,

Figure 4.5: Voltammogram of a platina RDE in 1 M KOH at different sweep rates. The curves match those measured in earlier work[6], indicating that all the components in the electrochemical setup was functional

The most promising electrochemical response was achieved using the GC rod to characterize nanocrystalline $YMnO_3$ on mesoporous carbon ST8. In the following sections, the voltammograms produced from the different electrodes will be presented in chronological order. Areas of interest in the figures are pointed out for better clarity. A few initial attempts at using C-tape for adhesion of both particles and pellets to the RDE, as well as attempts to hot-press composite electrodes of mesoporous carbon and $YMnO_3$ are presented in Appendix B.

4.4 Glassy carbon RDE

Without a binder, the bulk particles would not adhere sufficiently well to the glassy carbon surface. Upon lowering of the electrode into the electrolyte, the particles fell off immediately. The nanocrystalline particles adhered a little, but would slowly fall. This also occurred for nanocrystalline particles supported on mesoporous carbon. All attempts to gently wash the used electrode with DI water were unsuccessful. The particles were swept away by the water. Due to the insufficient adhesive properties of particles deposited directly on glassy carbon, repeating the measurements in N_2(g) purged electrolyte was not given high priority.

4.4.1 Bulk $YTi_{0.12}Mn_{0.88}O_{3\pm\delta}$

The voltammogram recorded for bulk $YTi_{0.12}Mn_{0.88}O_{3\pm\delta}$ on the GCRDE in 3 M KOH is shown in Figure 4.6. There are no clearly discernible peaks in the measurements. The increasing slope of the curves are probably due to uncompensated ohmic resistance.

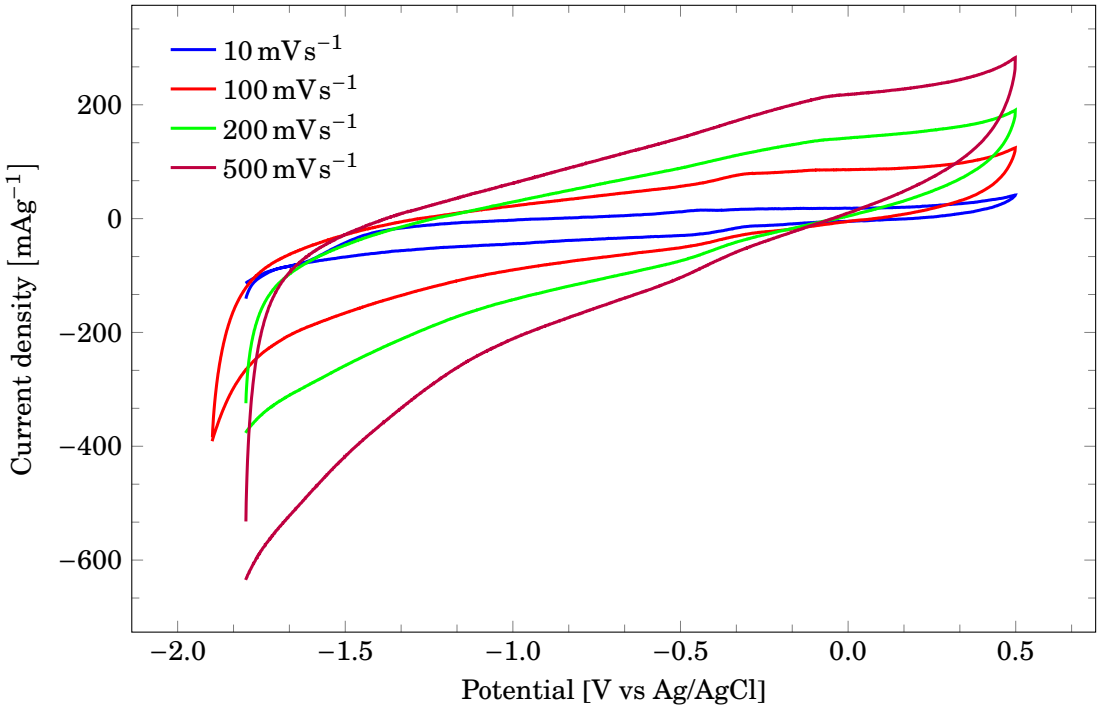

Figure 4.6: Cyclic voltammogram of bulk $YTi_{0.12}Mn_{0.88}O_{3\pm\delta}$ deposited on a glassy carbon RDE. Measured in 3 M KOH. The deposited particles adhered insufficiently to the glassy carbon surface, and fell off upon contact with the electrolyte

4.4.2 Nanocrystalline $YTi_{0.15}Mn_{0.85}O_{3\pm\delta}$

The CV curves for both depositions of nanoparticles are shown in Figure 4.7. At high sweep rates, there are no clearly discernible peaks.

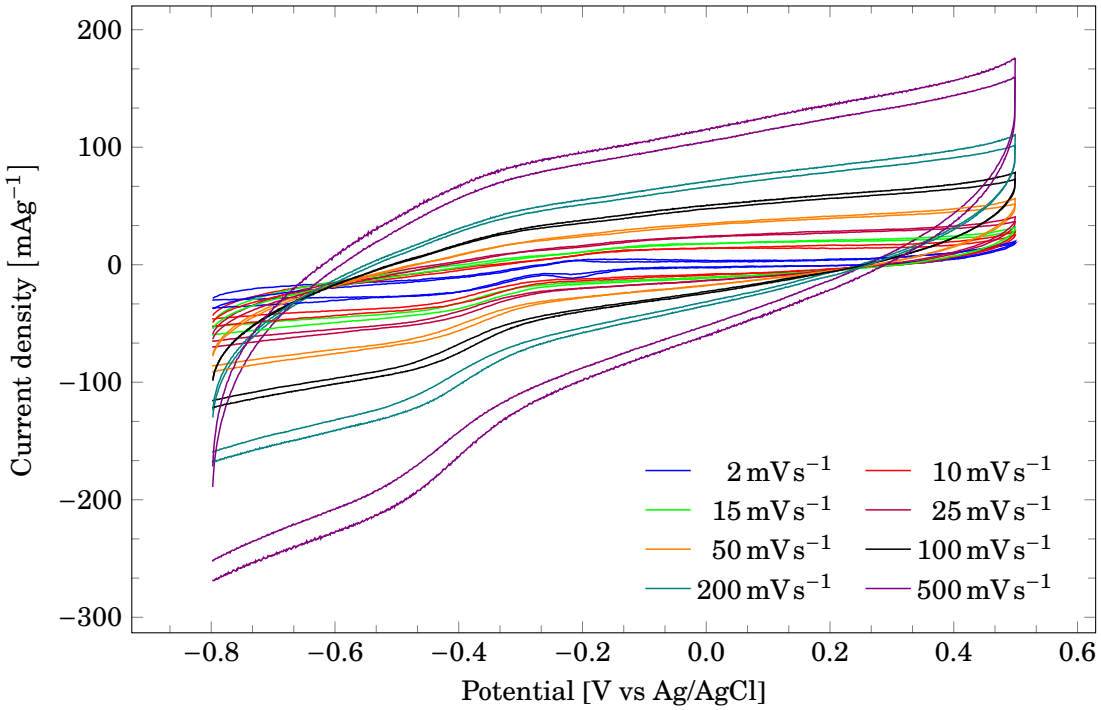

Figure 4.7: Voltammogram if nanocrystalline $YTi_{0.15}Mn_{0.85}O_{3\pm\delta}$ deposited on a glassy carbon RDE. 3 M KOH was used as the supporting electrolyte. Two depositions are shown, where deposition and cyclic voltammetry were performed identically. I.e. the sweeps were performed with increasing sweep rate. At the lowest sweep rate (2 mV s^{-1}), there are both anodic and cathodic peaks.

The voltammogram for the narrow-potential scan of the second nanocrystalline electrode is shown in Figure 4.8, and do not show any redox features at high sweep rates.

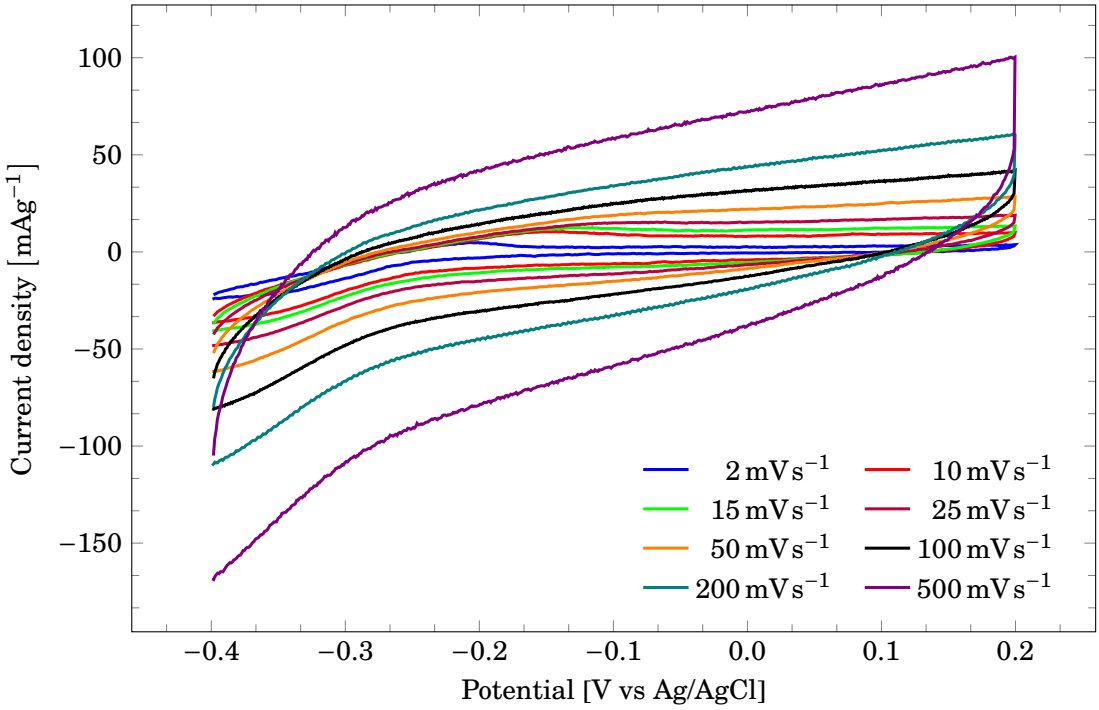

Figure 4.8: In order to eliminate the possibility of gaseous evolution on the electrode, a narrow potential sweep was performed on a newly deposited electrode of nanocrystalline $YTi_{0.15}Mn_{0.85}O_{3\pm\delta}$ on glassy carbon. At the lowest sweep rate ($2\,mV\,s^{-1}$), there are both anodic and cathodic peaks.

In Figures 4.7 and 4.8, a cathodic peak is present around −250 mV at sweep rate 2 $mV s^{-1}$, but not at higher rates. The peak is shown in Figures 4.9 to 4.11. The magnitude of the peak is reduced for each cycle.

In Figures 4.9 and 4.10, there are possibly a corresponding anodic peak that shifts to slightly more positive potentials for each cycle. A cathodic peak that was reduced in magnitude for each cycle was also observed in earlier work [6] for nanoparticles of $YMnO_3$ supported on mesoporous carbon, where it was not an artefact of dissolved gaseous oxygen, but rather hydroxide ions.

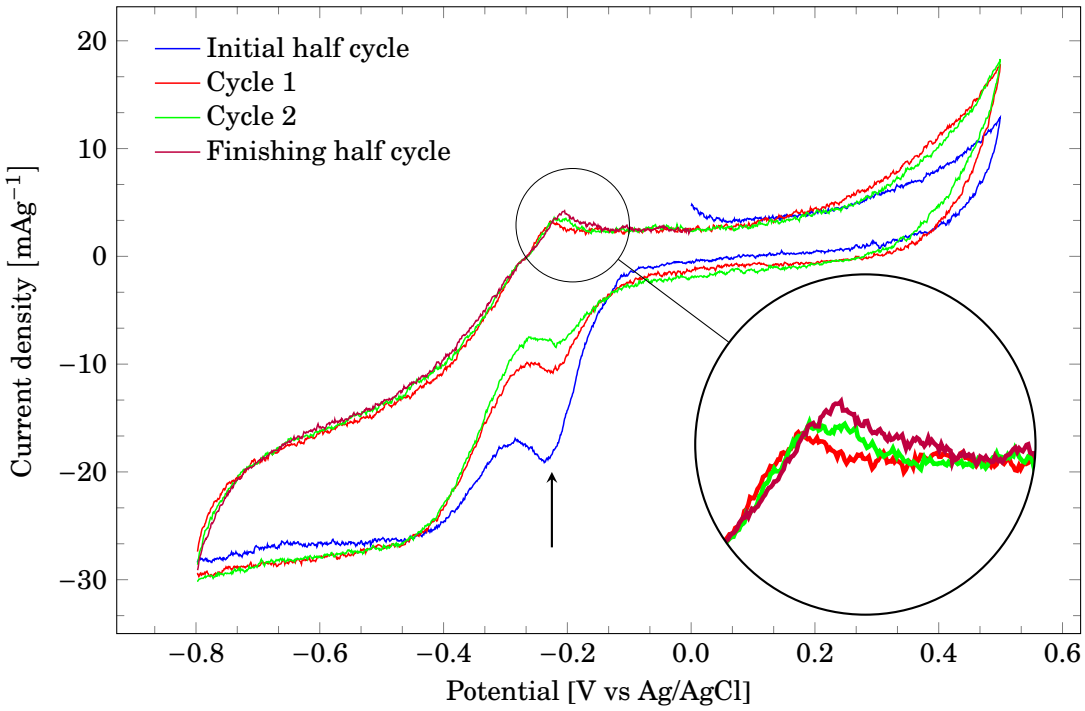

Figure 4.9: Cyclic voltammogram of nanoparticles of $YTi_{0.15}Mn_{0.85}O_{3\pm\delta}$ deposited on a glassy carbon RDE. It can be seen very clearly that the cathodic peak around −250 mV is reduced in magnitude for each cycle. No gaseous evolution was observed, but it could be seen that the particles fell off the electrode. The reduction in peak current is most likely caused by loss of active material at the electrode. The magnified area shows that the peak in the anodic direction shifts to slightly more positive potentials for each cycle. Voltammogram recorded in 3 M KOH at 2 $mV s^{-1}$

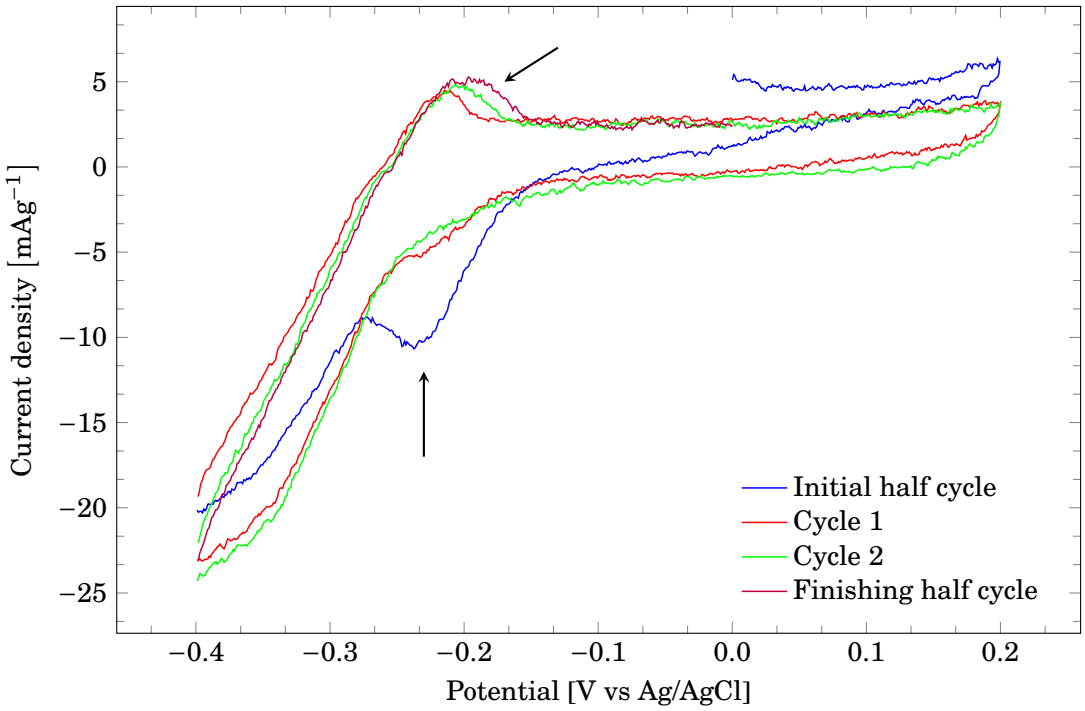

Figure 4.10: Cyclic voltammogram of nanoparticles of $YTi_{0.15}Mn_{0.85}O_{3\pm\delta}$ deposited on a glassy carbon RDE. The same trend as in Figure 4.9 can be seen here, with a reduced cathodic peak current for each cycle. Voltammogram recorded on 3 M KOH at 2 mV s^{-1}. An anodic peak that shifts towards more positive potentials for each cycle can also be observed.

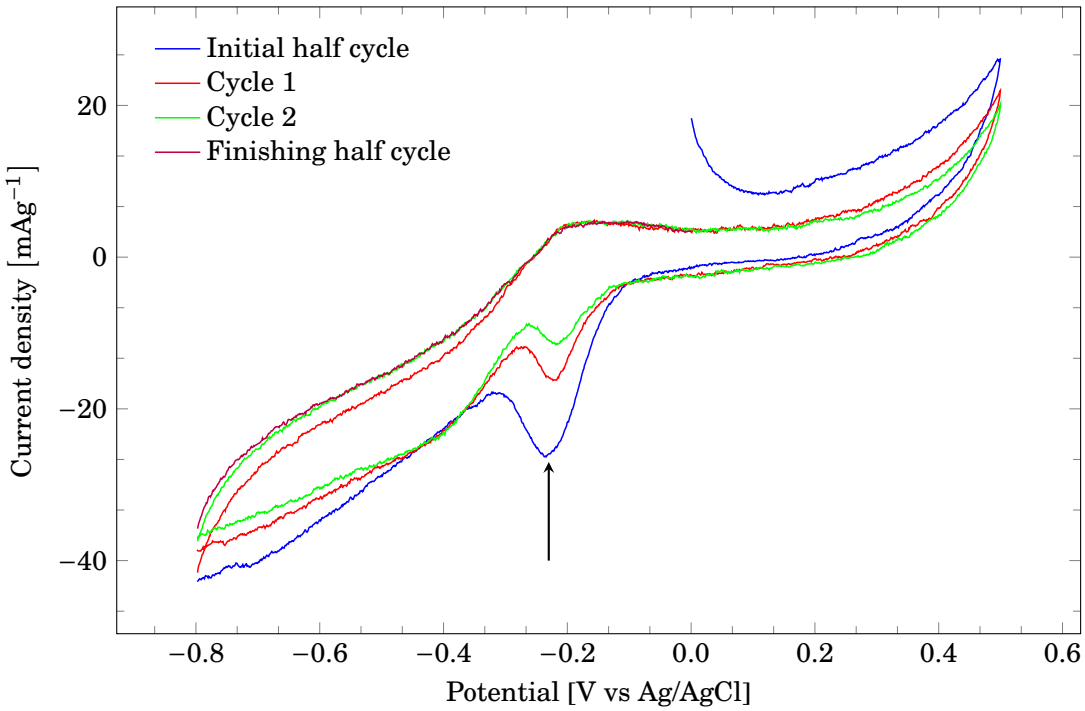

Figure 4.11: A new deposit of nanoparticles of $YTi_{0.15}Mn_{0.85}O_{3\pm\delta}$ were made at the glassy carbon RDE, and the sweeps in Figure 4.9 were repeated. The same trend can be seen in the cathodic direction, with a reduced peak current for each cycle. The shape of the cathodic end of the curve is different than that of Figure 4.9, with a changing versus constant current. Voltammogram recorded in 3 M KOH at 2 mV s^{-1}

4.4.3 Nanocrystalline $YMnO_3$ supported on mesoporous carbon ST8

The electrochemical response of nanocrystalline $YMnO_3$ supported on mesoporous carbon ST8 had both anodic and cathodic peaks when deposited on the glassy carbon RDE, as seen in Figure 4.12. The cathodic and anodic peaks are pointed out as P_a and P_c.

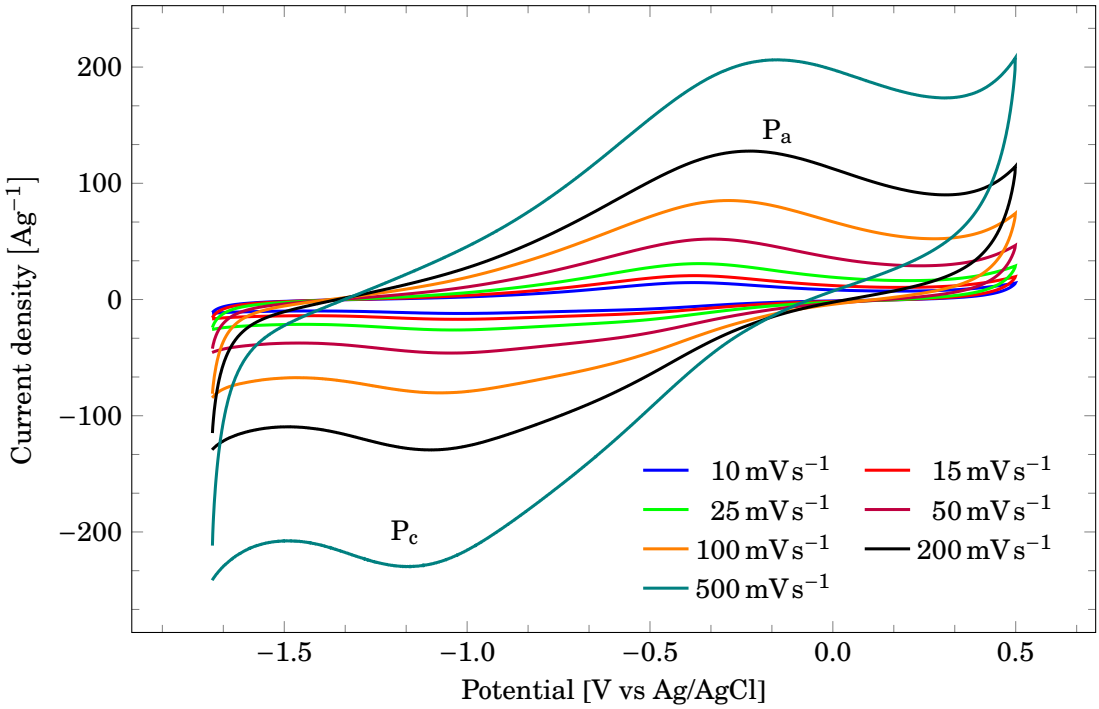

Figure 4.12: Cyclic voltammogram of nanoparticles of $YMnO_3$ supported on mesoporous carbon at 30wt% $YMnO_3$. Measurements were performed in N_2(g) purged 3 M KOH. The peaks have been marked as P_a and P_c

By performing sweeps with an increasing cathodic turnaround potential (E_c)[(a)], it became clear that the anodic peak shifted to more positive potentials as the cathodic turnaround potential increased, as can be seen in Figure 4.13. The cathodic peak did not shift. The sweep with E_c=−1.9 V was performed after those in Figure 4.12, whereas E_c=−1.5 V and E_c=−1.6 V was performed before. The curve with E_c=−1.7 V is from Figure 4.12.

The very first scan that was performed on the electrode after deposition is shown in Figure 4.14. The shape if the curve is significantly different than for those performed afterwards. The cycle with E_c=−1.5 V in Figure 4.13 was the second scan performed on the electrode.

The transition from the curve shape in Figure 4.14 to that in the other figures was abrupt from the last cycle at 10 mV s^{-1} to the first cycle at 100 mV s^{-1}. During the first scan, the peak shape of the curve changed gradually from a plateau-peak towards a single peak, centred between the original plateau and peak, as seen in the magnified area of Figure 4.15.

Two attempts were made to measure the background current of mesoporous carbon. In both cases, the cathodic current took a dive between −1 V and −1.5 V and it appeared that deposited particles began to swell and fall off the GC surface. This current response is shown in Figure 4.16.

[(a)] −1.5 V, −1.6 V, −1.7 V and −1.9 V.

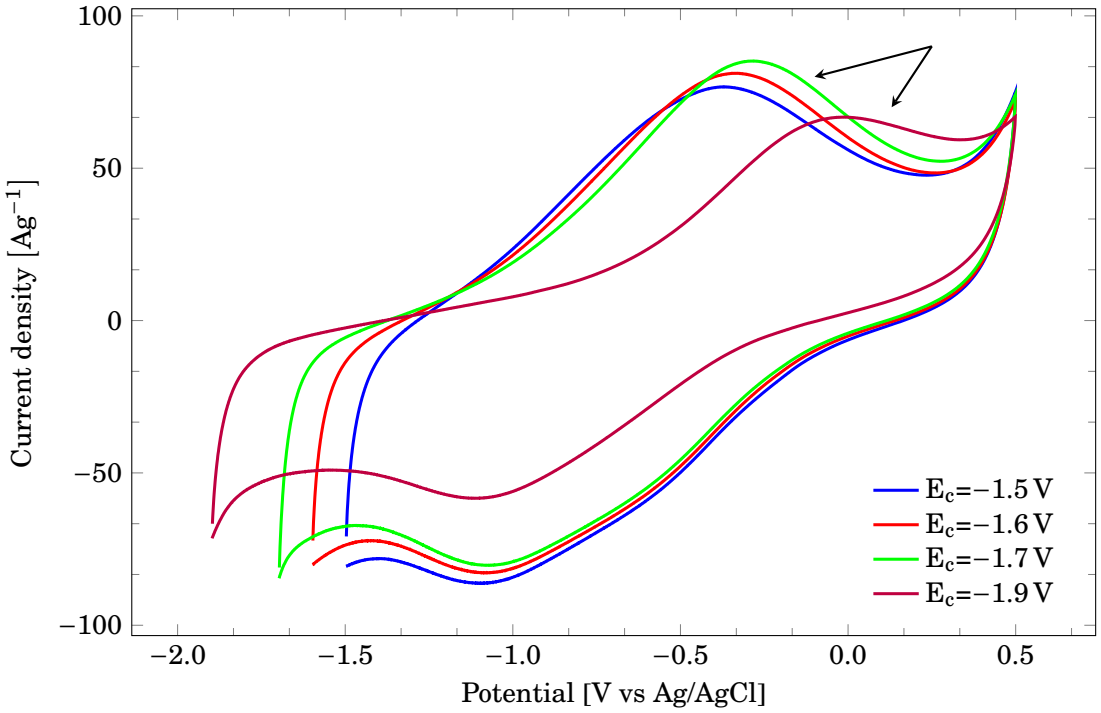

Figure 4.13: Cyclic voltammograms of 30wt% nanoparticles of $YMnO_3$ supported on mesoporous carbon in N_2(g)-purged 3 M KOH at a sweep rate of 100 mV s^{-1}. The anodic peak shifts to more positive potentials as the potential window is increased, while the cathodic peak does not. The first three cycles with a cathodic turnaround potential of E_c=-1.5, -1.6 and −1.7 V were performed in succession. The last cycle, E_c=−1.9 V, was performed after the electrode had been cycled between −1.7 V and 0.5 V at various sweep rates(fig. 4.12).

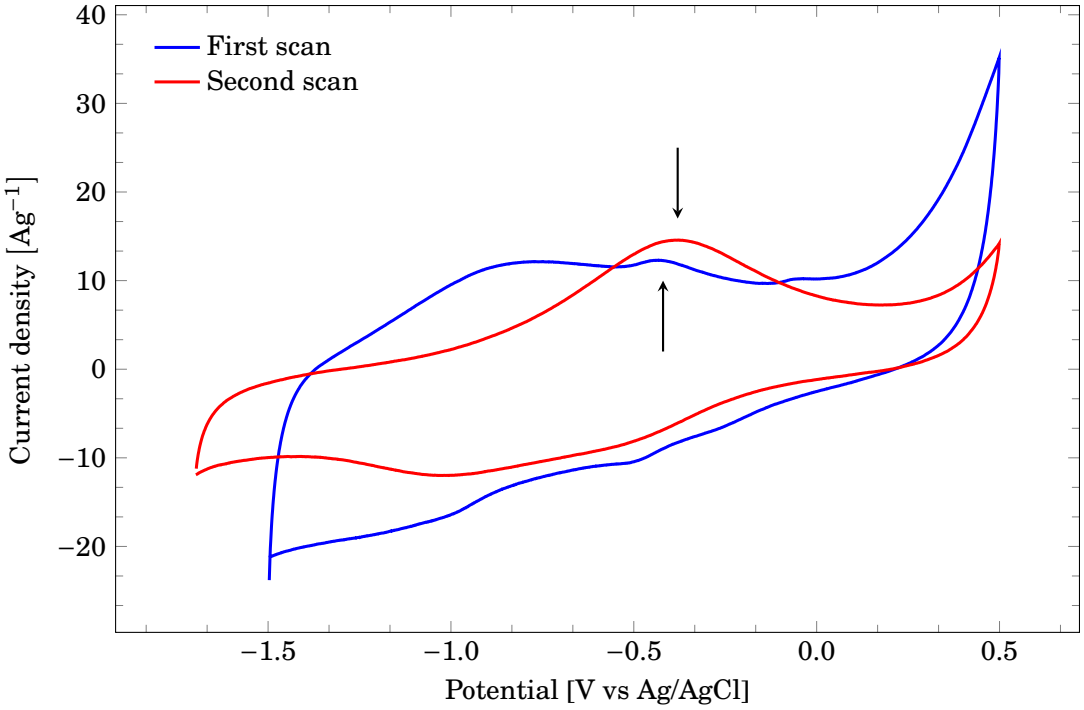

h!]

Figure 4.14: Cyclic voltammogram of 30wt% nanoparticles of $YMnO_3$ supported on mesoporous carbon in N_2(g) purged 3 M KOH at a sweep rate of 10 mV s^{-1}. The curve with a cathodic limit of -1.7V is the same as in Figure 4.12. The curve with a cathodic limit of −1.5 V was measured prior to the curves in Figure 4.12.

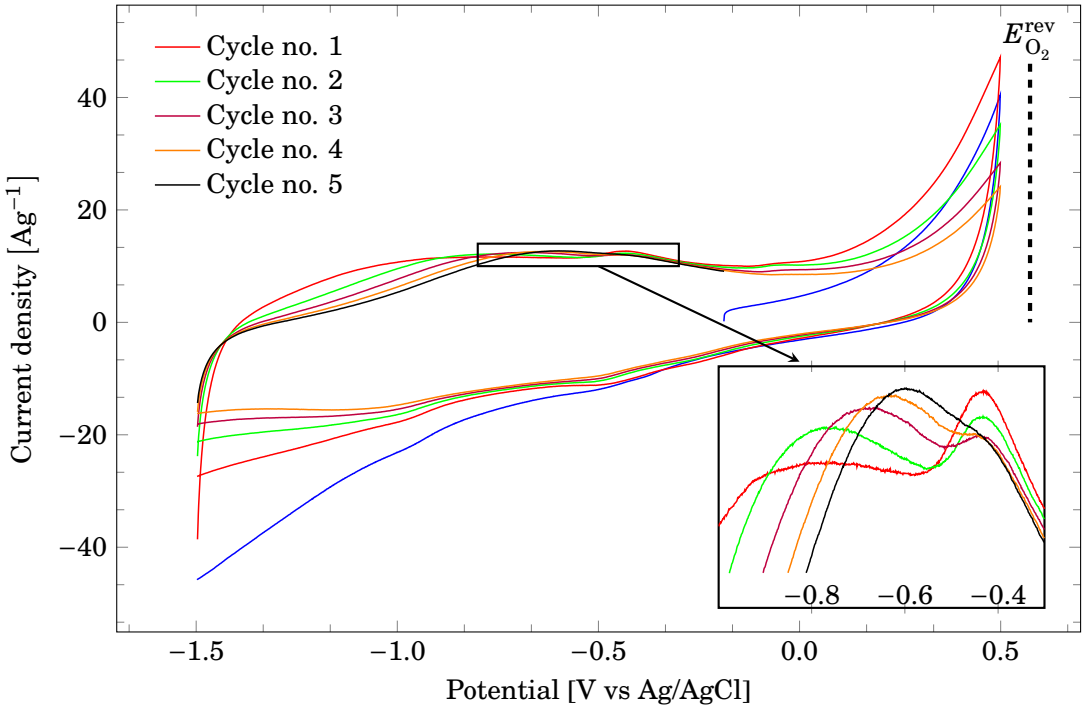

Figure 4.15: During the first cycles of the electrode of nanoparticles of $YMnO_3$ supported on mesoporous carbon, the peak characteristics of the curve changed gradually for each cycle. The magnified area changed from a plateau-peak into a single peak. The final peak was centred in the middle of the first plateau and peak.

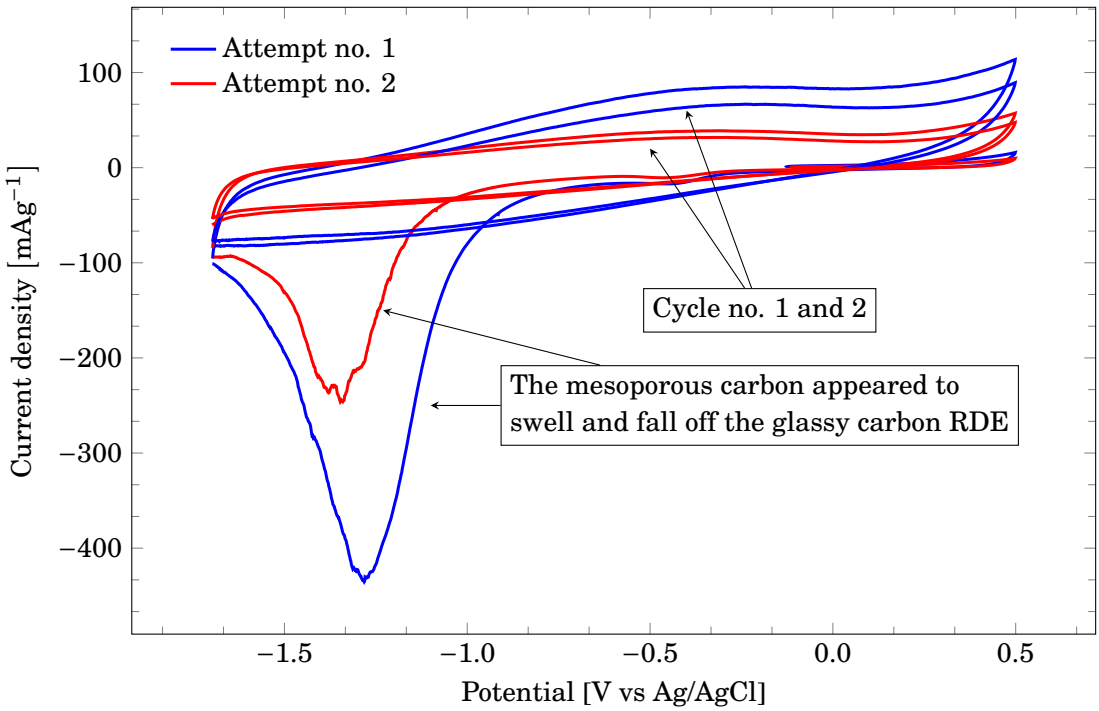

Figure 4.16: Cyclic voltammogram of mesoporous carbon in N_2(g) purged 3 M KOH. During the first cycle in both depositions, the cathodic current increased rapidly in magnitude after −1 V, and the carbon fell off the electrode.

4.4.4 Nanocrystalline $YMnO_3$ supported on mesoporous carbon ST3

When mesoporous carbon ST3 was used, the current response changed. Figure 4.17 shows the current response when nanocrystalline $YMnO_3$ loaded on mesoporous carbon ST3 at 30wt% $YMnO_3$ was deposited at the GCRDE at total mass loadings $51\,\mu g\,cm^{-2}$ and $102\,\mu g\,cm^{-2}$ and cycled between $-1.5\,V$ and $0.5\,V$ at $10\,mV\,s^{-1}$ and $100\,mV\,s^{-1}$ in N_2(g) purged 3 M KOH. A second deposit was made at $102\,\mu g\,cm^{-2}$ and cycled between $-1.4\,V$ and $0.5\,V$ at $10\,mV\,s^{-1}$ and then $5\,mV\,s^{-1}$. The current increased with an increased total mass loading.

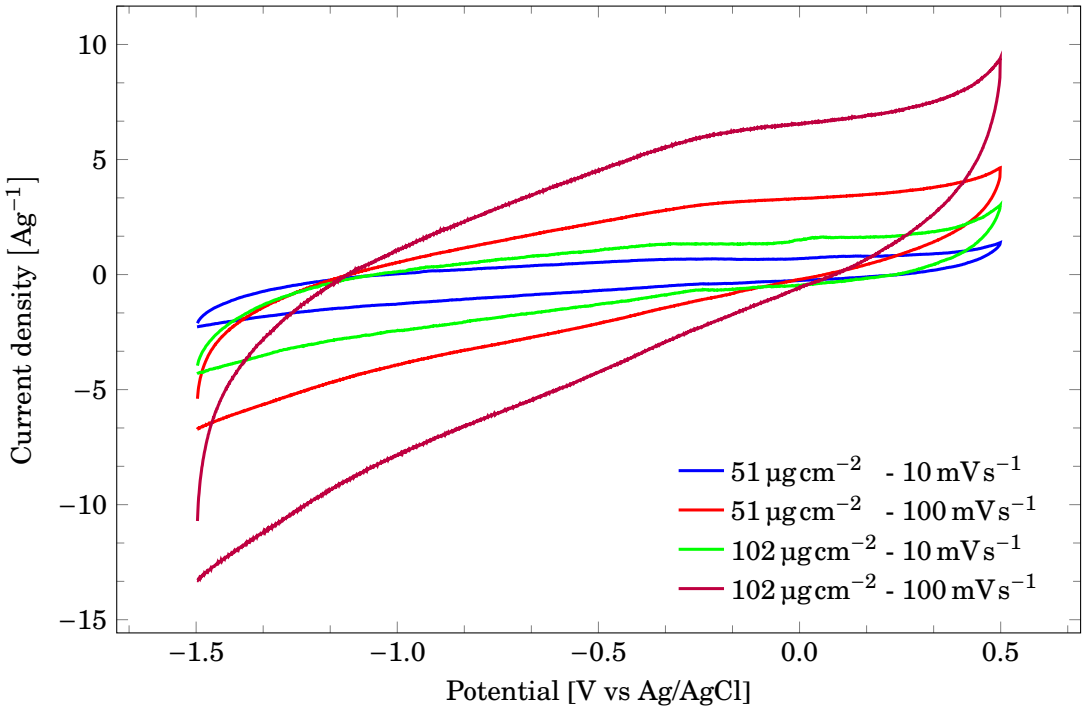

Figure 4.17: Cyclic voltammogram of nanocrystalline $YMnO_3$ supported on mesoporous carbon type ST3, deposited on a glassy carbon RDE at total mass loadings $51\,\mu g\,cm^{-2}$ and $102\,\mu g\,cm^{-2}$. The electrode was cycled between $-1.5\,V$ and $0.5\,V$ in 3 M KOH at $10\,mV\,s^{-1}$ and $100\,mV\,s^{-1}$.

An oxidation plateau, as in Figure 2.10, might be present for the deposition at $102\,\mu g\,cm^{-2}$. As seen in Figure 4.18, an anodic peak around 0 V is both preceded and followed by a by an area that might be considered a plateau. There is also a cathodic return peak around $-0.25\,V$.

Plotting all the cycles at $10\,mV\,s^{-1}$ from Figure 4.18 in Figure 4.19 revealed that the peak intensity decreased for each cycle.

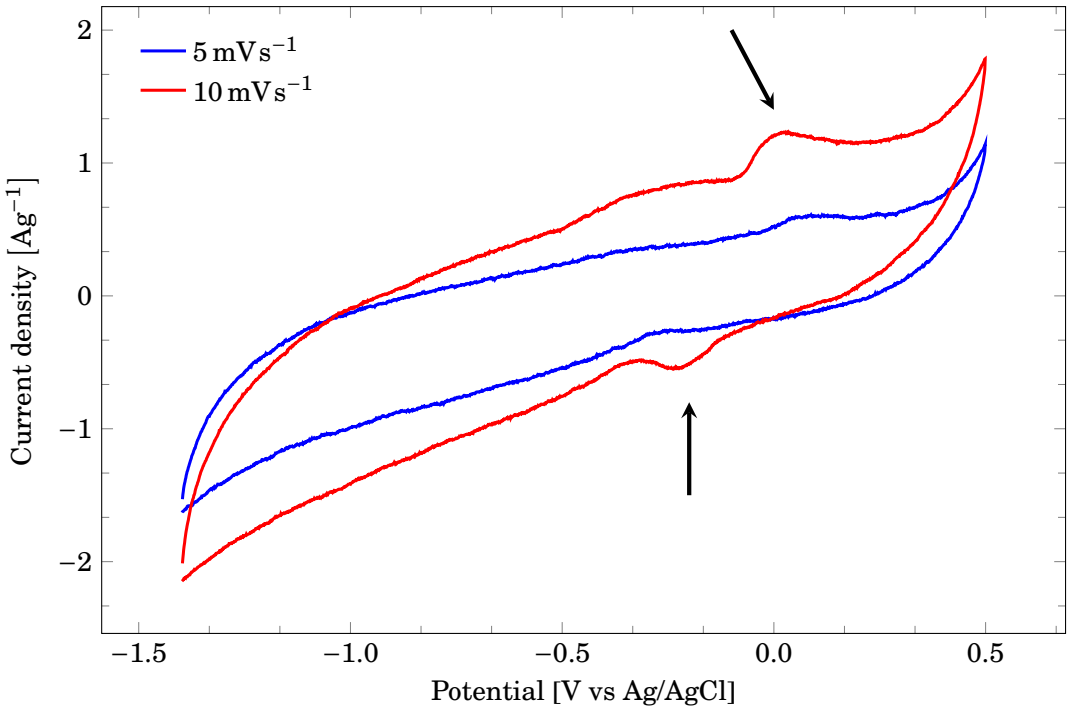

Figure 4.18: Cyclic voltammogram of nanocrystalline $YMnO_3$ supported on mesoporous carbon ST3, deposited on a glassy carbon RDE at total mass loading 102 µg cm^{-2}. The electrode was cycled between −1.4 V and 0.5 V in 3 M KOH at 5 mV s^{-1} and 10 mV s^{-1}. An anodic-cathodic redox couple can be seen clearly with $E_{1/2} \approx -0.1$ V.

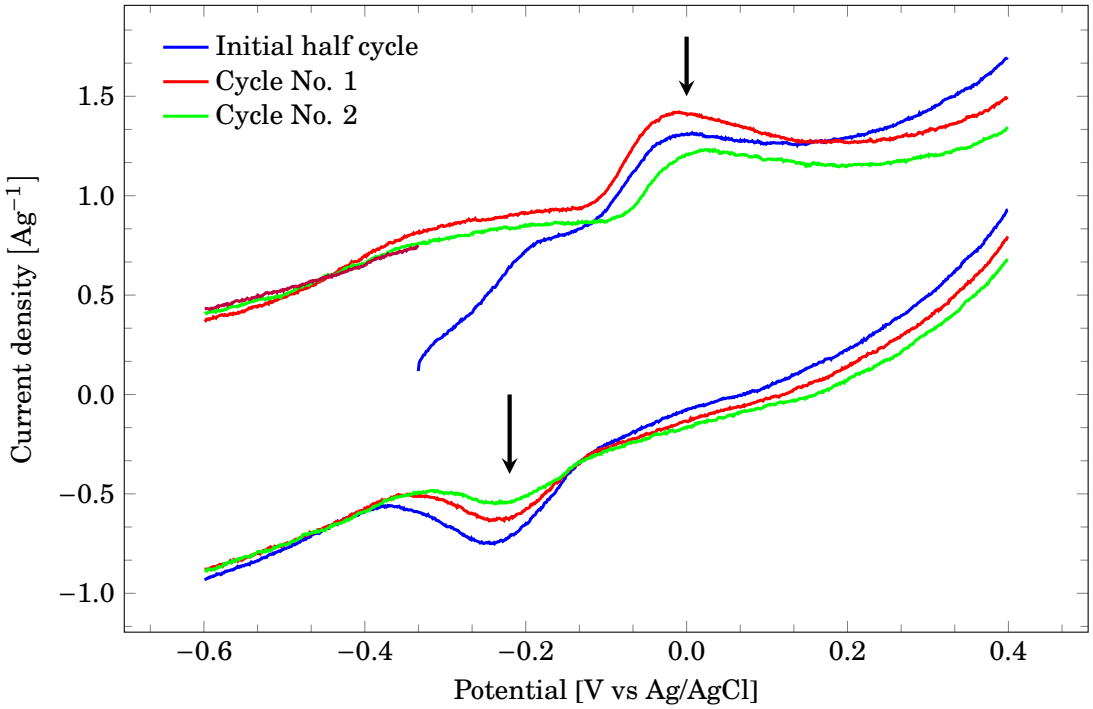

Figure 4.19: Cyclic voltammogram of nanocrystalline $YMnO_3$ supported on mesoporous carbon type ST3, deposited on a glassy carbon RDE at total mass loading 102 µg cm^{-2}. The electrode was cycled between −1.4 V and 0.5 V in 3 M KOH at 10 mV s^{-1} for 3 cycles.

4.4.5 Nafion™ as binder

The deposited particles adhered well to the glassy carbon surface at all Nafion™ concentrations. A few small particles could be seen falling off when 0.0025wt% Nafion™ in ethanol was used. Figures 4.20 to 4.24 show the voltammograms for 1wt%. 0.05wt% and 0.025wt% Nafion™ in ethanol. The mass loading of $YTi_{0.12}Mn_{0.88}O_{3\pm\delta}$ on the glassy carbon surface was $1\,mg\,cm^{-2}$. The measured current is within the range $-500\,mA\,g^{-1}$ to $200\,mA\,g^{-1}$ for all the Nafion™ concentrations. A small anodic peak can be seen at approximately $-0.75\,V$ for the high, 1wt% Nafion™ concentration.

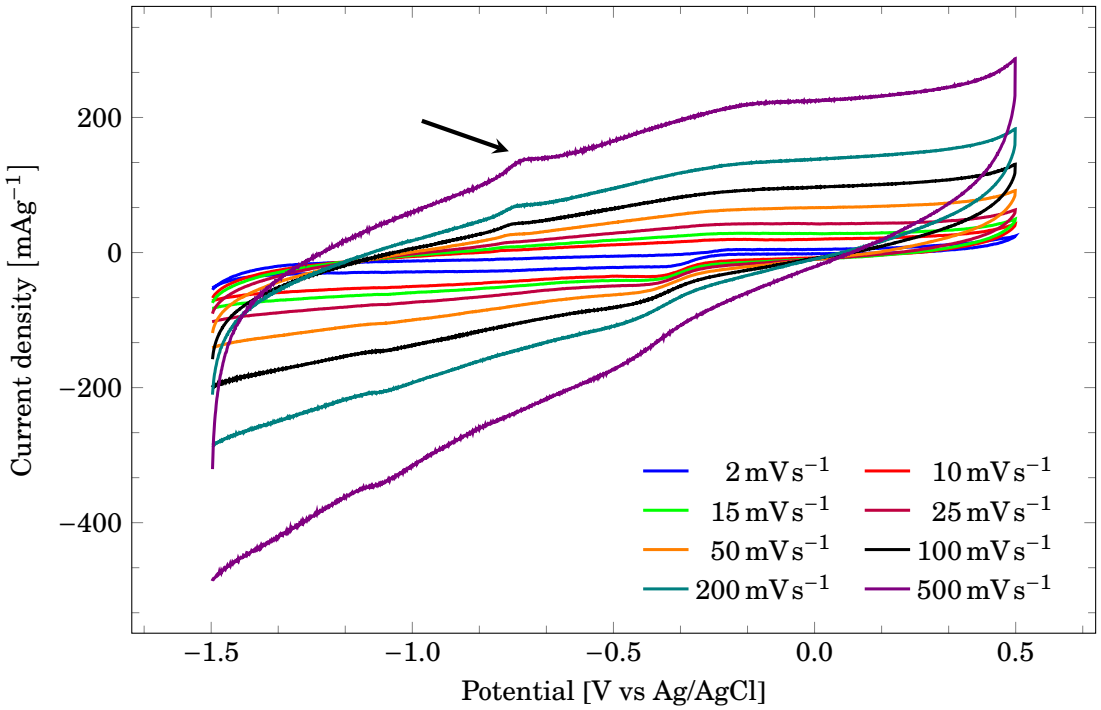

Figure 4.20: Cyclic voltammogram of bulk $YTi_{0.12}Mn_{0.88}O_{3\pm\delta}$ deposited on a glassy carbon RDE, with a mass loading of $1\,mg\,cm^{-2}$. The deposition was made from a suspension of 1wt% Nafion™ in ethanol, with bulk $YTi_{0.12}Mn_{0.88}O_{3\pm\delta}$ suspended at $20\,mg\,mL^{-1}$. 3 M KOH was used as the electrolyte. A small anodic peak can be seen around $-0.75\,mV$.

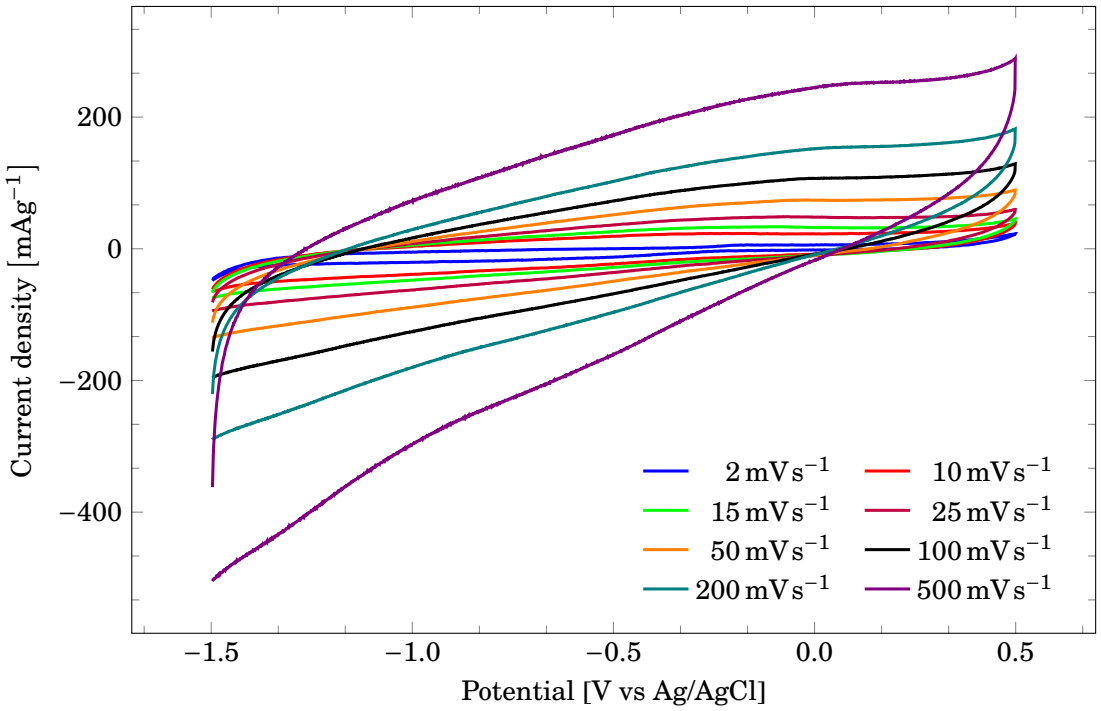

Figure 4.21: Cyclic voltammogram of bulk $YTi_{0.12}Mn_{0.88}O_{3\pm\delta}$ deposited on a glassy carbon RDE, with a mass loading of 1 mg cm^{-2}. The deposition was made from a suspension of 0.05wt% Nafion™ in ethanol, with bulk $YTi_{0.12}Mn_{0.88}O_{3\pm\delta}$ suspended at 20 mg mL^{-1}. N_2(g) purged 3 M KOH was used as the electrolyte.

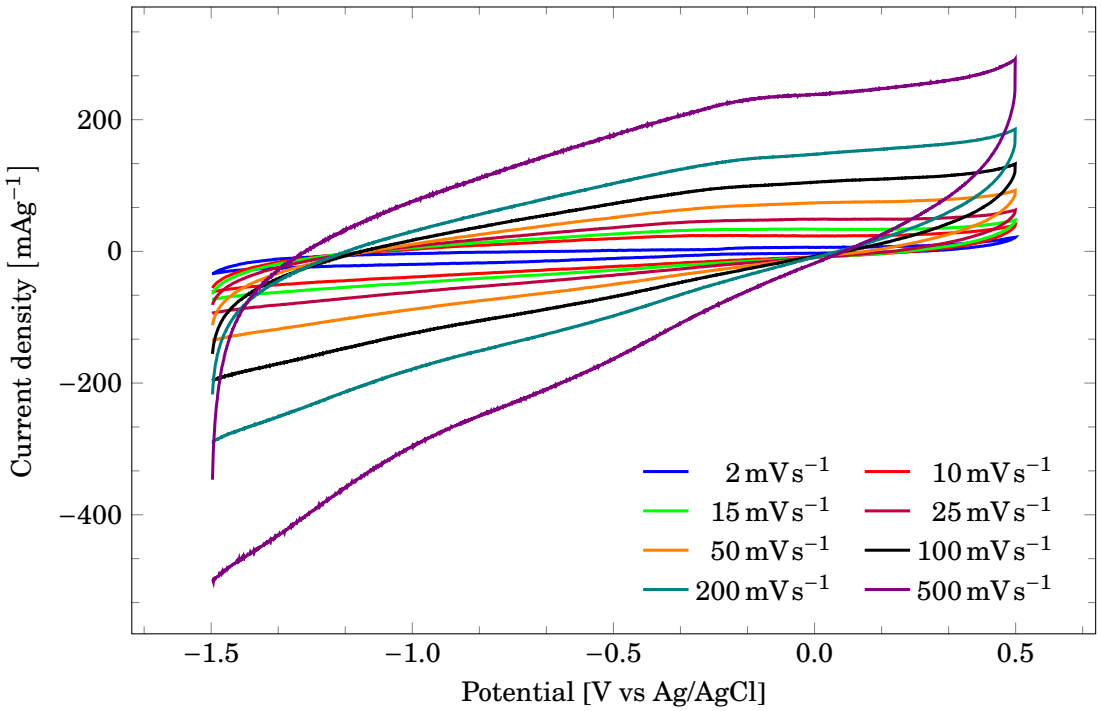

Figure 4.22: Cyclic voltammogram of bulk $YTi_{0.12}Mn_{0.88}O_{3\pm\delta}$ deposited on a glassy carbon RDE, with a mass loading of 1 mg cm^{-2}. The deposition was made from a suspension of 0.025wt% Nafion™ in ethanol, with bulk $YTi_{0.12}Mn_{0.88}O_{3\pm\delta}$ suspended at 20 mg mL^{-1}. 3 M KOH was used as the electrolyte, both oxygen saturated and N_2(g) purged.

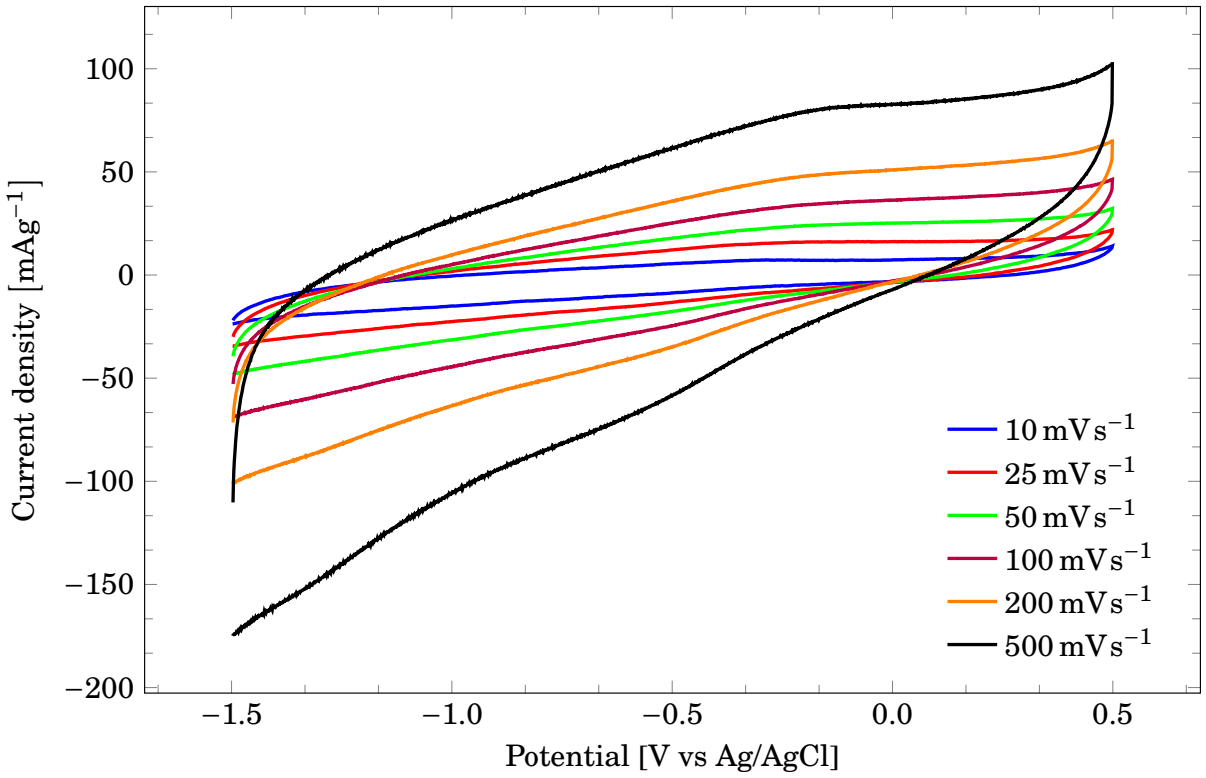

Figure 4.23: Cyclic voltammogram of bulk $YTi_{0.12}Mn_{0.88}O_{3\pm\delta}$ deposited on a glassy carbon RDE, with a mass loading of 2.5 mg cm^{-2}. The deposition was made from a suspension of 0.1wt% Nafion™ in ethanol, with bulk $YTi_{0.12}Mn_{0.88}O_{3\pm\delta}$ suspended at 50 mg mL^{-1}. 3 M KOH was used as the electrolyte, both oxygen saturated and N_2(g) purged.

The last suspension used in combination with Nafion™ was nanoparticles of $YMnO_3$ loaded on mesoporous carbon ST3. In order to compare the current response with and without Nafion™ present, the same suspension load as earlier, $1\,mg\,mL^{-1}$, was used in combination with 0.025wt% Nafion™ The voltammogram produced from cycling the GCRDE electrode in N_2(g) purged 3 M KOH is shown in Figure 4.24

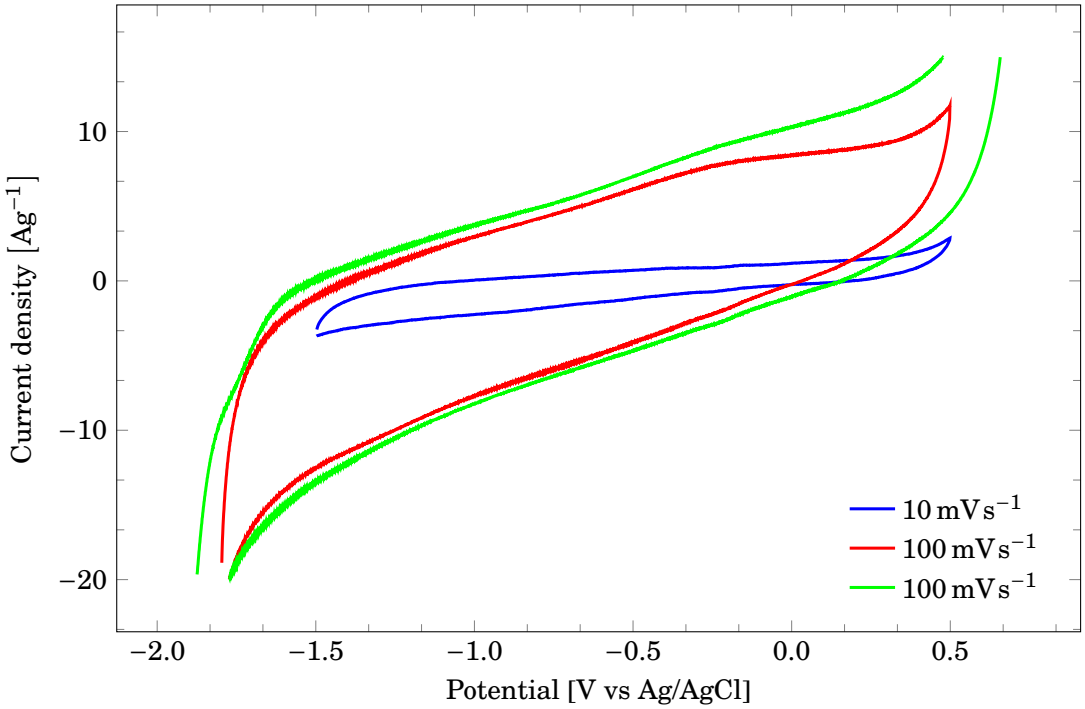

Figure 4.24: Cyclic voltammogram of nanocrystalline $YMnO_3$ deposited on a glassy carbon RDE from an ethanol suspension containing 0.025wt% Nafion™.

The first scan at $10\,mV\,s^{-1}$ produced an anodic peak during the first cycle that was not present in the subsequent cycles and sweep rates. A wide cathodic peak might be present, as seen in Figure 4.25.

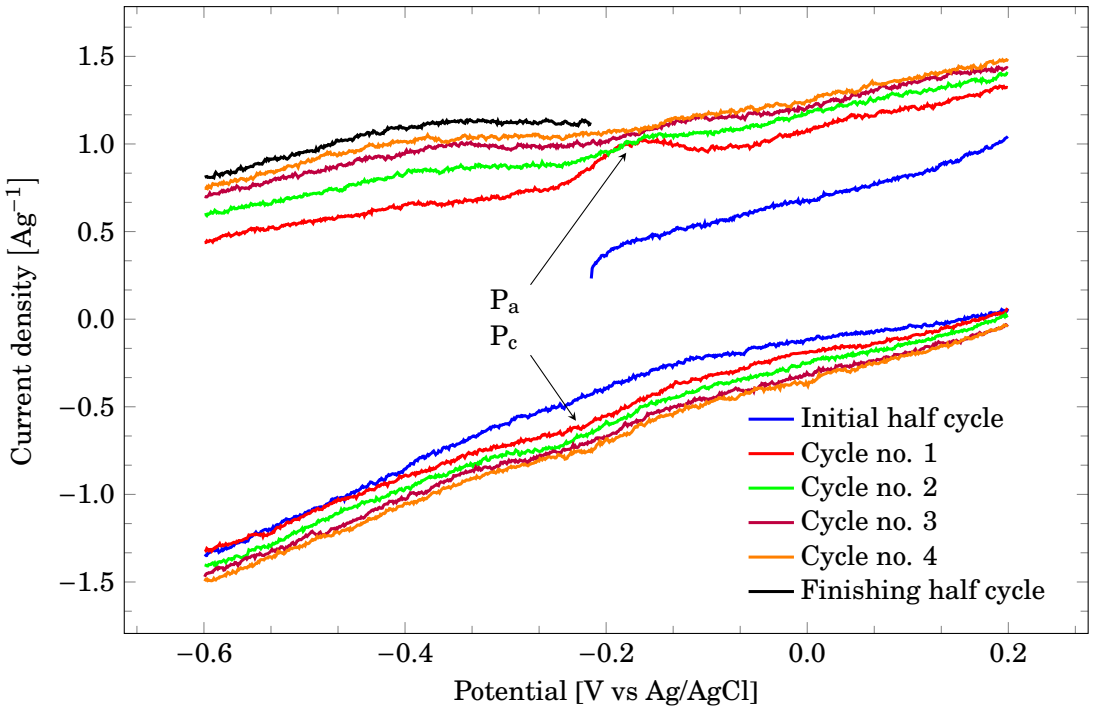

Figure 4.25: Cyclic voltammogram of nanocrystalline $YMnO_3$ loaded onto mesoporous carbon ST3 at 30t%, and suspended at $10\,mg\,mL^{-1}$ in ethanol containing 0.0025wt% Nafion™. The 30wt% $YMnO_3$ was deposited onto a glassy carbon RDE at a total mass loading of $51\,\mu g\,cm^{-2}$ and cycled at $10\,mV\,s^{-1}$ in N_2(g) purged 3 M KOH. A pair of anodic-cathodic peaks can be seen in the first cycle, but they are not present in subsequent cycles.

.

4.5 Glassy carbon rod

When filling the cell with KOH, and during purging, particles were easily washed away from the electrode. In Figure 4.26, the washed-away particles can be clearly seen to the right in the picture. Even though the deposited particles did not adhere well to the GC surface, careful filling and purging of the cell allowed cyclic voltammograms to be obtained.

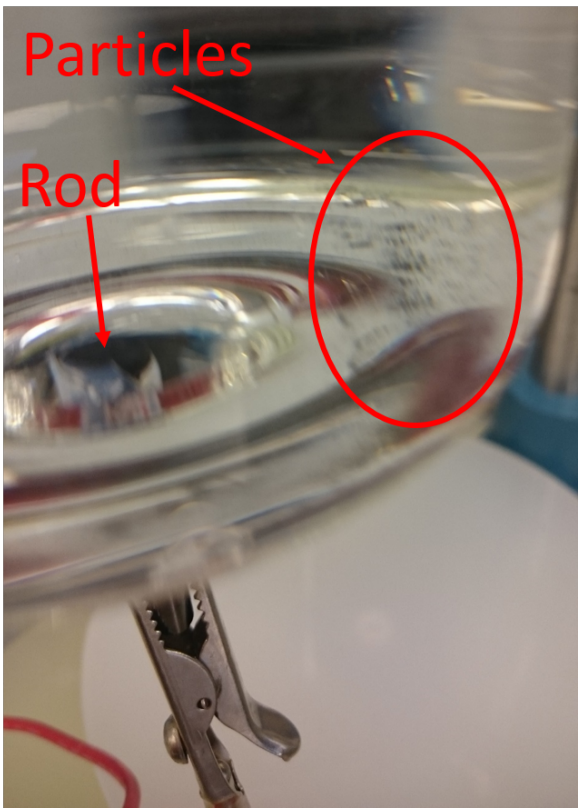

Figure 4.26: The material that was swept away from the electrode surface during filling and purging of the cell can be seen as black particles to the right

4.5.1 Bulk $YTi_{0.12}Mn_{0.88}O_3$

Both depositions of bulk $YTi_{0.12}Mn_{0.88}O_{3\pm\delta}$ on the glassy carbon rod had quite rectangular shaped CV curves when cycled between $-0.8\,V$ and $0.5\,V$ and various sweep rates. The nearly identical curves are shown in Figure 4.27.

When the potential range was increased and the second deposition of bulk $YTi_{0.12}Mn_{0.88}O_{3\pm\delta}$ on the GC rod was cycled between $-1.5\,V$ and $0.2\,V$, an anodic peak emerged in Figure 4.28.

Reducing the cathodic turnaround potential and performing cycles between $-1.2\,V$ and $0.2\,V$ resulted in the curves in Figure 4.29.

By looking at only the low sweep rates used in Figures 4.27 to 4.29, it is possible to identify an anodic peak around $-0.5\,V$. They have been replotted in Figures 4.30 and 4.31. The peak potential appear to be dependent on the cathodic turnaround potential.

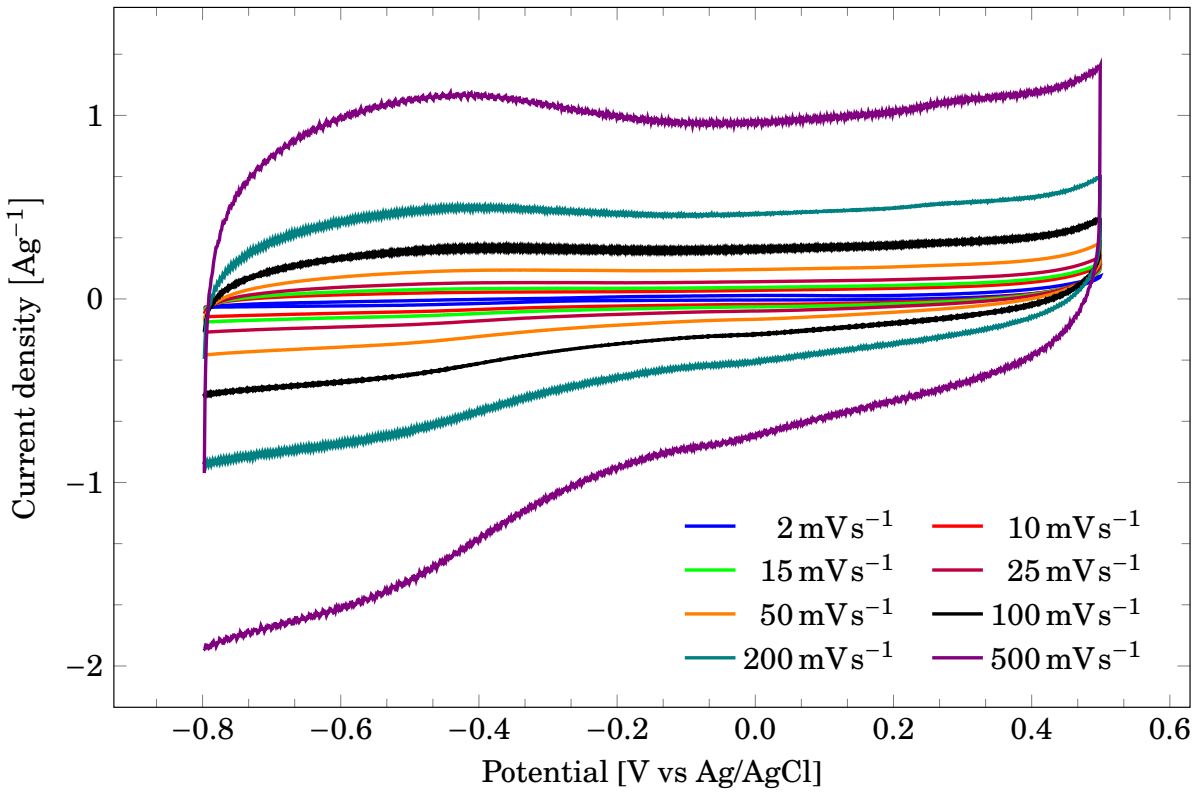

(a) First deposition

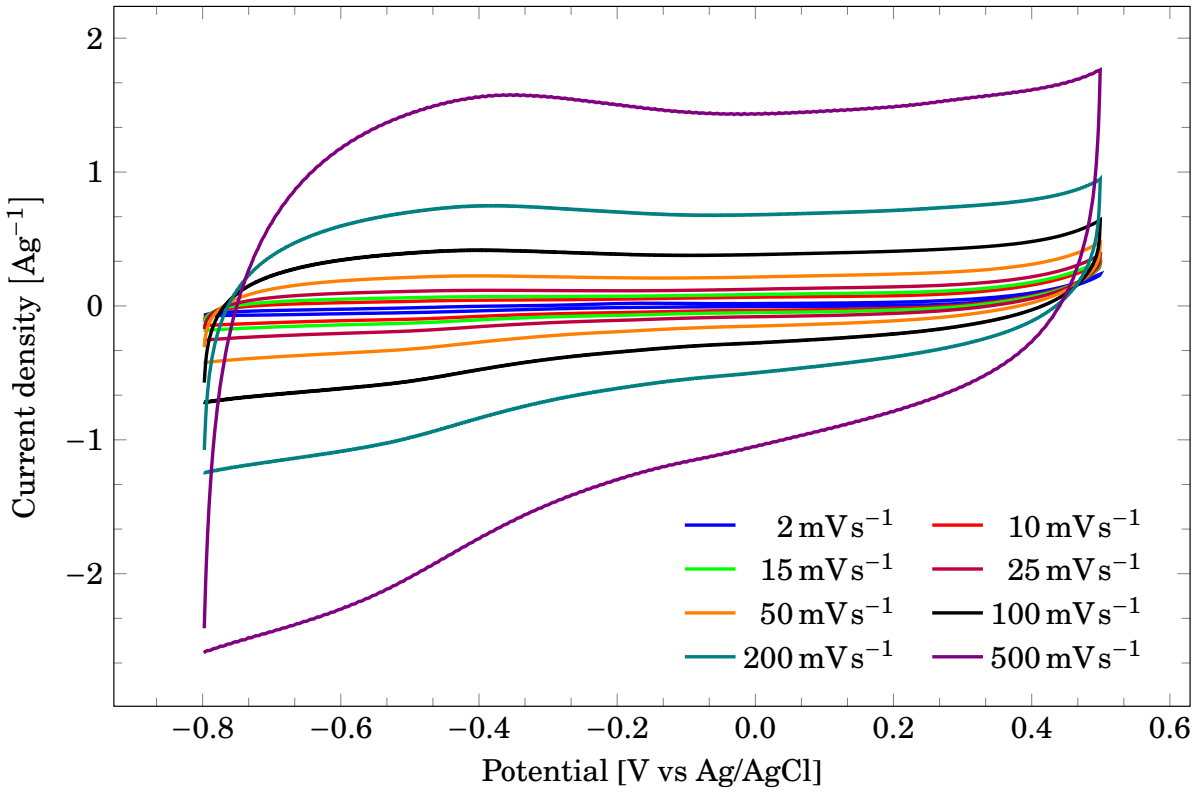

(b) Second deposition

Figure 4.27: Cyclic voltammograms of the first (fig. 4.27a) and second (fig. 4.27b) deposition of bulk $YTi_{0.12}Mn_{0.88}O_{3\pm\delta}$ on the glassy carbon rod. The cycling was performed in N_2(g) purged 3 M KOH.

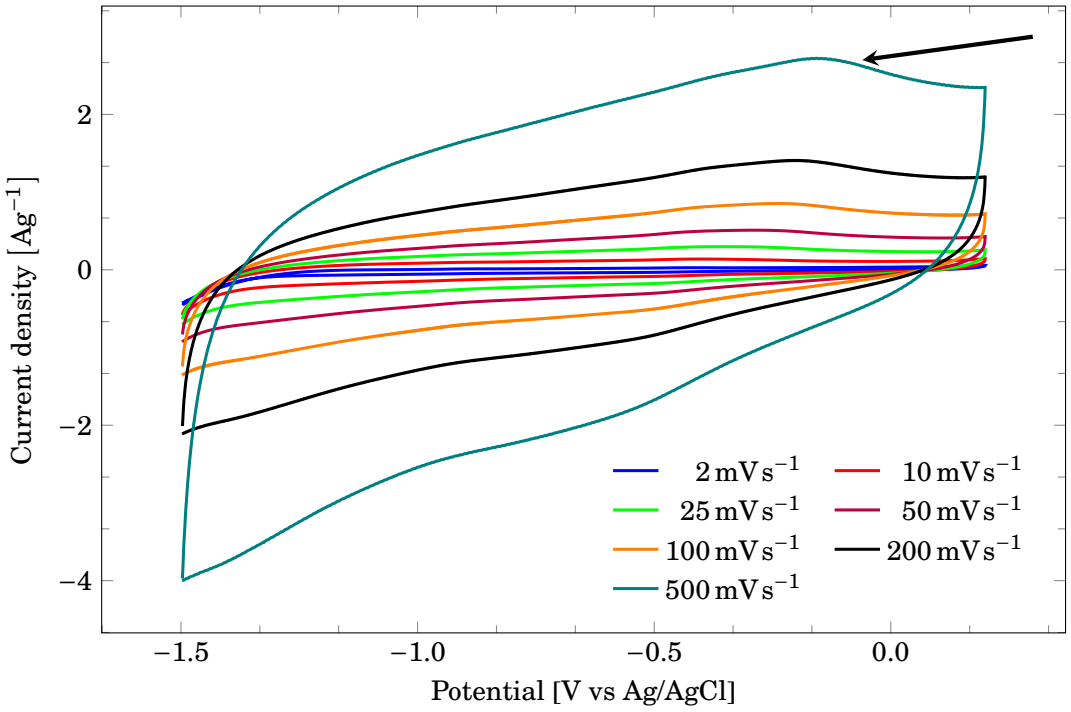

Figure 4.28: Cyclic voltammogram of bulk $YTi_{0.12}Mn_{0.88}O_3$ deposited on glassy carbon. The electrolyte was N_2(g) purged 3 M KOH

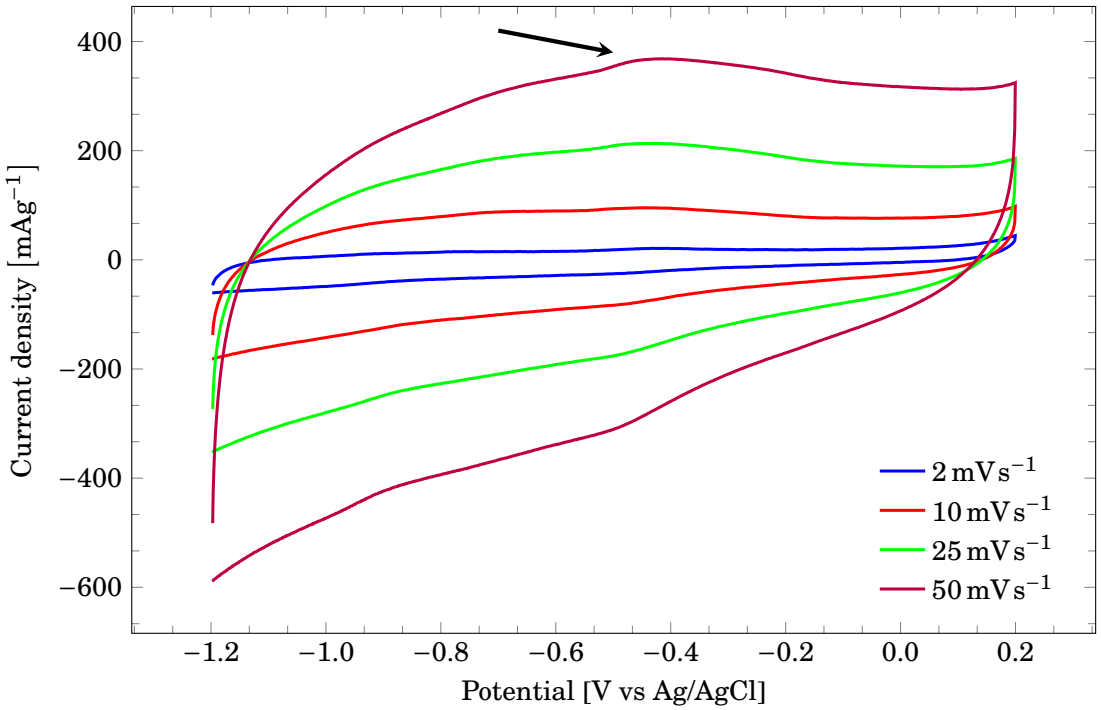

Figure 4.29: Cyclic voltammogram of bulk $YTi_{0.12}Mn_{0.88}O_{3\pm\delta}$ deposited on a glassy carbon rod. Performed on the same electrode as Figure 4.28, but with a cathodic turnaround potential at −1.2 V, and only at low sweep rates.

.

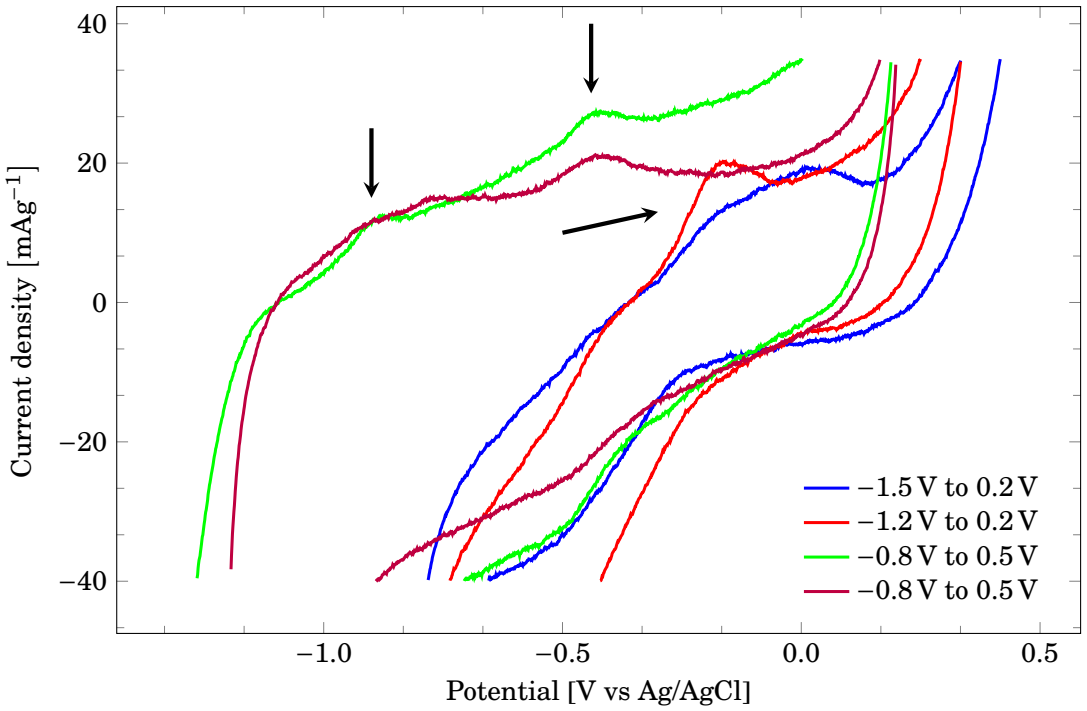

Figure 4.30: The sweeps at $2\,\mathrm{mV\,s^{-1}}$ from Figures 4.27 to 4.29. An anodic peak is present at all the sweeps. The peak potential appear be dependent on the cathodic turnaround potential.

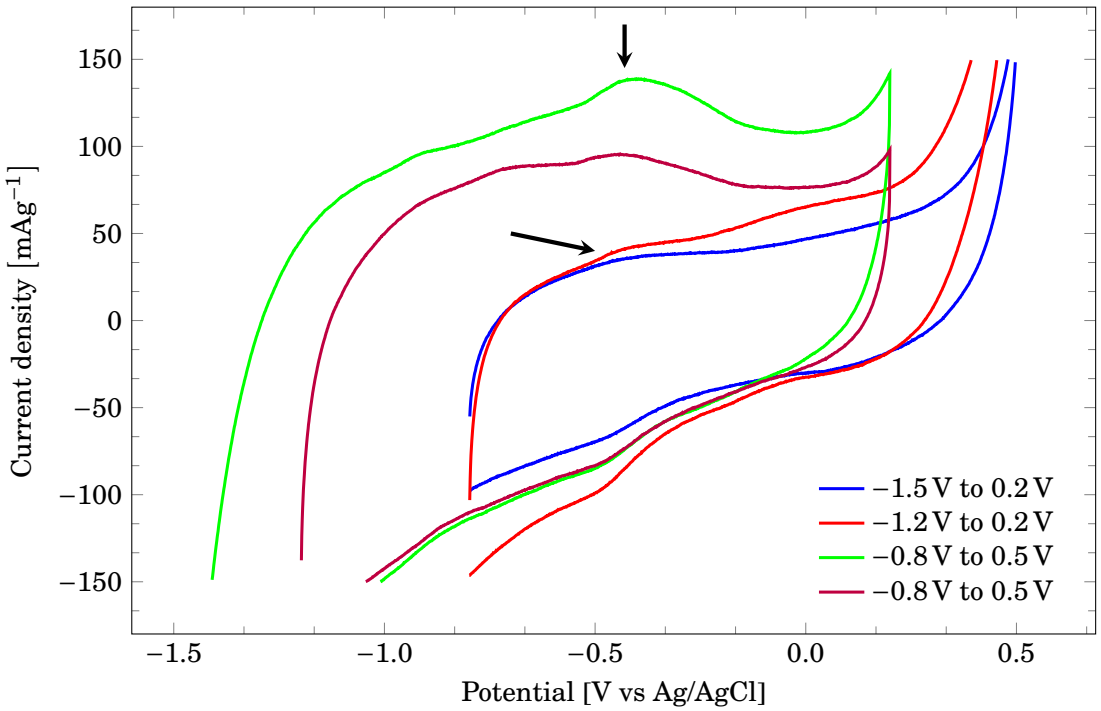

Figure 4.31: The sweeps at $10\,\mathrm{mV\,s^{-1}}$ from Figures 4.27 to 4.29. An anodic peak is present around $-0.45\,\mathrm{V}$ for the low cathodic turnaround potentials.

4.5.2 Nanocrystalline $YTi_{0.15}Mn_{0.85}O_{3\pm\delta}$

The cyclic voltammogram for nanocrystalline $YTi_{0.15}Mn_{0.85}O_{3\pm\delta}$ deposited on the glassy carbon rod is shown in Figure 4.32. The electrolyte was N_2(g) purged 3 M KOH. The curves are nearly identical to the voltammogram of only the GC rod (fig. D.12).

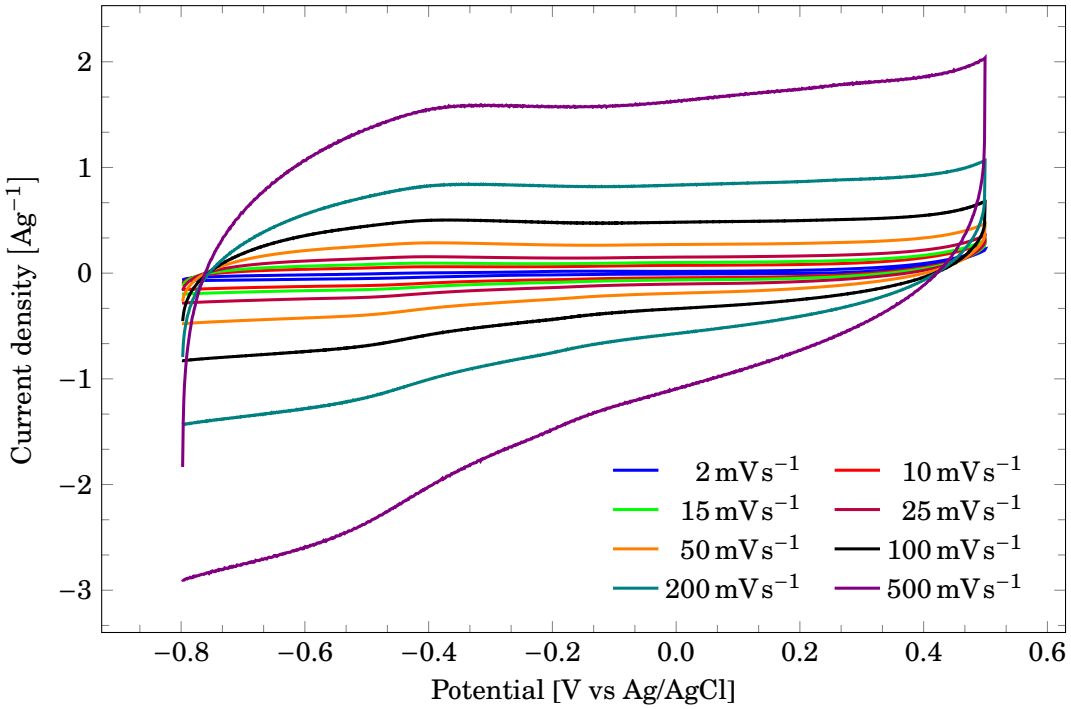

Figure 4.32: Cyclic voltammogram of nanoparticles of $YTi_{0.15}Mn_{0.85}O_{3\pm\delta}$ deposited on the glassy carbon rod. The cycles were performed in N_2(g) purged 3 M KOH. The shape of the CV curve was nearly identical to that of the GC rod itself.

4.5.3 Nanocrystalline $YMnO_3$ supported on mesoporous carbon ST8

The current response of nanocrystalline $YMnO_3$ supported on mesoporous carbon ST8 deposited on the glassy carbon rod, was different than that of the corresponding experiment on the RDE electrode (section 4.4.3). The voltammogram are shown in Figure 4.33.

By studying the cycles performed in a slightly varying potential range at 100 mV s^{-1}, a cathodic and anodic peak can be observed in Figure 4.34 with $E_{1/2}$ around −0.4 V.

When the concentration of KOH was lowered to 1 M and an identical characterization of an identical electrode was performed, the results were quite similar, as seen in Figure 4.35. In the magnified area, a distinct peak was present around $E = -0.35$ V for a sweep rate of 100 mV s^{-1}. This was the first scan performed. The peak gradually reduced in magnitude during the subsequent scans, until the curve had the shape that can be seen for 200 mV s^{-1} and 500 mV s^{-1}. A larger version of the magnified area can be seen in Figure D.18

The cyclic voltammogram of mesoporous carbon deposited onto the GC rod at 51 µg cm^{-2} in N_2(g) purged 3 M KOH is shown in Figure 4.36. There is an absence of redox peaks around −0.45 V.

The rubber seal ruptured when the cell was dismantled in order to measure the current from mesoporous carbon in 1 M KOH, and a new seal could not be acquired in time to perform the measurements.

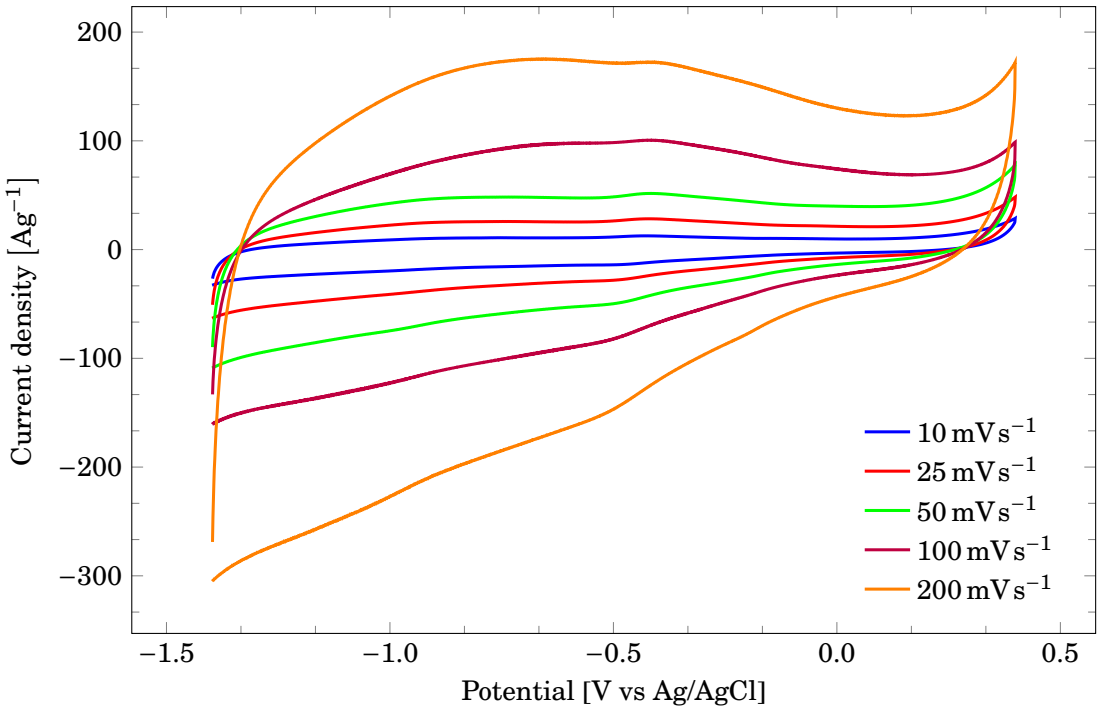

Figure 4.33: Cyclic voltammogram of nanoparticles of $YMnO_3$ supported at 30wt% on mesoporous carbon ST8, deposited on a glassy carbon rod at total mass loading 51 µg cm^{-2}. N_2(g) purged 3 M KOH was used as the electrolyte.

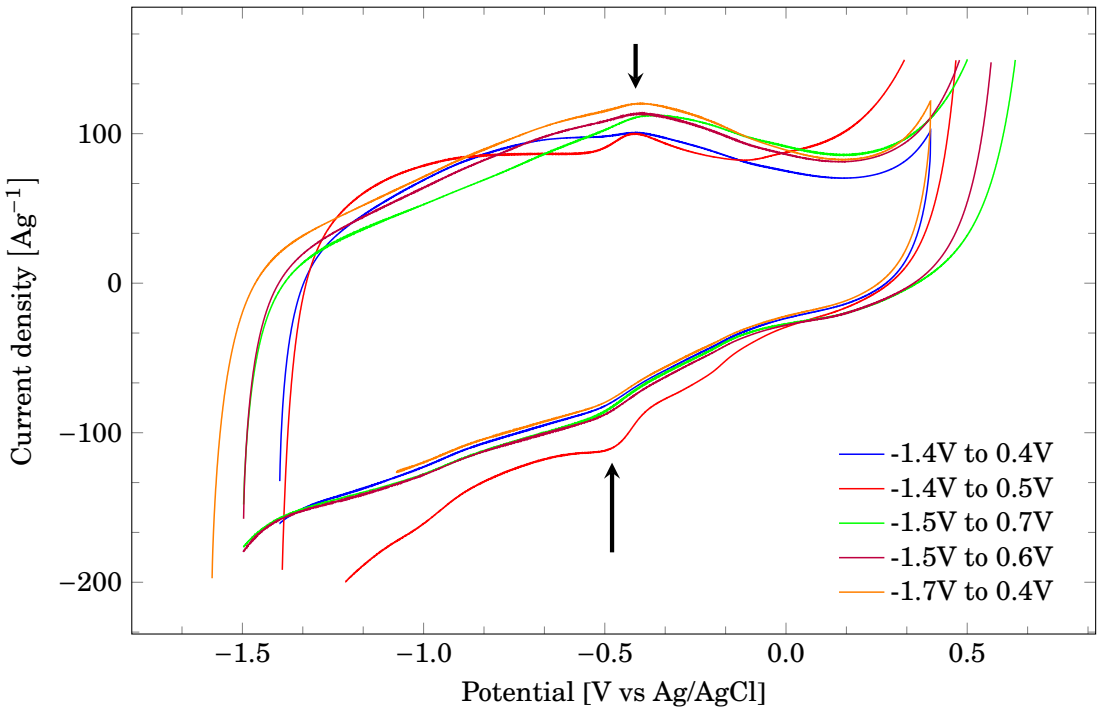

Figure 4.34: Cyclic voltammograms of nanoparticles of $YMnO_3$ supported on mesoporous carbon, deposited on a glassy carbon rod with a total mass loading of 51 µg cm^{-2}. The measurements were performed in N_2(g) purged 3 M KOH at a sweep rate of 100 mV s^{-1}. An anodic peaks is present in all the curves with $E_{1/2}$ around −0.4 V.

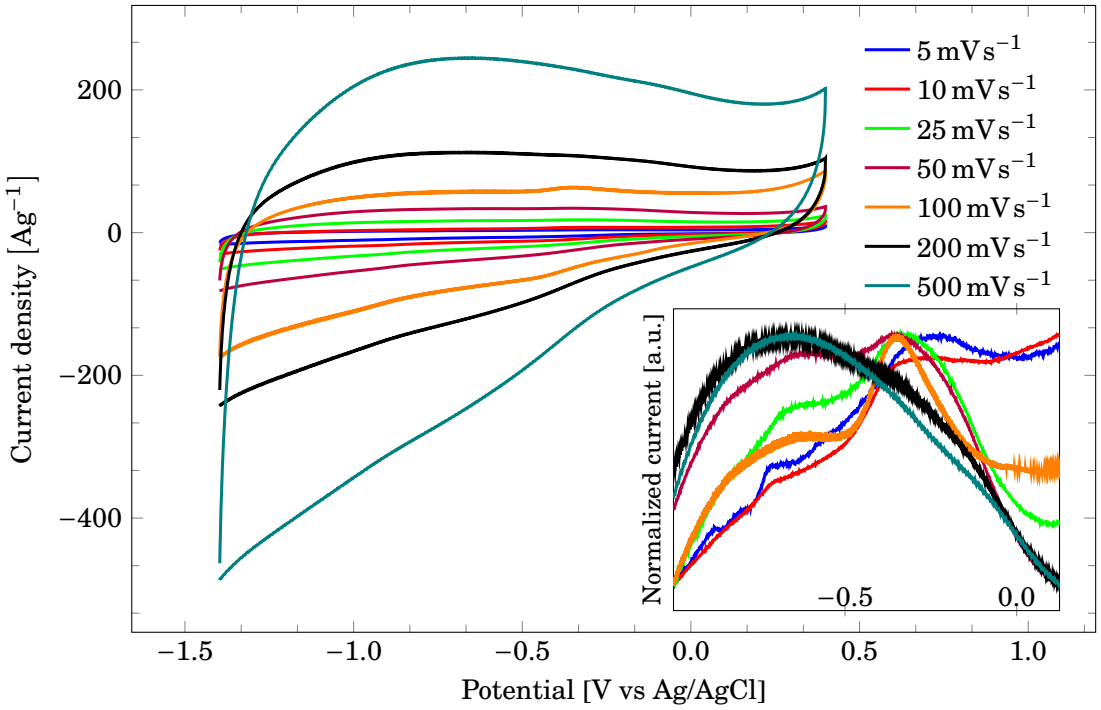

Figure 4.35: Cyclic voltammogram of nanoparticles of $YMnO_3$ supported at 30wt% on mesoporous carbon ST8, deposited on a glassy carbon rod at a total mass loading of 51 µg cm^{-2}. N_2(g) purged 1 M KOH was used as the electrolyte. A clear oxidation peak can be discerned at 100 mV s^{-1} around −0.35 V. The shape of the peak changed during cycling.

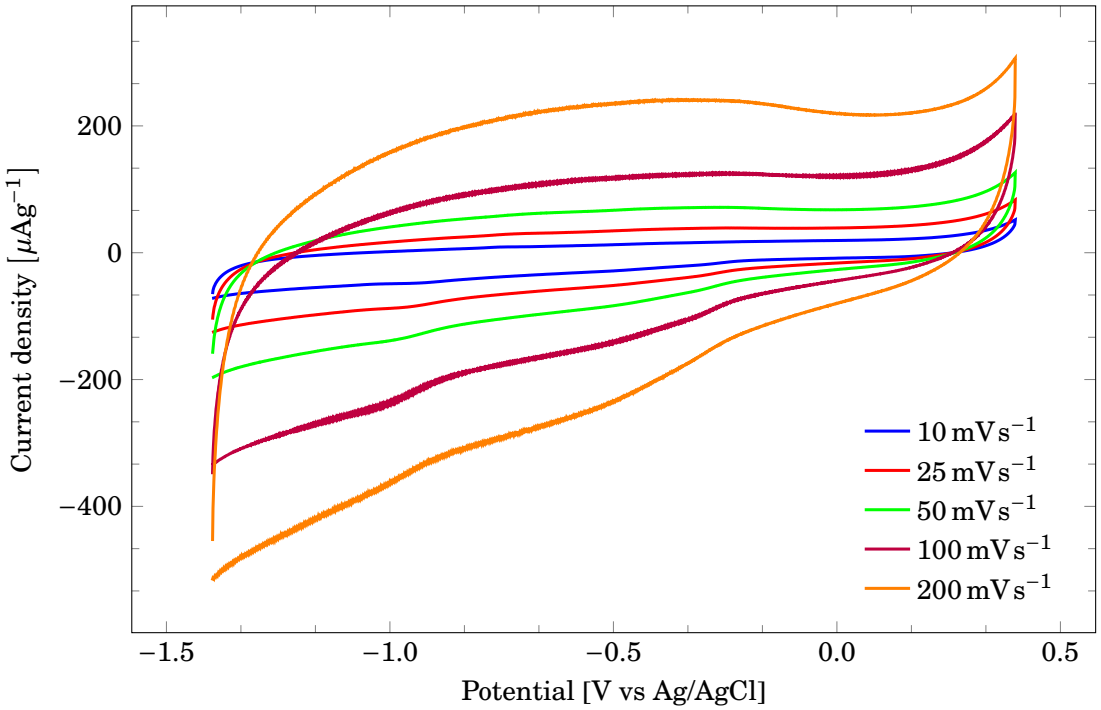

Figure 4.36: Cyclic voltammogram of mesoporous carbon ST8 on the GC rod, in N_2(g) purged 3M KOH at various sweep rates. There is an absence of redox peaks around −0.4 V.

4.6 Flat specimen electrode

The volume, weight, calculated and theoretical density, and porosity of the sintered discs are given in Table 4.6. Only 2 out of 7 discs did not break during polishing. The total porosity was expressed as $P = 1 - \frac{\rho}{\rho_{\text{cry}}}$ where ρ is the density found from measuring weight and volume of the disc, and ρ_{cry} was the crystal density found in the Rietveld refinement of the XRD-data in Figure 4.3.

Table 4.6: The total porosities of the sintered samples. The crystal density used was ρ_{cry} =5.084 g cm^{-3}. It was found by refining the XRD-data for the bulk particles with TOPAS[45].

Disc no.	Diameter mm	Height mm	Volume cm^3	Weight g	Density g cm^{-3}	Porosity %
1	18.2	1.2	0.312	1.050	3.363	33.9
2	18.2	2.3	0.598	1.902	3.179	37.5

During polishing which was performed by hand, most of the discs fractured, as shown in Figure 4.37b. Two discs from the first batch , i.e. sintered for 12 hours at 1450 °C from binary oxides, survived the polishing. However, they both fractured when electrode was tightened, shown in Figure 4.37a. It was attempted to perform cyclic voltammetry on the first disc, as the crack appeared quite narrow. The second batch of discs, sintered for 10 hours at 1400 °C fractured very easily during polishing.

(a) When tightening the teflon casket on the flat specimen electrode, the pressure on the disc caused it to fracture.

(b) 5 out of 7 sintered discs of bulk $YTi_{0.12}Mn_{0.88}O_{3\pm\delta}$ fractured during polishing

Figure 4.37: The sintered discs of bulk $YTi_{0.12}Mn_{0.88}O_{3\pm\delta}$ was not sufficiently mechanically strong, and would fracture either during polishing or when assembling the flat specimen electrode

The first voltammogram recorded at 100 mV s^{-1} is shown in Figure 4.38a. The cathodic current increased fast when the potential went below −0.5 V. If the potential range is restricted to show

only the part of the curve between approximately $\pm 0.4\,\mathrm{V}$, a possible oxidation plateau, starting at P_a, and a cathodic peak can be seen between $-0.2\,\mathrm{V}$ and $0\,\mathrm{V}$ in Figure 4.38b.

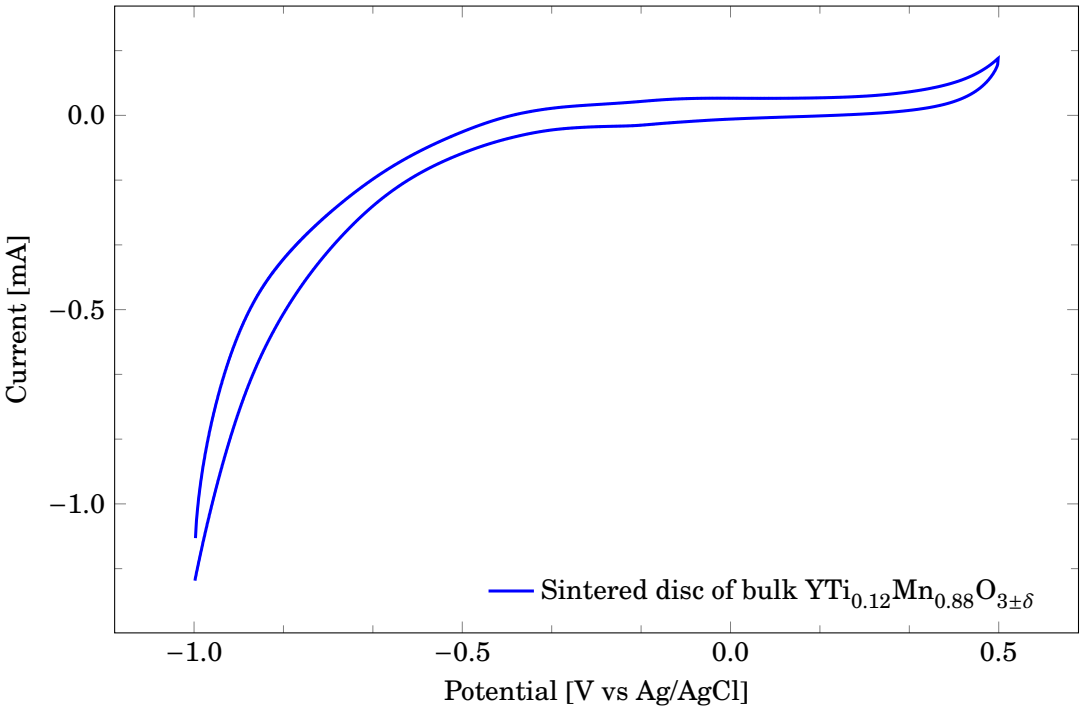

(a)

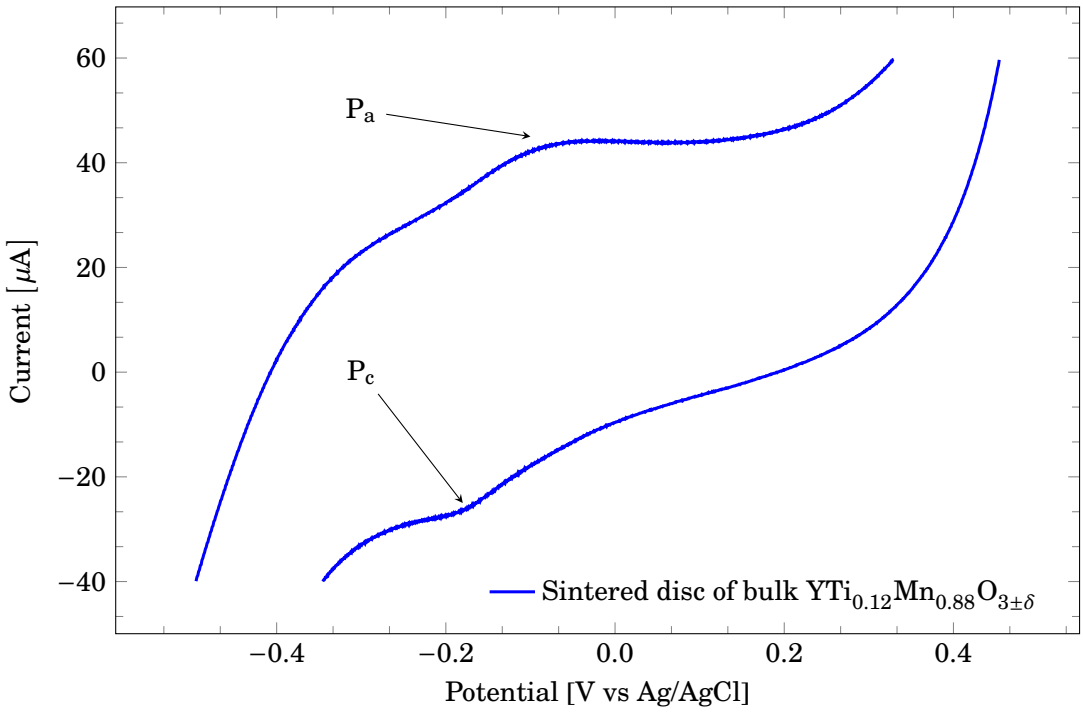

(b)

Figure 4.38: Cyclic voltammogram of a sintered disc of bulk $YTi_{0.12}Mn_{0.88}O_{3\pm\delta}$ inserted into a flat specimen electrode (**a**). In (**b**), the range on the axes has been reduced. The cycle was performed at $100\,mV\,s^{-1}$ in 3 M KOH. The disc had fractured, but this voltammogram was successfully recorded before the electrolyte penetrated through the crack. An oxidation plateau may be present at P_a, with a corresponding return peak at P_c. Sweep rate was $100\,mV\,s^{-1}$ in 3 M KOH.

4.7 SEM and EDS

4.7.1 Particle size of bulk $YTi_{0.12}Mn_{0.88}O_{3\pm\delta}$

As seen in Figure 4.39, all the particles were below 37 µm, as would be expected since they had been sieved in a 37 micron sieve. It would appear that the particle morphology are spherical-oval.

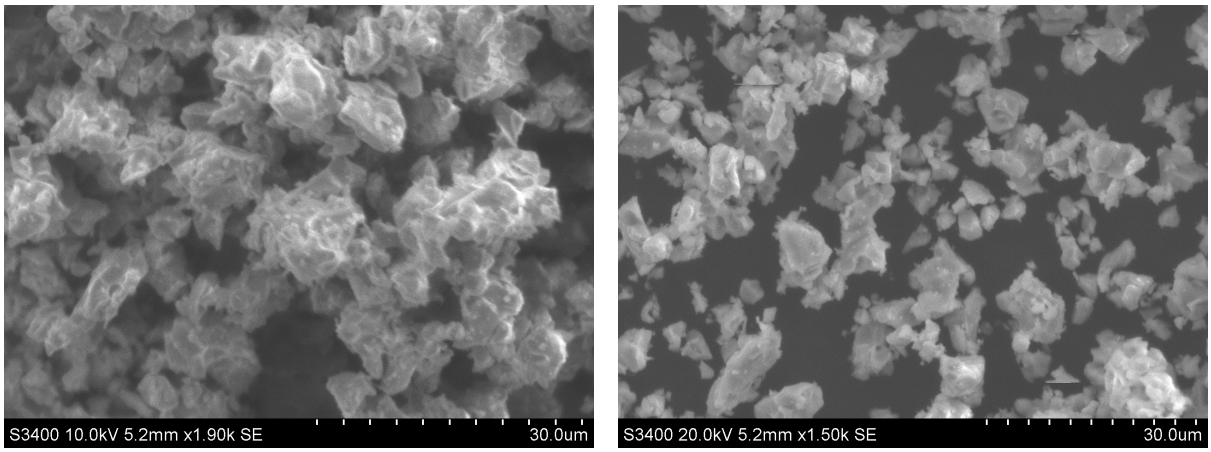

(a) **(b)**

Figure 4.39: SEM image of the bulk $YTi_{0.12}Mn_{0.88}O_{3\pm\delta}$

4.7.2 Sintered disc of $YTi_{0.12}Mn_{0.88}O_{3\pm\delta}$

Even though the porosity of the sintered samples was 30-40%, the sintered sample appear to be quite dense at the surface. No large-continuous pores are present in Figure 4.40

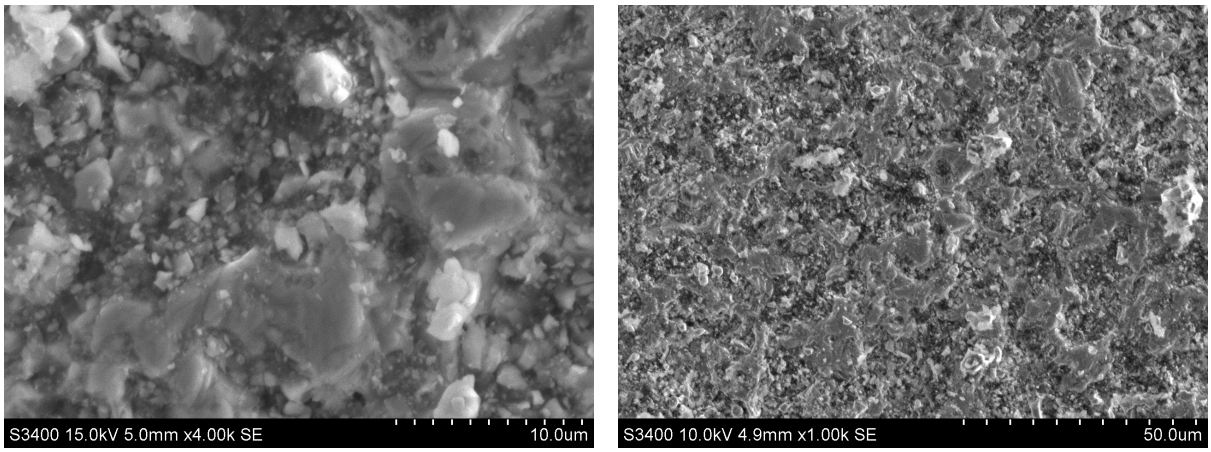

(a) **(b)**

Figure 4.40: SEM image of the polished surface of a sintered sample of bulk $YTi_{0.12}Mn_{0.88}O_{3\pm\delta}$

4.7.3 Deposited bulk $YTi_{0.12}Mn_{0.88}O_{3\pm\delta}$

Figure 4.41 show SEM images of bulk $YTi_{0.12}Mn_{0.88}O_{3\pm\delta}$ deposited on the glassy carbon RDE. The GC rod had the same diameter as the RDE, so the images should be representative for both cases. The particles were deposited with a mass loading of $1\,mg\,cm^{-2}$. The film appear to be thick, as the glassy carbon can not be seen though any pores.

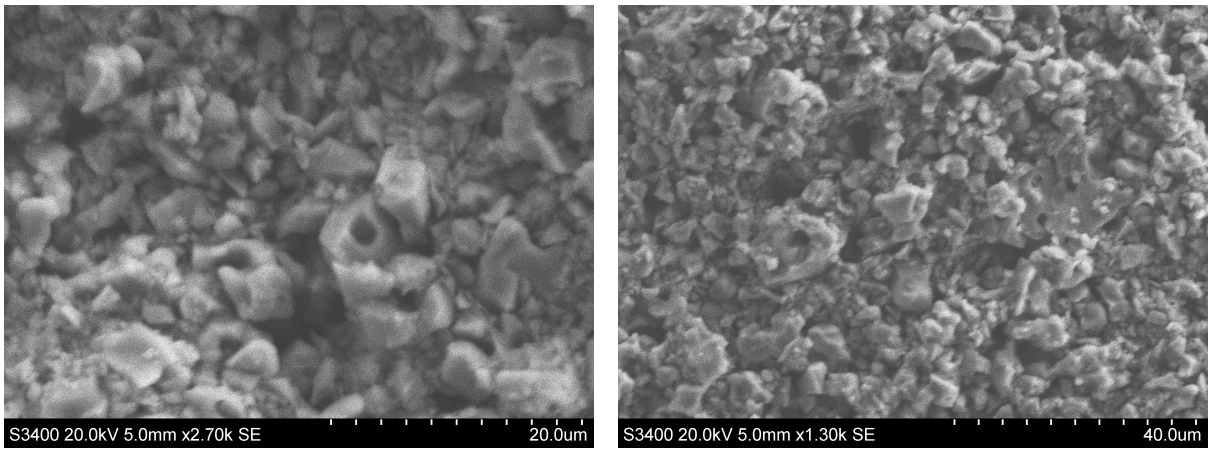

(a) **(b)**

Figure 4.41: SEM image of the RDE electrode with bulk $YTi_{0.12}Mn_{0.88}O_{3\pm\delta}$ deposited at $1\,mg\,cm^{-2}$.

4.7.4 Nanocrystalline $YMnO_3$

As seen in Figure 4.42a, $YMnO_3$ appears to be agglomerated or polycrystalline with agglomerate- or particle sizes up to 200 nm. From the EDS spectra of area 1-3 in Figure 4.43 given in Figures 4.44 to 4.46 it was confirmed that the bright particles are $YMnO_3$. The brightness is due to charging, as the conductivity of $YMnO_3$ is lower than that of mesoporous carbon. The Y and Si peaks overlap because they lie close in K_α-energy. At ≈3.4 keV, there is a false Sn-peak due to K_α^{Sn} being double that of the substrate, Si[48]. The presence of a manganese peak in area 1, and the lack thereof in area 2 and 3 confirmed that the bright particles are $YMnO_3$.

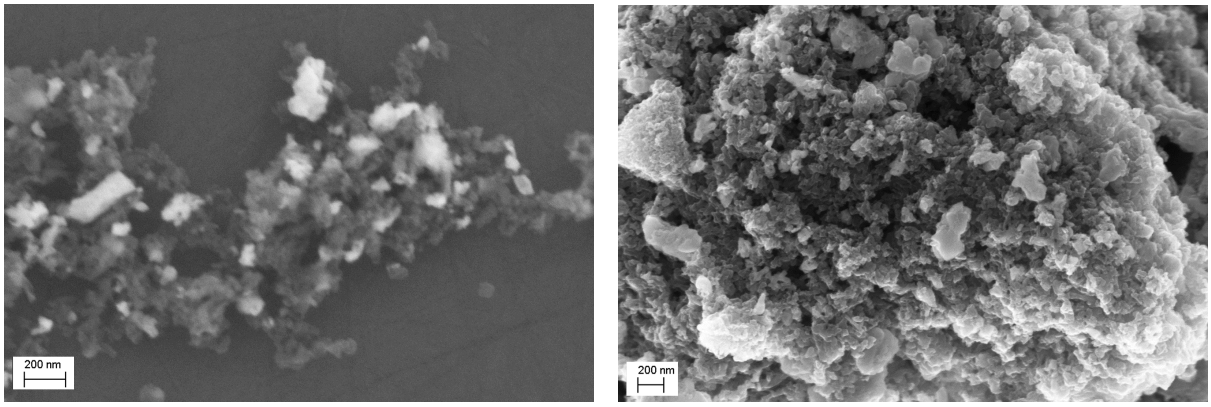

(a) **(b)**

Figure 4.42: Secondary electron SEM images of nanocrystalline $YMnO_3$ supported on mesoporous carbon ST8. $YMnO_3$ are white due to charging (**a**). The porosity of the carbon can be seen in the InLens-detector image (**b**).

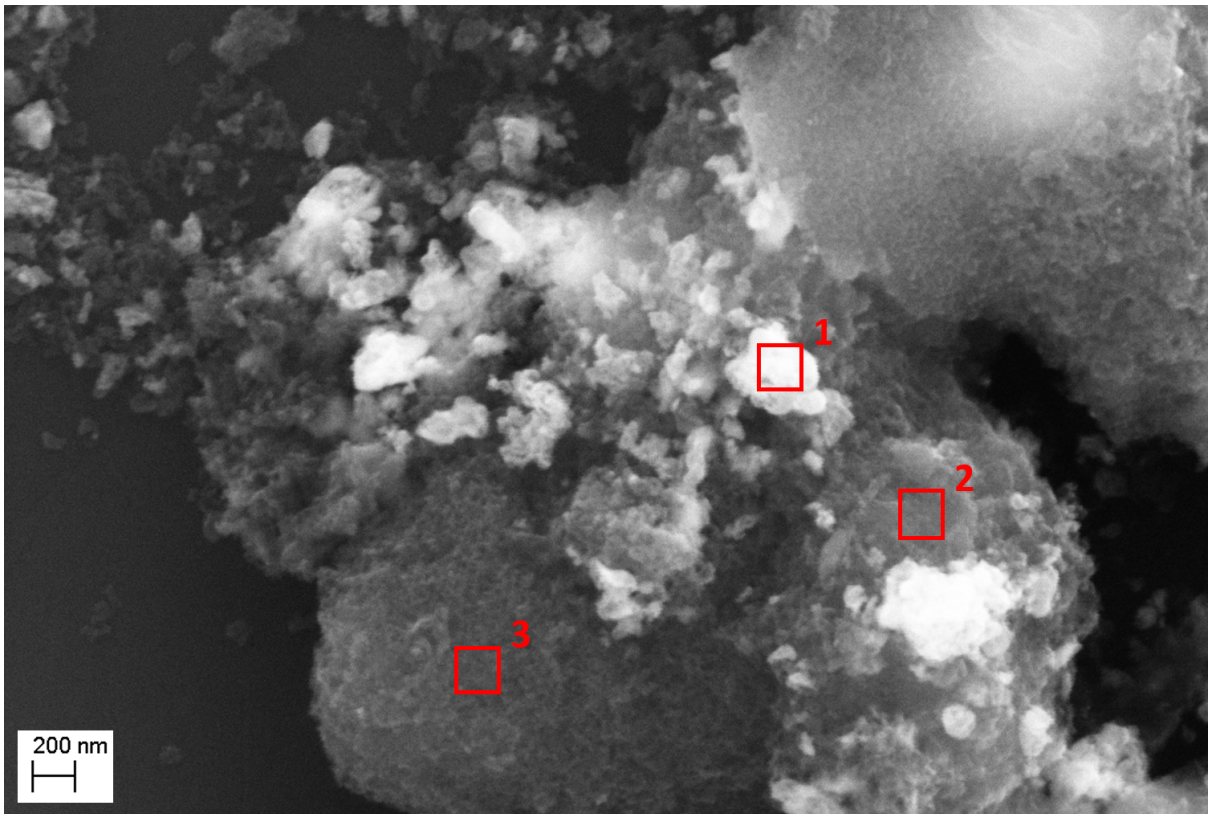

Figure 4.43: Secondary electron image of nanocrystalline $YMnO_3$ supported on mesoporous carbon type ST8. The areas 1-3 was analysed by EDS.

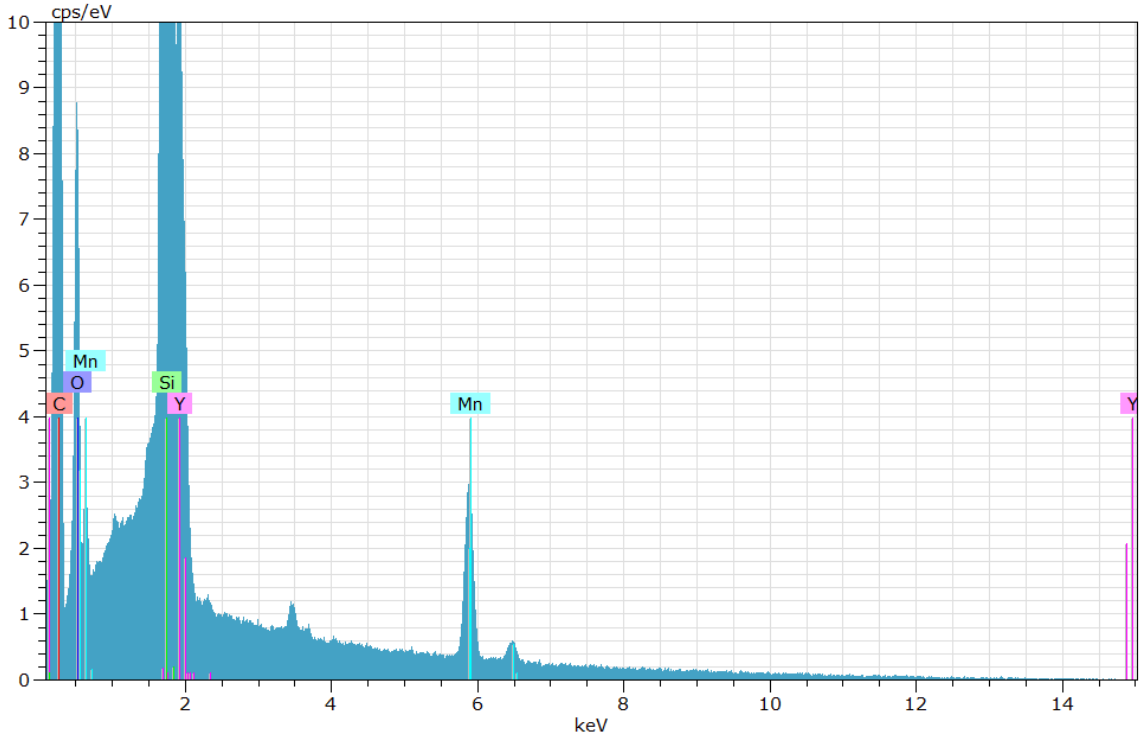

Figure 4.44: EDS spectra of area 1. The clear presence of manganese confirms that the bright particles are $YMnO_3$. The peaks for the Si-substrate and Y overlaps, as seen by the asymmetrical peak.

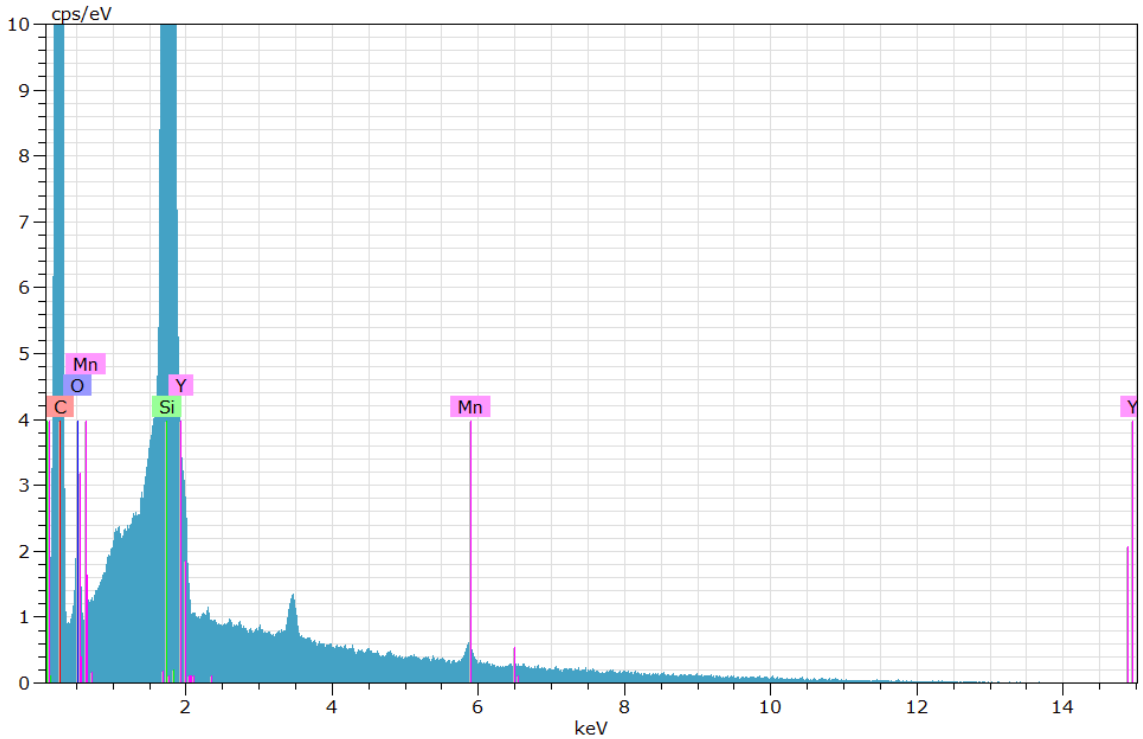

Figure 4.45: EDS spectra of area 2. The image is of mesoporous carbon, although some manganese are present.

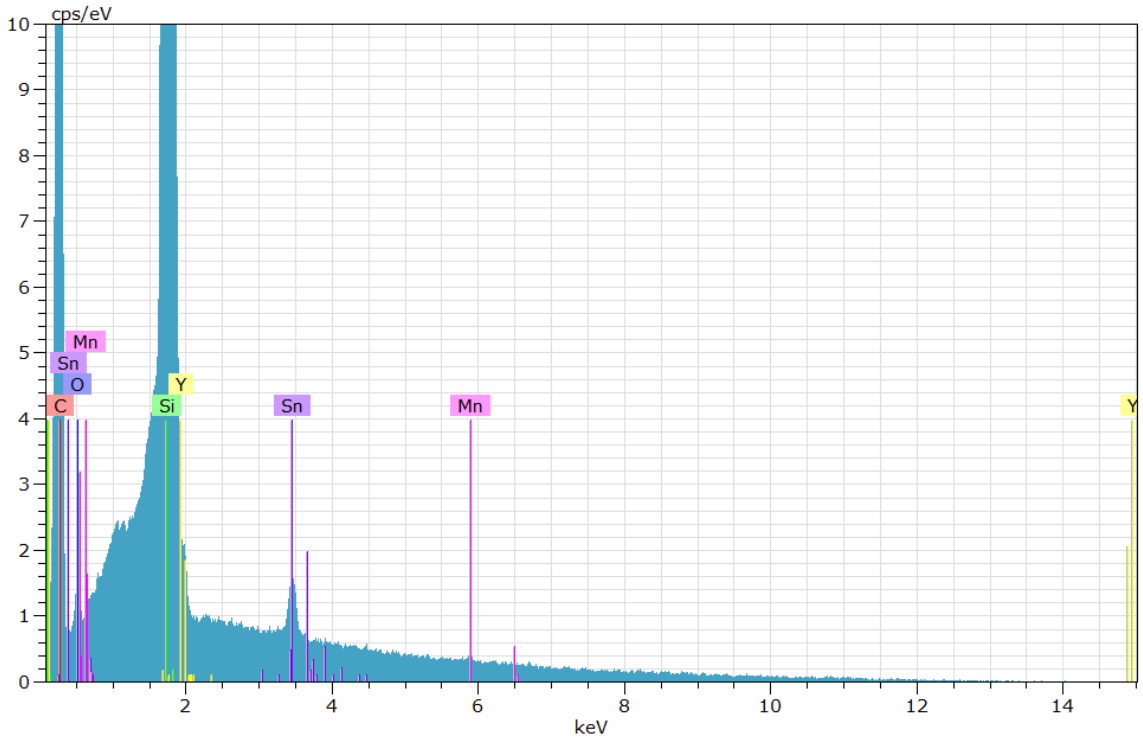

Figure 4.46: EDS spectra of area 3. No manganese was detected. The Sn-peak is due to Sn K_α energy being half of that of Si.

4.8 Analysis of cyclic voltammograms

Due to the promising CV curves recorded for nanocrystalline $YMnO_3$ supported on mesoporous carbon ST8, the separated faradic and non-faradic currents will be presented in the following sections. The separated currents for the other thin-film compositions are presented in Appendix D.

4.8.1 RDE

Even though the current contribution from mesoporous carbon could not be measured alone on the RDE, the faradic and non-faradic currents were separated using the methods presented in Section 3.11. The resulting faradic and non-faradic voltammograms are given in Figures 4.47 and 4.48, respectively. It should be noted that both the faradic and non-faradic currents in Figures 4.47 and 4.48 are for the system as a whole, and not for $YMnO_3$ alone.

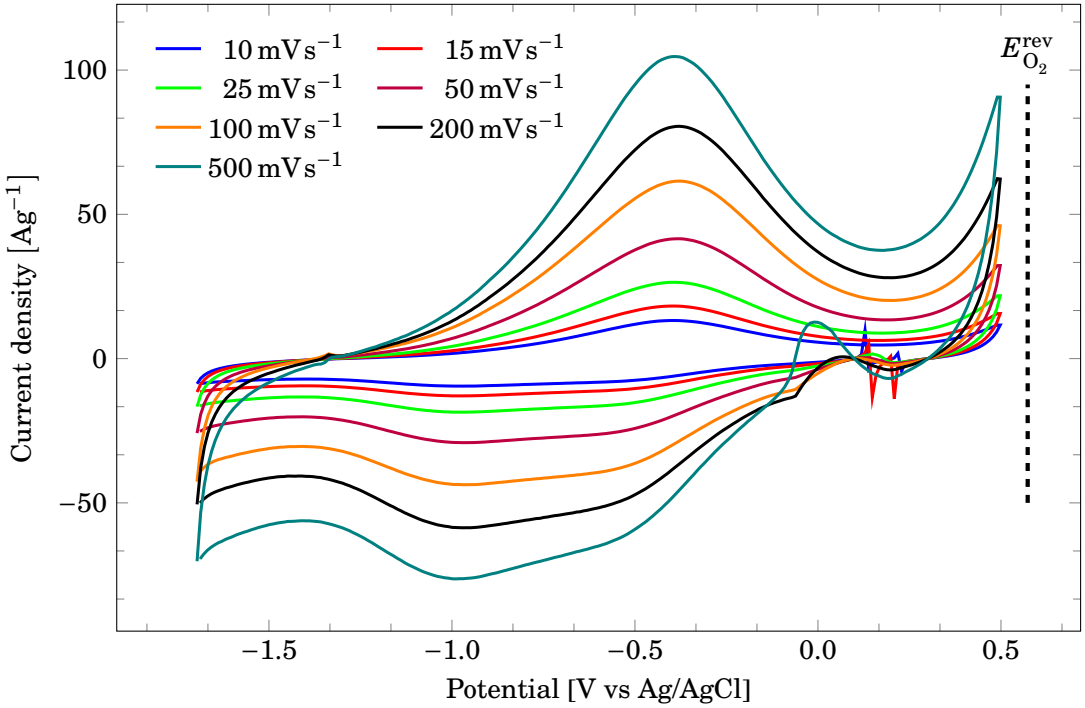

Figure 4.47: The faradic components of Figure 4.12

Although an oxidation plateau appeared to be present in Figure 4.18, when mesoporous carbon ST3 was used, it was only present at one sweep rate and unstable during cycling. The results were thus not further processed.

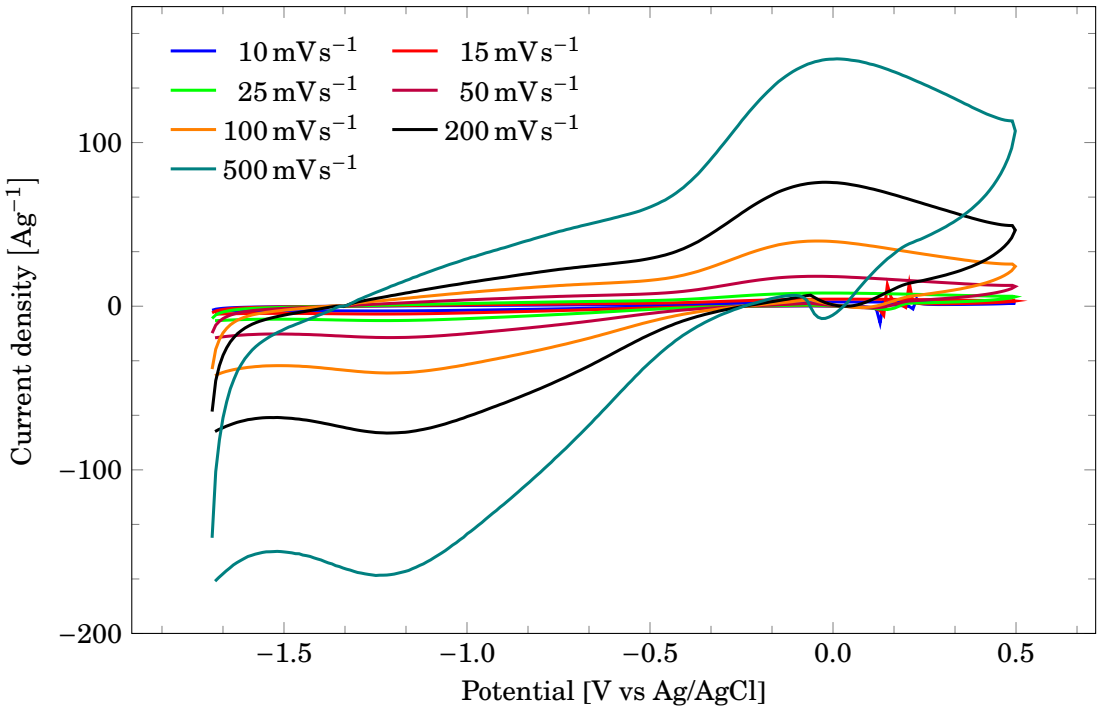

Figure 4.48: The non-faradic components of Figure 4.12

4.8.2 Rod

Removing the non-faradic currents from the experimental data in Figure 4.33, using the method presented in Section 3.11 ($I_f = I\left(\frac{K}{1+K}\right)$), made distinct peaks emerge. In Figure 4.49, The anodic (a) and cathodic (c) peaks A and B have been pointed out. The voltammogram in Figure 4.49 is the sum of the faradic currents on the mesoporous carbon and $YMnO_3$.

Removing the current contribution from mesoporous carbon (given in fig. 4.36) with point by point subtraction resulted in the voltammogram in Figure 4.50. As have been pointed out, three slight features can be observed.

Further separation of I_f and I_{nf} after removal of the MC current (performing $I_f = I_{meas}\left(\frac{K}{1+K}\right)$ on fig. 4.50) clearly demonstrates the presence of redox-pair B, as well as a possible second pair C. The anodic point marked A_a earlier became a plateau, with a corresponding inverse cathodic peak, as seen in Figure 4.51.

Even though no voltammogram was recorded for mesoporous carbon in 1 M KOH, the non-faradic current could still be removed. The faradic signal is given in Figure 4.52. The same peaks A and B can be seen as for 3 M KOH (fig. 4.49).

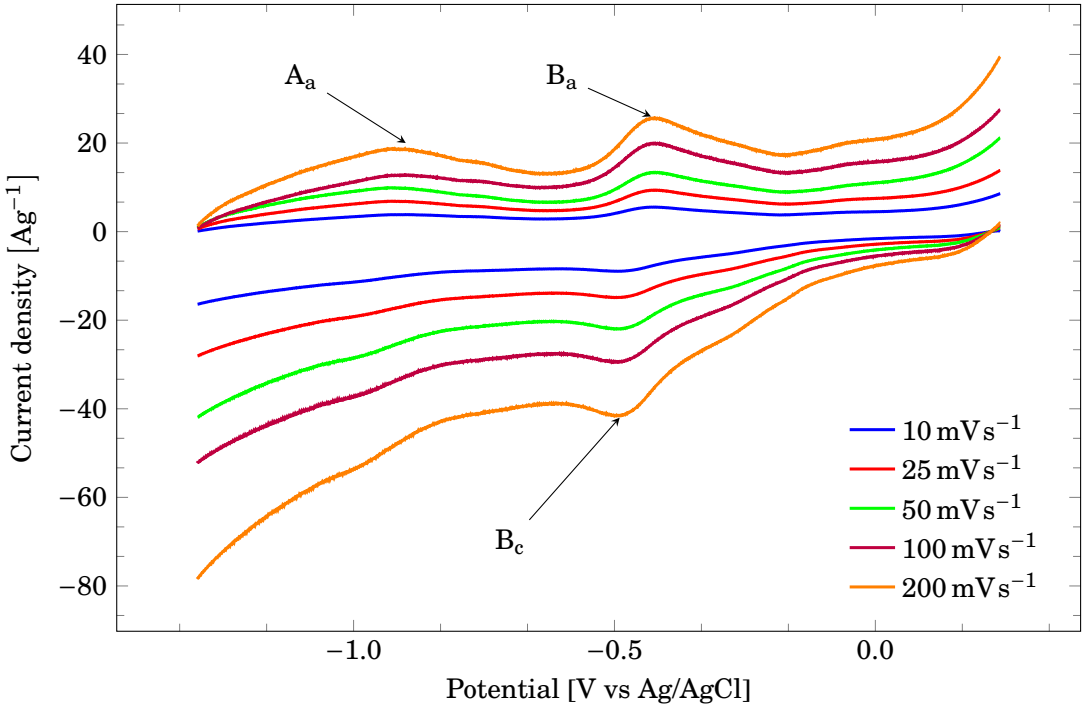

Figure 4.49: The extracted faradic signal from Figure 4.33). The data are from nanocrystalline $YMnO_3$ supported on mesoporous carbon ST8, deposited on the GC rod, scanned in N_2(g) purged 3 M KOH. Faradic currents from both mesoporous carbon and $YMnO_3$ are present.

.

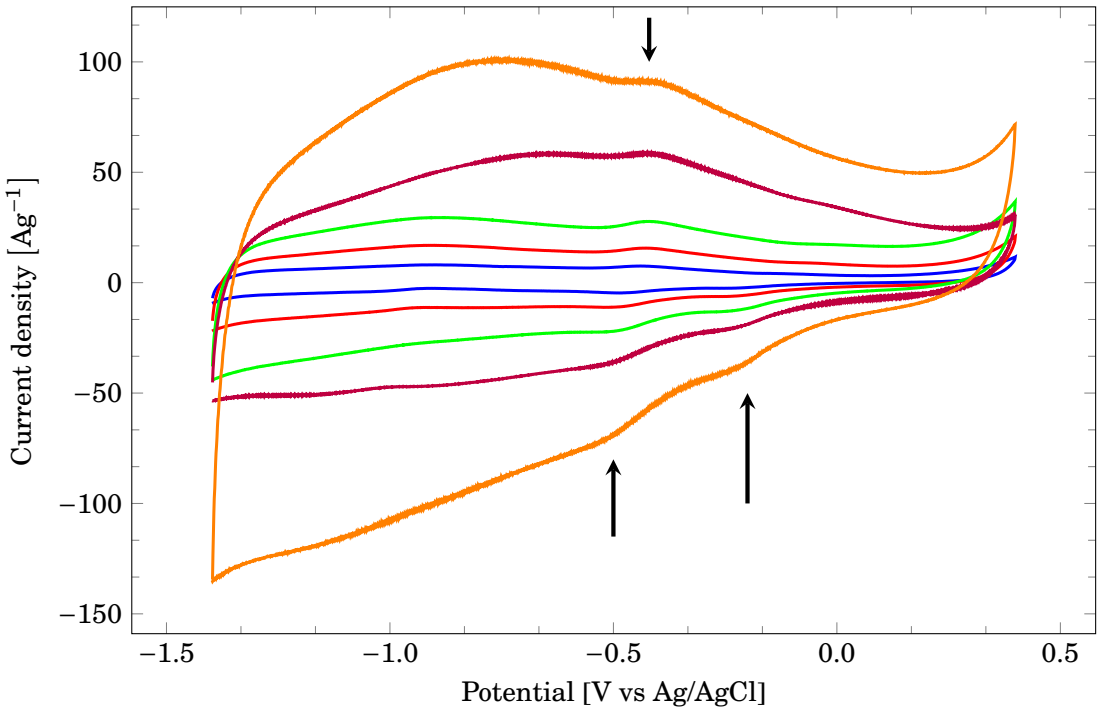

Figure 4.50: Cyclic voltammogram of nanocrystalline $YMnO_3$ on the GC rod in N_2(g) purged 3 M KOH. The background current from mesoporous carbon has been removed.

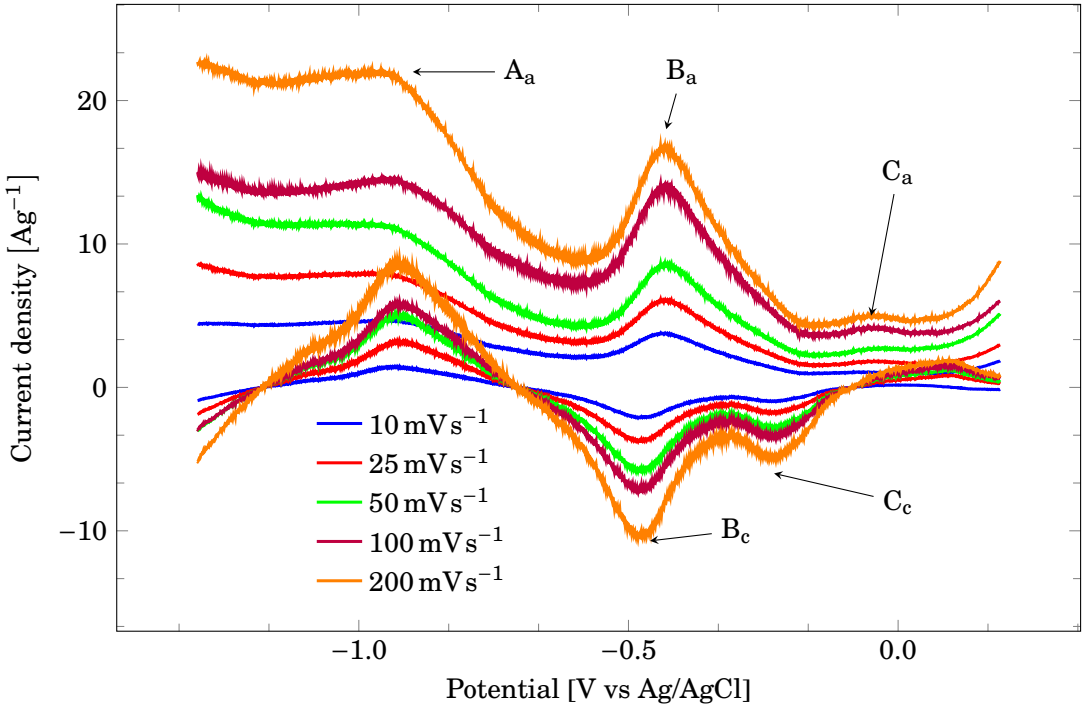

Figure 4.51: The purely faradic current from nanoparticles of $YMnO_3$ on the GC rod cycled in 3 M KOH at different sweep rates. The anodic and cathodic peaks have been marked as either A, B or C with the appropriate subscript.

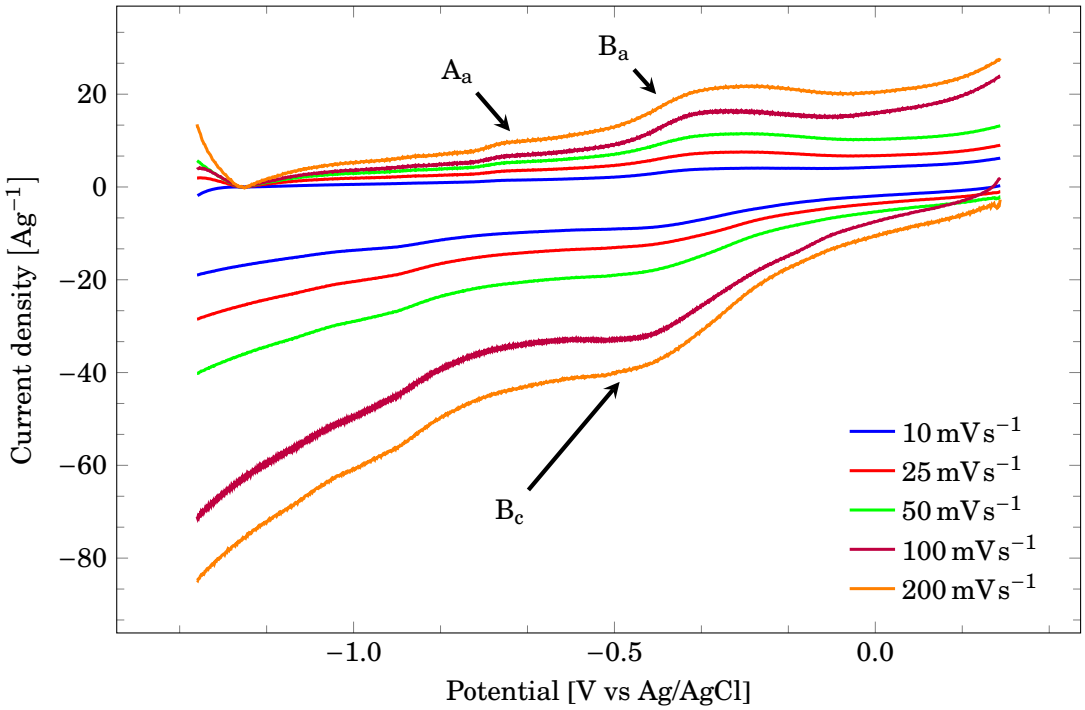

Figure 4.52: The extracted faradic signal from Figure 4.35. The data are from nanocrystalline $YMnO_3$ supported on mesoporous carbon ST8, deposited on the GC rod, scanned in N_2(g) purged 1 M KOH. Faradic currents from both mesoporous carbon and $YMnO_3$ are present.

.

Chapter 5

Discussion

5.1 Stability of $YMn_{1-x}Ti_xO_{3\pm\delta}$

The weight loss of 0.0117 g after suspension of bulk $YTi_{0.12}Mn_{0.88}O_{3\pm\delta}$ in 3 M for 4 days can most likely be attributed to loss of material during decanting. With a starting weight of 1.8653 g, the difference is only 0.63wt%. Combined with the identical XRD results before and after, it can be safely assumed that the hexagonal phase is stable. A question that still remains is whether the structure is stable when a potential is applied. In [49], it was found that the perovskite $La_{1-x}Sr_xCoO_3$ corroded during cycling in 1 M NaOH. Although this work did not investigate this possibility, characterizing the topography of the surface of a polished pellet before- and after cycling in a flat specimen electrode should provide insight into this phenomenon.

The observed reduction in anodic peak current during cycling would not be in agreement with $2Mn_{Mn}^{x} + 2OH^- \rightleftharpoons 2Mn_{Mn}^{\bullet} + O_i^{''} + 2e^-$. As presented Sections 2.3 and 2.5, the electronic conductivity should increase with increasing oxidation of manganese. On the other hand, it do agree with the reduced peak current in the cathodic direction, as would be the case for loss of oxygen. This will of course depend on the initial oxidation state of the sample, whether Ti-substitution is compensated for by reduction of manganese or oxygen excess.

A fully oxidized sample will have a high content of Mn^{4+}, increasing the tolerance factor towards the orthorhombic perovskite, as presented in Section 2.1. As thermal treatments did not cause a transition from the hexagonal to the orthorhombic phase in[14], the low cation mobility at room temperature should not allow cation diffusion, even under an applied potential. Indeed, if there is a net change in composition during cycling, it will most likely be caused by irreversible intercalation or extraction of oxygen and/or corrosion of cations.

5.2 Glassy carbon electrode without binder

As mentioned in Sections 4.4 and 4.5, unsupported particles deposited onto glassy carbon without Nafion™ would not stick sufficiently to the surface. The SEM images in Section 4.7 showed that the film at $1\,mg\,cm^{-2}$ was most likely thicker than only one particle. It its possible that most of the excess material fell off, leaving only a monolayer of particles on the glassy carbon surface. This could have been investigated in SEM. However, after electrochemical characterization, the electrode would have to be rinsed carefully with DI water so that the surface would not be covered in crystallized KOH. As reported, attempts to wash the electrode only lead to more particles being removed from the surface. The resulting image would provide some information, but it would most likely not be representative of the actual state of the

surface before it was rinsed. The loss of material would also make it hard to gain sufficient sample sizes for XRD and XPS analysis[35]. Although better results were obtained with the rod-electrode than the RDE, rinsing it with DI water would suffer from the same problem.

Whether particles stay at the glassy carbon surface or not is not only dependent on the contact force between particle and carbon. The electrolytes ability to wet both surfaces can be crucial. If the electrolyte wet both the particle and electrode surface very well, the particles may lifted up from the surface, regardless whether the RDE or rod are used. Also, even if the particles stay at the rod surface, it does not guarantee proper electrical contact. Only a small fraction of the area of a particle could be in contact with the electrode.

5.3 Effect of Nafion™

Independent of the Nafion™ concentration, the current response for the $1\,\mathrm{mg\,cm^{-2}}$-films was in the range $-400\,\mathrm{mA\,g^{-1}}$ to $200\,\mathrm{mA\,g^{-1}}$. Either, the Nafion™ did not affect the measurements, or it most likely covered the surface, preventing anion diffusion. Regardless, the addition of Nafion™ gave sufficient adhesive properties with as little as 0.025wt% Nafion™ in ethanol for a suspension load of $1\,\mathrm{mg\,mL^{-1}}$. Comparing the voltammograms for 30wt% $YMnO_3$ on MC ST3 with and without Nafion™ (figs. 4.19 and 4.25) reveals that even though sufficient binding was achieved, most of the $YMnO_3$ surface was most likely not accessible for the hydroxide ions. Even though Na-substituted Nafion™ was used in [2], the procedure of which the polymer film was applied both there and in this work may rise some questions as to how it affects the electrochemical properties of both electrode and particles. As the Nafion™ in ethanol solution evaporates during spin coating, a thin layer of polymer will cover the entire surface. Nafion™ being a proton conductor (or cation for other variations of it), will not conduct hydroxide ions, and will for the specific case of intercalation of oxygen in an alkaline solution, effectively block the surface of $YMn_{1-x}Ti_xO_{3\pm\delta}$, rendering the use of Nafion™ counter-productive. This would also be true for most dissolved polymers. Rather, it should be attempted to use an alkaline ionomer in suspension as a binder. At least one product is available commercially[(a)]. Creating a suspension of nanocrystalline $YMn_{1-x}Ti_xO_{3\pm\delta}$ and ionomer particles could potentially create the same effect as loading the oxide onto mesoporous carbon, i.e. gaining a high surface area. Although it may work, it is unknown how an ionomer would affect both the electrochemical measurements and other analysis techniques like XRD, EDS and XPS.

5.4 Starbon™ 300 and 800

According to the data provided by Sigma Aldrich[42, 43], the main difference between the two types is the porosity. The higher-temperature treated ST8 has a higher total surface area, although the particle sizes should be the same. Also, according to the order confirmation in Appendix G, the pore surface of the ST8 is hydrophobic whereas the ST3 has a hydrophilic pore surface[43]. According to [39], the stability in alkaline solutions increases with Starbon™ preparation temperature. So does the transition from starch to carbon. Although it was decided to test mesoporous carbon ST3 due to the hydrophilic pore surface, which could possibly enhance the electrical contact at the electrode-solution interface, the lower stability in high pH and presence of functional surface groups[39] may make this product incompatible as a support material for characterization of nanoparticles.

[(a)] `http://www.actaspa.com/products/ionomer-i2/`

5.5 Electrochemical response of mesoporous carbon

The shape of the voltammogram in Figure 4.12 with nanoparticles of $YMnO_3$ loaded onto mesoporous carbon ST8 was also observed in earlier work[6] for electrodes of only ST8 at the same mass loading in purged 1 M KOH. The voltammogram in Figure 5.1 is reprinted from earlier work[6].

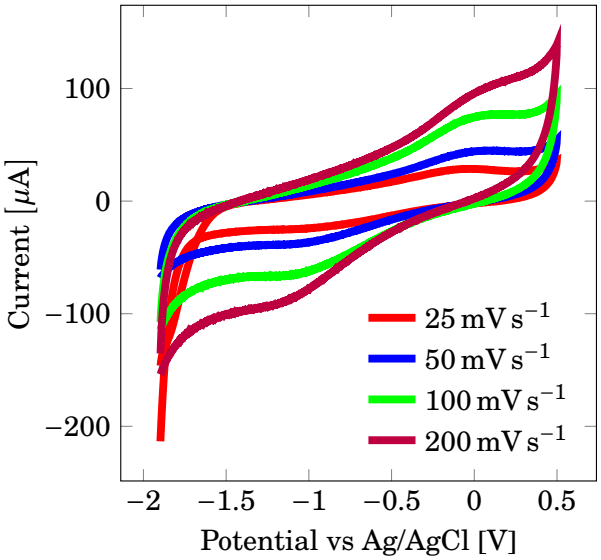

Figure 5.1: Cyclic voltammogram of mesoporous carbon ST8 in N_2(g) purged 1 M KOH. Reprinted from earlier work[6].

This strongly indicates that an electrochemical response from $YMnO_3$ was not present in Section 4.4.3 - Figure 4.12, and that the observed curve shape is the response of mesoporous carbon only. Although, it does not explain the cathodic peak in the first cycle of MC ST8 in this work (fig. 4.16). If this was a catalytic hydrogen evolution reaction on the mesoporous carbon, then there are two possibilities. Either, the presence of $YMnO_3$ suppresses the formation of hydrogen gas, or proper electrical contact between the MC-$YMnO_3$ film and glassy carbon was not established in Figure 4.12. The same arguments can be made if the peak is attributed to intercalation of K^+ into the mesoporous carbon. However, considering that the phenomenon in Figure 4.16 did not occur in earlier work nor on the GC rod, it will be treated as an outlier. Should this be observed on a later occasion, it should be investigated.

5.6 Electrochemical response

In earlier work, an electrochemical response of $YMnO_3$ supported on MC ST8 at the GCRDE was identified in N_2(g) purged 3 M KOH, reprinted in Figure 5.2. Subtraction of the current contribution from MC revealed clear redox-peaks in Figure 5.3. These voltammograms bear a striking resemblance to the response of $YMnO_3$ on the rod (fig. 4.51). Combined with the arguments made in Section 5.5, it can be concluded that the voltammogram of $YMnO_3$ in N_2(g) purged KOH can be characterized by an oxidation peak around −0.45 V and reduction peaks around −0.2 V and −0.5 V vs Ag/AgCl (figs. 4.34, 4.51 and 5.2). A possible explanation for the two cathodic peaks versus only one anodic, is that hydroxide ions adsorb at surface vacancies at zero applied potential. The anodic peak then corresponds to an intercalation mechanism similar to the one presented in Section 2.6.1 - Equation (2.28). As the potential sweep is reversed,

surface oxygen species are first protonated and then desorbed, at two different potentials. This of course can not be said with confidence, and should be researched in further work.

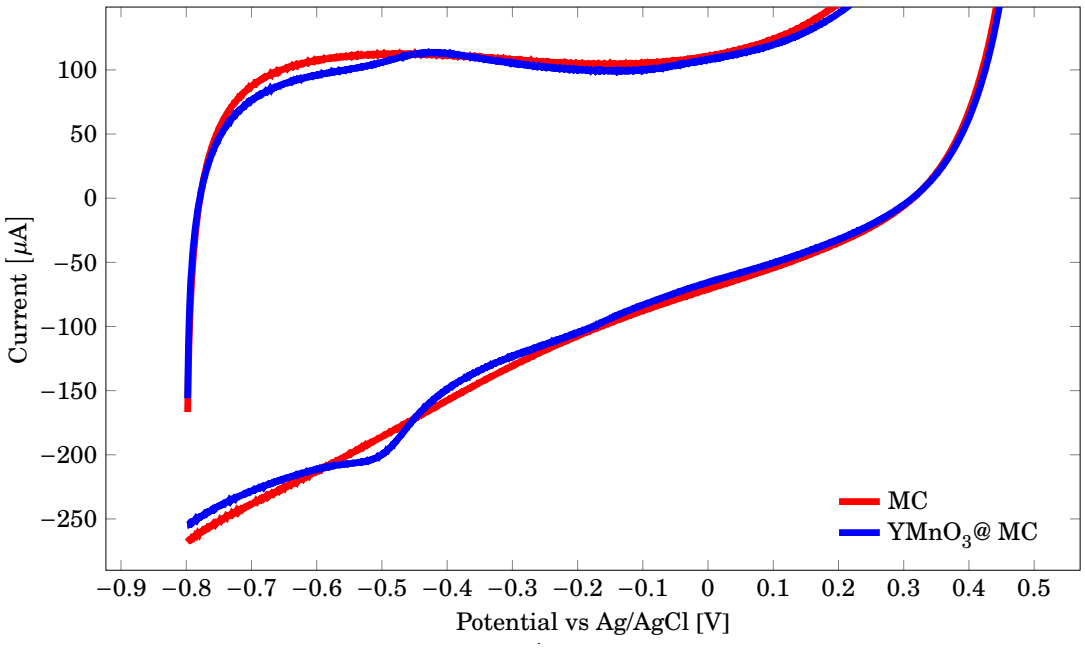

Figure 5.2: Cyclic voltammogram of $YMnO_3$ supported on mesoporous carbon ST8 on the GCRDE in N_2(g) purged 3 M KOH at 100 $mV s^{-1}$. There is an absence of redox peaks in the curve for mesoporous carbon. Reprinted from [6]

.

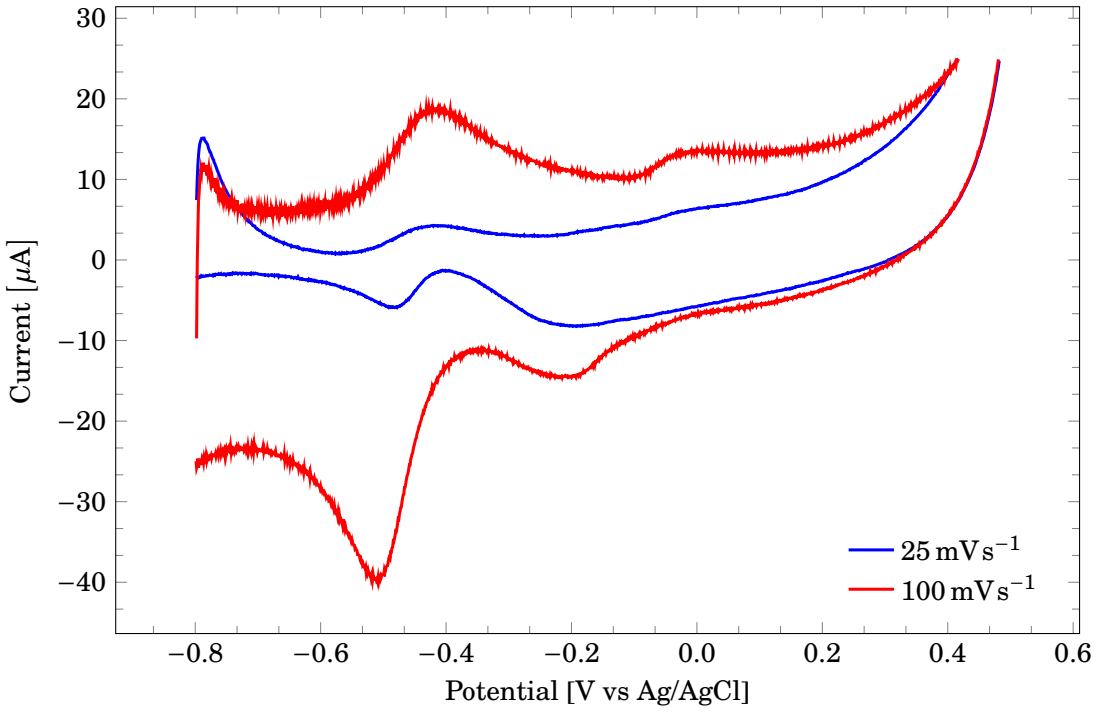

Figure 5.3: Cyclic voltammogram of $YMnO_3$ on the GCRDE in N_2(g) purged 3 M KOH at 100 $mV s^{-1}$ and 25 $mV s^{-1}$. The current contribution from mesoporous carbon has been subtracted out. Data was from earlier work[6].

5.7 Peak potential and pH dependency

Most of the anodic peaks that could be observed in the cyclic voltammograms appeared around −0.45 V. In the same potential area, there is an absence of a peak in the voltammogram of mesoporous carbon ST8 (fig. 4.36). While the recorded voltammograms of nanocrystalline $YMnO_3$ are not equal for the RDE and the rod, the anodic peaks of the faradic components (figs. 4.47 and 4.51) are located at approximately this potential. Even bulk $YTi_{0.12}Mn_{0.88}O_{3\pm\delta}$ on the rod produced an anodic peak around this potential. However, as mentioned earlier, the peak potential appears to be dependent on the cathodic turnaround potential. The measured current is the sum of the faradic and non-faradic currents. In Figure 4.48, it can be seen that the non-faradic current peaks around E =0 V. Due to the non-faradic current scaling linearly with the sweep rate, whereas the faradic scales with the square root, the total peak potential will shift towards that of the non-faradic current at higher sweep rates.

Comparing the results in this work to those of [2] in Figure 2.8, it should be possible to observe one or two single peaks at negative potentials. However, as presented in Section 2.6.1, [7] found that the intercalation mechanism in Equation (5.1) occurs at potentials preceding oxygen evolution, and can be observed by an oxidation plateau in the voltammogram.

$$A_xMO_y + 2\delta OH^- \rightleftharpoons A_xMO_{y+\delta} + \delta H_2O + 2\delta e^- \tag{5.1}$$

By comparing the sweeps performed at 25 $mV\,s^{-1}$ on $YMnO_3$ on the glassy carbon rod electrode in 1 M and 3 M KOH, it is clear that the peak shifts to more negative potentials with increasing pH. A plateau followed by a peak can be seen for both concentrations in Figure 5.4.

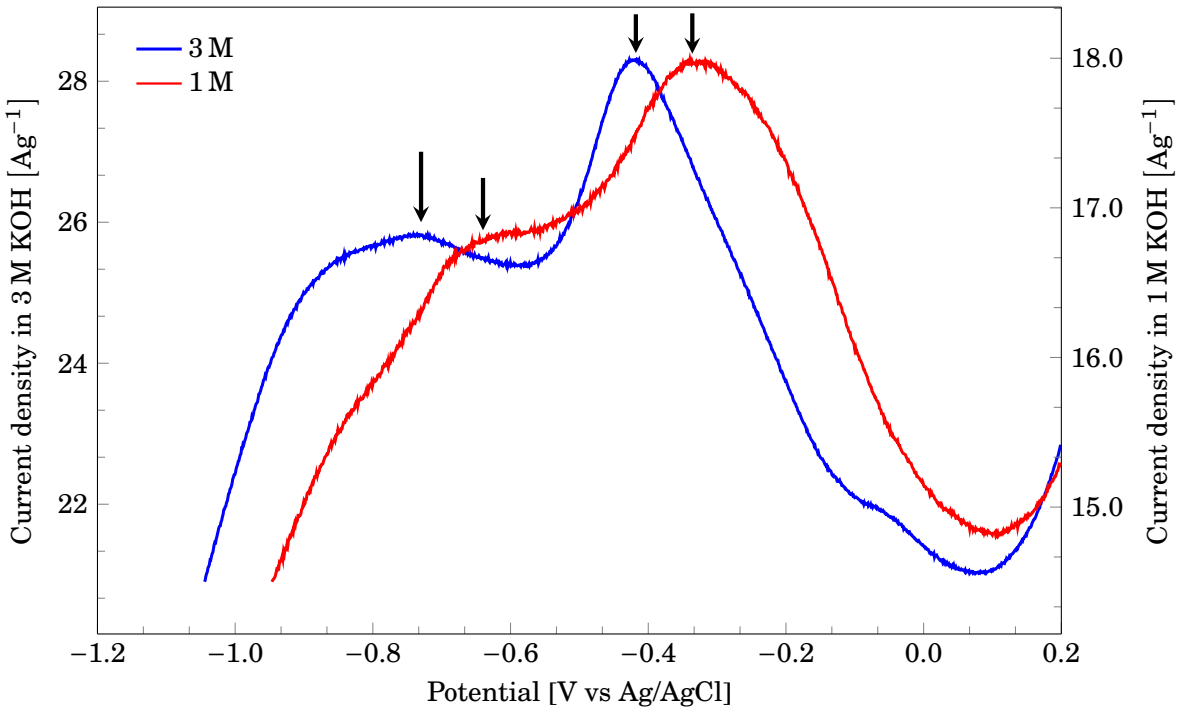

Figure 5.4: Comparison of the peaks present in the experimental CV curves of $YMnO_3$ supported on mesoporous carbon ST8 when using two different concentrations of KOH. The peak potential clearly shifts to more negative potentials as pH is increased. Sweep rate is 25 $mV\,s^{-1}$.

The difference in peak potential is ΔE =70 mV with peak potentials being $E_p(3\,M) \approx -0.42$V and $E_p(1\,M) \approx -0.35$V at all sweep rates. Applying the Nernst equation on Equation (5.1) to estimate

the difference in peak potential between the 3 M and 1 M KOH solutions gives $\Delta E_p(\text{Nernst}) \approx 28\,\text{mV}$ from Equation (5.5), which is $\frac{1}{2.5}$ of the experimental difference. The measured and calculated values for ΔE_p are not equal, which may indicate that a different mechanism is occurring. Of course, the calculated value is a simplification, as the activity of the oxide species has been assumed to be 1.

$$\Delta E_p(\text{Nernst}) = E_p(3\,\text{M}) - E_p(1\,\text{M}) \tag{5.2}$$

$$\Delta E_p(\text{Nernst}) = \frac{RT}{F}\ln(3) - \frac{RT}{F}\ln(1) \tag{5.3}$$

$$\Delta E_p(\text{Nernst}) = \frac{8.314[\text{J K}^{-1}\,\text{mol}^{-1}] \times 298[\text{K}]}{96485[\text{C mol}^{-1}]}\ln(3) \tag{5.4}$$

$$\Delta E_p(\text{Nernst}) = 28.2\,\text{mV} \tag{5.5}$$

Although only two concentrations of KOH were used before the equipment broke, the same trend can be seen for all sweep rates after removal of the non-faradic currents (three sweep rates are plotted in fig. 5.5).

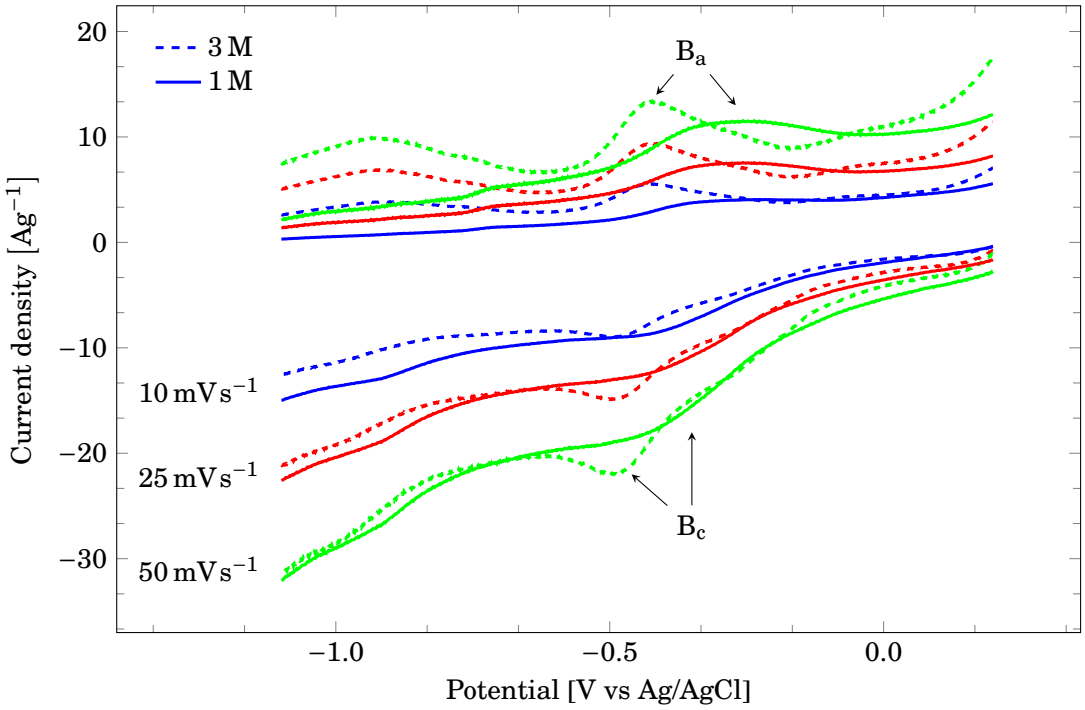

Figure 5.5: Comparison of the faradic currents of nanocrystalline $YMnO_3$ supported on MC ST8, deposited on the GC rod. The difference in peak potential is equal for all three sweep rates.

This strongly indicates that both the marked peaks are related to hydroxide ions. The peaks potential are lower than the reversible potential for oxygen evolution and thus not connected to the oxygen evolution reaction.

The oxygen reduction reaction[37] (ORD) in Equation (5.6) is related to the intercalation mechanism in Equation (5.1). The main difference being the oxidation products, either O^{2-} or O_2(g). A possibility is that the peaks in e.g. Figures 4.15 and 4.34 are related to intercalation or manganese oxidation, while peaks the peaks in Figure 4.47 ($YMnO_3$ on RDE) is Equation (5.6) on the glassy carbon. That being said, the reduction reaction should not occur, as the electrolyte was purged with N_2(g).

$$O_2 + 2H_2O + 4e^- \rightleftharpoons 4OH^- \qquad E^0 = 0.401\text{V vs NHE} \tag{5.6}$$

5.8 Evaluation of the different experimental setups

All three of the different experimental setups used in this work all had both advantages and disadvantages. Even though the RDE and rod are principally the same, the subtle differences affect the experimental results to such an extent that careful consideration should be made when choosing the working electrode.

5.8.1 Glassy carbon RDE

Using a glassy carbon rotating disc electrode as the working electrode is a well known method. By spin coating, a consistent thin film can be obtained as many times as needed. The main challenge in using this method lies in the contact forces between the thin film and the glassy carbon surface. If the adhesion is insufficient, it is necessary to use an adhesive agent to ensure that the deposited particles stay in place. Of course, the electrolyte plays an important role in this. In most cases, a variation of Nafion™ can be used, as it will readily transport protons or small cations. In highly alkaline conditions, however, the solution is not as simple. As demonstrated in this work and discussed earlier, a very small amount of Nafion™ is needed in order to obtain sufficient adhesive properties. However, even small amounts will block anion transport and render the use of Nafion™ counter productive. A completely different approach, as was attempted in Appendix B, is to glue a small sintered pellet onto the RDE. Using carbon tape did not work for this application. Although not attempted, conducting glue could potentially yield excellent results, but the glue would be rather permanent, hence potentially damaging the RDE.

5.8.2 Glassy carbon rod

By allowing gravity to pull the deposited material towards the glassy carbon surface, the problem with adhesion was partially solved. Even so, this method has it's own set of disadvantages. The cell was slightly too small, so pushing the rod through the rubber seal from above was not possible. The rubber seal would touch the surface of the rod when pushing it through, so it had to be placed in the cell before coating. Therefore, drop coating had to be used, which does not necessarily yield consistent thin films. The long, thin rod of glassy carbon could not be successfully mounted in a SEM sample holder. The deposited particles did indeed stay at the glassy carbon surface, as long as there was no stirring of the electrolyte. Due to the principle design of this setup, the cell had to be filled with electrolyte after the deposition had been performed. If the cell was not filled very slowly, the particles would easily be washed away, which happened on many occasions. This also applies to removing the electrolyte, and washing the electrode. Nevertheless, the method produced promising results that should be investigated in further work. The rod electrode is well suited for electrochemical measurements, as long as there is no need for further characterization of the sample. As long as no rotation of the electrode is required during cycling, the rod may be a better alternative than the RDE, due to the fact that the particles doe not fall off. Most of the disadvantages can also be worked around. If the rod can be properly insulated on the sides, and a modified electrode can be placed inside the cell without damaging the surface, then it should be possible to spin coat a thin film onto the rod.

5.8.3 Flat specimen electrode

Much like the voltammogram of La_2CuO_4 presented in Figure 2.10, the sintered disc in the flat specimen electrode had an oxidation plateau in the voltammogram. Considering that such a plateau was potentially observed for nanocrystalline $YMnO_3$ as well, it is highly likely that this is caused by the oxidation of manganese, as has been reported for many different perovskites[33]. The main drawback of this electrode is that the sample needs sufficient mechanical strength so that it does not break, which happened in this work. An effect of this is that a dense sample with good mechanical properties will have a low surface area. Of course, in the case of oxygen intercalation, the current generated by the oxidation of manganese may be limited by the bulk diffusion rate of oxygen. Ionic transport is faster at surfaces than through the bulk of a material. If a dense disc could be created from nanoparticles, the diffusion distance though the grains would be minimized, given that the grain boundary diffusion is much more rapid than bulk diffusion. If sufficient strength proves difficult to achieve, the pellet should be embedded in epoxy. This was done in [49], when oxygen evolution on pellets of the perovskite $La_{1-x}Sr_xCoO_3$ (LSCO) was studied in alkaline solution. In order to establish proper electrical contact between the pellet and copper contact in the sample holder, colloidal suspended silver was added to the backside of the pellet. In the thesis, cyclic voltammetry was performed in 1 M NaOH at $20\,mV\,s^{-1}$ on pellets of different values of x. In contrast to this work, which experienced a reduced current density for each cycle, LSCO suffered from corrosion during cycling, which led to an increased surface area, and hence current density. The successful measurements on pellets of LSCO is proof that the method can be used.

The use of a pellet would also allow for the creation of a high surface area by mimicking a membrane. Sintering a thin dense film onto a porous substrate would produce an electrode with a very high surface area. If this can be done successfully, a very high capacitance could be achieved.

Even though a disc electrode would most likely suffer from diffusion limitations through the bulk of the material, this could also be used as an advantage. With EDS, the oxygen content of samples that has been oxidized and reduced could be compared. Furthermore, $LaMnO_3$ suffered from surface segregation of manganese during cycling. Should this occur in $YMnO_3$, EDS could identify the difference in atomic percent of manganese at the surface before and after cycling.

5.8.4 Suggestions to electrode improvements

First of all, it required a bit of trial and error to insulate the sides of the GC rod with a shrinking tube. Altering the design of the glass cell used for the rod so that the RDE can be used would make spin coating possible. A second suggestion that could improve the rod electrode setup, is to create walls around the GC surface. If the insulating material around the glassy carbon are ever so slightly higher than the GC, then the thin film might be protected from flowing electrolyte. Of course, this would make polishing of the electrode ever so harder. Nevertheless, a new design should be made for characterization of powders.

Other than using the flat specimen electrode, a different approach could be to embed the pellet in a soft polymer/other material (e.g. beeswax). Electrical contact would have to be established between the sample and one or more copper(or other metal) wires. The sample- and wire would then be dip-coated in the polymer. By masking a known area of the pellet, and removing the polymer in this area, a known surface area can be established. The pellet-wire combo could be suspended into the electrolyte as the working electrode. The challenges in this method would be achieving proper electrical contact between the wire and pellet (copper/silver-tape could be

used), polymer compatibility with the electrolyte and removing the polymer and masking from the exposed surface area.

5.8.5 Remarks regarding the experimental execution

What was not done, but should have been done, was polarization curves. Before performing CV, polarization curves should have been recorded in order to determine the potential for oxygen and hydrogen evolution. Although the anodic turnaround potential never exceeded 0.5 V, which is below the reversible potential for oxygen evolution in 3 M KOH (≈0.56 V vs Ag/AgCl), the resulting voltammograms could still indicate that oxygen evolves prior to this point. Of course, the most likely explanation is that the potential of the Ag/AgCl electrode vs NHE was different from +0.197 V. This should also have been measured.

5.8.6 Separation of faradic and non-faradic currents

The method used to separate the faradic and non-faradic currents produced diverging points. Using the absolute value of the currents reduced this, but it still produced noise in the voltammograms. Although the equations $I_f = \alpha\sqrt{v}$ and $I_{nf} = \beta v$ could have been used directly to produce divergence-free voltammograms, $I_f + I_{nf}$ would in most cases not sum up to be equal the total current, as seen in Figure 5.6.

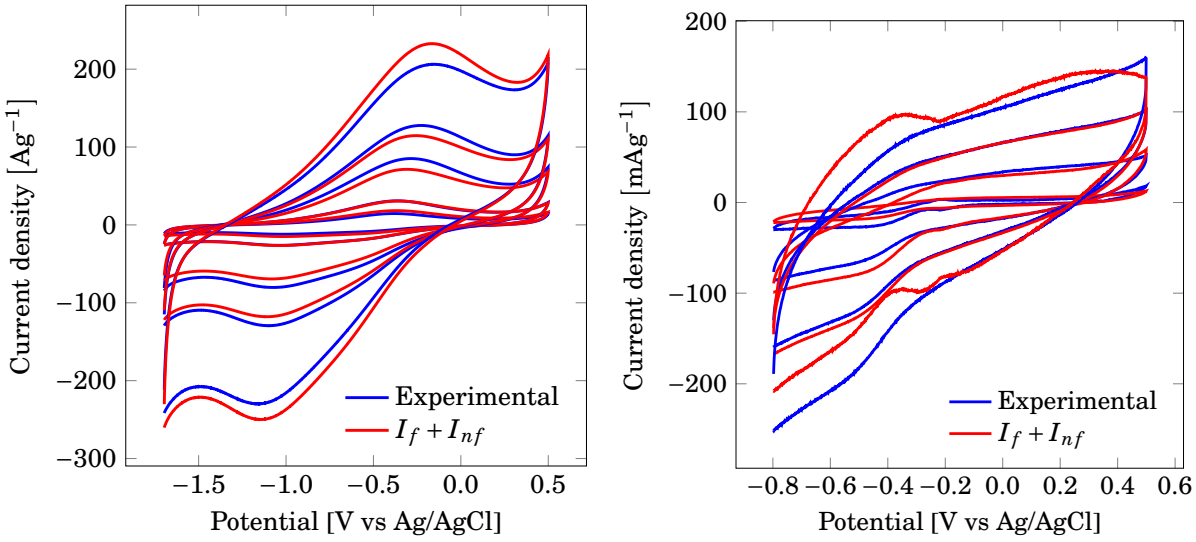

Figure 5.6: Comparison of the total measured current, and the summation of $I_f + I_{nf}$ after separation with $I_f = \alpha\sqrt{v}$ and $I_{nf} = \beta v$.

By defining $I_f + I_{nf} = aI + bI = I$, given the constraint $a + b = 1$, the method used can be justified

with Equations (5.7) to (5.21):

$$I = I_f + I_{nf} \tag{5.7}$$
$$I = aI + bI \tag{5.8}$$
$$I = \alpha\sqrt{v} + \beta v \tag{5.9}$$

$$I_f = aI = \alpha\sqrt{v} \tag{5.10}$$
$$a = \frac{\alpha\sqrt{v}}{I} \tag{5.11}$$
$$a = \frac{\alpha\sqrt{v}}{\alpha\sqrt{v} + \beta v} \tag{5.12}$$
$$a = \frac{\alpha}{\alpha + \beta\sqrt{v}} \tag{5.13}$$

$$I_{nf} = bI = \beta v \tag{5.14}$$
$$b = \frac{\beta v}{I} \tag{5.15}$$
$$b = \frac{\beta\sqrt{v}}{\alpha + \beta\sqrt{v}} \tag{5.16}$$
$$b = \frac{\beta\sqrt{v}}{\alpha + \beta\sqrt{v}} \frac{\alpha^{-}1}{\alpha^{-}1} \tag{5.17}$$
$$b = \frac{\frac{\beta}{\alpha}\sqrt{v}}{1 + \frac{\beta}{\alpha}\sqrt{v}} \tag{5.18}$$
$$b = \frac{K}{1+K} \tag{5.19}$$

$$a = 1 - b \tag{5.20}$$
$$a = 1 - \frac{K}{1+K} \tag{5.21}$$

Thus, justifying Equations (3.4) and (3.5) and the derivation given in Appendix C.

5.9 Diffusion coefficients

A model to estimate the diffusion coefficient of oxygen in the perovskite $Ca_{0.5}La_{0.5}FeO_{2.618}$ (CLFO) has been developed by [34, 36]. The model assumes that the diffusion coefficient is independent of the oxygen content, and requires galvanostatic (constant current) discharge curves to be recorded. This was not done in this work, and it has not been found a model that takes into account diffusion towards- and inside particles. In the aforementioned work, CLFO was reduced at a constant current. When no more oxygen could be extracted, a steep change in the potential was observed. Although no constant current measurements are mentioned in the paper characterizing $LaMnO_3$[2], the supplementary information [35] states the diffusion coefficient was calculated from CV curves using the aforementioned model. An e-mail should be sent to the corresponding authors in order to ask what was done.

5.10 Further work

Based on the results discussed earlier, a comprehensive suggestion for further work will be presented. Due to the inherent problems with characterizing a thin film, further work will be based on the flat specimen electrode.

Bulk particles can easily be made phase pure by solid state synthesis. With the proper pre-consolidation and sintering program, it should be possible to create dense and strong pellets of phase pure $YMn_{1-x}Ti_xO_{3\pm\delta}$. In order to gain sufficient electronic conductivity and minimize microcracking, it would be advantageous to perform the initial investigation using a titanium doping level of e.g. x=15 in $YMn_{1-x}Ti_xO_{3\pm\delta}$.

When sintering of dense strong pellets has been achieved, it can either be attempted to mount them directly in a flat specimen electrode, or they can be embedded in epoxy. It should be noted that the suggested pellet diameters are 2cm for direct mounting and 1cm for epoxy, but this is based on the equipment that was available during this work. In order to gain sufficient electrical contact between the pellet and the electrode, colloidal suspended silver could be added to this interface.

Prior to electrochemical characterization, the surface of the pellets should be polished and characterized by gracing incidence XRD, SEM or light microscopy and EDS. If possible, the topography of the polished samples can be investigated using AFM, in order to determine the roughness factor and adjust for the real surface area. This was done in [49]. Of course, the oxygen content of the samples should be determined using TGA.

An appropriate electrochemical characterization program should then be deployed. First, the potential for oxygen and hydrogen evolution should be found from the corresponding polarization curves. The second step would be to investigate the stability during cycling. Performing e.g. 100-500 cycles at a sufficient low sweep rate (15 or 20 $mV\,s^{-1}$) should give information about the cycling stability. The cathodic and anodic turnaround potentials should not exceed that of gaseous evolution. Any eventual peak in the voltammogram would also be identified during these cycles. After thoroughly rinsing the pellet with DI water, and possibly drying in an exicator, the surface should once again be characterized using the aforementioned methods. If the data do not indicate the exchange of oxygen, it can be attempted to use a higher concentration of KOH and a lower sweep rate. If surface segregation of manganese is observed, then a mechanism similar to that in [2] probably occurs during cycling.

If one or more redox peaks can be identified in the voltammogram, the next step would be to fully oxidize and reduce two samples using either galvanostatic or potentiostatic methods. Differences in the surface composition between the samples would confirm the presence of oxygen exchange in $YMnO_3$. Although destroying the sample, EDS of a cross section could give some insight into the whether oxygen exchange extends into the bulk of the pellet. The same applies to using TGA to determine the difference in oxygen content between the two samples. The difference in atomic percentage of oxygen in e.g. $YMnO_{2.9}$ and $YMnO_{3.1}$ is only 1.6%, which may be within the margin of error for EDS, rendering TGA the only option.

For comparison with the results obtained in this work, cycling should be performed in e.g. 1, 3 and 6 M KOH in order to determine the pH dependency of the peak potential. Even better would be to use e.g. 1, 2, 3, 4, 5 and 6 M, as everything will have a linear dependency if only two data points are collected, and three data points will always fit a quadratic function. The pH dependency of the peak potential could be used in combination with other obtained data to suggest a mechanism for the intercalation of oxygen into $YMnO_3$.

If intercalation can be confirmed for a single value of x in $YMn_{1-x}Ti_xO_{3\pm\delta}$, a model for diffusion

towards a surface, with subsequent diffusion inside the pellet should be established. Determining the diffusion coefficient of oxygen for different compositions, e.g. x=0, 0.05, 0.1 and 0.15, would be of great interest for further research. Oxygen deficit $LaMnO_{2.91}$ showed greater capacity for oxygen storage than oxygen excess $LaMnO_{3.09}$[2]. Exploring this dependency in $YMn_{1-x}Ti_xO_{3\pm\delta}$ should be performed for both undoped $YMnO_3$ and $YTi_{0.15}Mn_{0.85}O_{3\pm\delta}$, as the presence of Ti^{4+} is suspected to stabilize interstitial oxygen. However, whether this will enhance the oxygen exchange, or stabilize a specific stoichiometry is unknown. Of course, if oxygen is intercalated into both vacancies and interstitial sites, but at the same potential, a calculated diffusion coefficient will be the average of the two. Two separate peaks in close proximity could indicate that oxygen is first intercalated into interstitial sites prior to vacancies, or the other way around.

The final part of using the flat-specimen electrode should be an ambiguous one. By sintering a thin dense layer onto a porous support, a very high surface area can be achieved. This way, it can be investigated how high capacity a pure pellet of $YMn_{1-x}Ti_xO_{3\pm\delta}$ can achieve.

If no electrochemical response indicating intercalation of oxygen can be achieved, then an effort should be made into developing a method for characterizing a thin film. The suggestions for electrode improvements made in Section 5.8.4 should then be considered.

Chapter 6

Conclusion

The characteristic voltammogram of $YMnO_3$ has most likely been identified with an oxidation peak around $-0.45\,V$ and reduction peaks around $-0.2\,V$ and $-0.5\,V$ vs Ag/AgCl in 3 M KOH. Electrochemical characterization was successfully performed using the glassy carbon rod electrode. However, due to the inherent problems with thin film methods, further work is recommended to be carried out using a sintered pellet in a flat specimen electrode.

Three different electrode preparation methods for electrochemical characterization of $YMnO_3$ in alkaline solution were evaluated. The work focused on assessing each method with respect to reproducibility and practical implications regarding further analysis, beyond electrochemical measurements.

The method used to evaluate the electrochemical response from each electrode was cyclic voltammetry. The electrochemical response for each method was evaluated qualitatively as to whether oxidation of manganese, and subsequent insertion of oxygen into the lattice, was observed.

Without a binder, a thin film spin- or drop coated onto a glassy carbon electrode would not adhere sufficiently well to the carbon. Even though Nafion™ provides sufficient adhesive properties, even when using a very small amount, it will effectively block anion transport towards the active sites of the thin film. The lack of adhesion is a fundamental problem whether the electrode surface is pointing upwards or downwards. Even so, promising electrochemical responses was observed at negative potentials similar to what was observed for $LaMnO_3$[2].

A different approach is to mount a sintered pellet of $YMnO_3$ in a flat specimen electrode. This method has challenges in terms of achieving sufficient mechanical strength of the pellet, and possible limitations if the material is a poor conductor. Only one out of seven sintered pellets was characterized. The other six fractured during either polishing or mounting it in the electrode. The electrochemical response of the pellet was promising, similar to that of other similar materials[11].

To conclude, a recommendation for the use of each electrode type can be made. The RDE electrode may be used if a procedure for the use of a compatible binder can be developed. If a binder is not available, the rod electrode may be used for purely electrochemical measurements. Further work is recommended to focus on the flat specimen electrode due to the inherent problems with characterizing a thin film in an alkaline solution. This facilitates the use of a large sample, making further analysis easier. The thickness of the sample can also be exploited to explore the mechanisms occurring during electrochemical measurements.

Bibliography

[1] K. Bergum, H. Okamoto, H. Fjellvag, T. Grande, M. A. Einarsrud, and S. M. Selbach. Synthesis, structure and magnetic properties of nanocrystalline $YMnO_3$. *Dalton Transactions*, 40(29):7583–7589, 2011.

[2] J. T. Mefford, W. G. Hardin, S. Dai, K. P. Johnston, and K. J. Stevenson. Anion charge storage through oxygen intercalation in $LaMnO_3$ perovskite pseudocapacitor electrodes. *Nature Materials*, 13(7):726–732, 2014.

[3] S. K. Nesdal. Development of hexagonal manganites for use in oxygen permeable membranes. Master's thesis, NTNU, 2013.

[4] M. M. Frydenlund. Development of a new class of oxygen ion mixed conductors. Master's thesis, NTNU, 2014.

[5] M. Reidulff. Phase stability and point defects in $InMnO_3$. Master's thesis, NTNU, 2014.

[6] K. Thorbjørnsen. Electrochemical characterization of $YMnO_3$. Specialization project, 2015.

[7] J-C. Grenier, M. Pouchard, and A. Wattiaux. Electrochemical synthesis: Oxygen intercalation. *Current Opinion in Solid State and Materials Science*, 1(2):233 – 240, 1996.

[8] B.E. Conway. *Electrochemical Supercapacitors: Scientific Fundamentals and Technological Applications*. Springer US, 1999.

[9] S. Wen, J-W. Lee, I-H. Yeo, J. Park, and S. Mho. The role of cations of the electrolyte for the pseudocapacitive behavior of metal oxide electrodes, MnO_2 and RuO_2. *Electrochimica Acta*, 50(2–3):849 – 855, 2004.

[10] T. Kudo, H. Obayashi, and T. Gejo. Electrochemical behavior of the perovskite-type $Nd_{1-x}Sr_xCoO_3$ in aqeous alkaline solution. *Journal of Electrochemical Society*, 122(2):159–163, 1975.

[11] J-C. Grenier, A. Wattiaux, N. Lagueyte, J.C. Park, E. Marquestaut, J. Etourneau, and M. Pouchard. A new superconductor obtained by electrochemical oxidation of La_2CuO_4. *Physica C: Superconductivity*, 173(3):139 – 144, 1991.

[12] Remsen S. and B. Dabrowski. Synthesis and oxygen storage capacities of hexagonal $Dy_{1-x}Y_xMnO_{3-\delta}$. *Chemistry of Materials*, 23(17):3818–3827, 2011.

[13] R. D. Shannon. Revised effective ionic radii and systematic studies of interatomic distances in halides and chalcogenides. *Acta Crystallographica Section A*, 32(5):751–767, Sep 1976.

[14] J. A. Alonso, M. J. Martinez-Lope, M. T. Casais, and M. T. Fernandez-Diaz. Evolution of the jahn-teller distortion of MnO_6 octahedra in $RMnO_3$ perovskites (R = Pr, Nd, Dy, Tb, Ho, Er, Y): A neutron diffraction study. *Inorganic Chemistry*, 39(5):917–923, 2000.

[15] C. J. Howard, B. J. Campbell, H. T. Stokes, M. A. Carpenter, and R. I. Thomson. Crystal and magnetic structures of hexagonal $YMnO_3$. *Acta Crystallographica Section B-Structural Science*, 69:534–540, 2013.

[16] K. Momma and F. Izumi. VESTA: for three-dimensional visualization of crystal, volumetric and morphology data. *Journal of Applied Crystallography*, 44(6):1272–1276, Dec 2011.

[17] M. Chen, B. Hallstedt, and L. J. Gauckler. Thermodynamic assessment of the Mn–Y–O system. *Journal of Alloys and Compounds*, 393(1–2):114–121, 2005.

[18] Diagrams that provide useful oxidation-reduction information. `https://www.wou.edu/las/physci/ch462/redox.htm`. [Accessed online 10.12.2015].

[19] E. S. Stampler, W. C. Sheets, W. Prellier, T. J. Marks, and K. R. Poeppelmeier. Hydrothermal synthesis of $LnMnO_3$ (Ln = Ho, Lu and Y): exploiting amphoterism in late rare-earth oxides. *J. Mater. Chem.*, 19:4375–4381, 2009.

[20] J. E. Medvedeva, V. I. Anisimov, M. A. Korotin, O. N. Mryasov, and A. J. Freeman. The effect of coulomb correlation and magnetic ordering on the electronic structure of two hexagonal phases of ferroelectromagnetic $YMnO_3$. *Journal of Physics-Condensed Matter*, 12(23):4947–4958, 2000.

[21] C. Moure, M. Villegas, J.F. Fernandez, J. Tartaj, and P. Duran. Phase transition and electrical conductivity in the system $YMnO_3$-$CaMnO_3$. *Journal of Materials Science*, 34(11):2565–2568, 1999.

[22] R. J. D. Tilley. *Understanding Solids: The Science of Materials*. Wiley, 2nd edition, 2013.

[23] B. B. Van Aken, J-W. G. Bos, R. A. de Groot, and T. T. M. Palstra. Asymmetry of electron and hole doping in $YMnO_3$. *Phys. Rev. B*, 63:125127, Mar 2001.

[24] M. C. Sekhar and N. V. Prasad. Dielectric, impedance, magnetic and magnetoelectric measurements on $YMnO_3$. *Ferroelectrics*, 345(1):45–57, 2006.

[25] M. M. Frydenlund. Electrical conductivity in hexagonal manganites. Specialization project, 2013.

[26] A.R. West. *Solid State Chemistry and its Applications*. Wiley, 2014.

[27] J.A.M. Van Roosmalen, E.H.P. Cordfunke, R.B. Helmholdt, and H.W. Zandbergen. The defect chemistry of $LaMnO_{3+\delta}$: 2. structural aspects of $LaMnO_{3+\delta}$. *Journal of Solid State Chemistry*, 110(1):100 – 105, 1994.

[28] E. R. Østli. Optimization of chemical composition of novel manganite oxides for oxygen permeable membranes. Master's thesis, NTNU, 2015.

[29] M. Tomczyk, A.M.O.R. Senos, I.M. Reaney, and P.M. Vilarinho. Reduction of microcracking in $YMnO_3$ ceramics by Ti substitution. *Scripta Materialia*, 67(5):427 – 430, 2012.

[30] T. Asaka, K. Nemoto, K. Kimoto, T. Arima, and Y. Matsui. Crystallographic superstructure of Ti-doped hexagonal $YMnO_3$. *Phys. Rev. B*, 71:014114, Jan 2005.

[31] B. P. Hahn, J. W. Long, and D. R. Rolison. Something from nothing: Enhancing electrochemical charge storage with cation vacancies. *Accounts of Chemical Research*, 46(5):1181–1191, 2013.

[32] S. H. Skjærvø, E. T. Wefring, S. K. Nesdal, G. H. Olsen, T. Tybell, and S. M. Selbach. Interstitial oxygen as a source of p-type conductivity in hexagonal manganites. *Subm. to Nature Commun. 29.10.2015*, 2015.

[33] A. Nemudry, E.L. Goldberg, M. Aguirre, and M.Á. Alario-Franco. Electrochemical topotactic oxidation of nonstoichiometric perovskites at ambient temperature. *Solid State Sciences*, 4(5):677 – 690, 2002.

[34] M. Hibino, T. Kimura, Y. Suga, T. Kudo, and N. Mizuno. Oxygen rocking aqueous batteries utilizing reversible topotactic oxygen insertion/extraction in iron-based perovskite oxides $Ca_{1-x}Cu_xFeO_{3-\delta}$. *Scientific Reports*, 2(601):601, 2012.

[35] J. T. Mefford, W. G. Hardin, S. Dai, K. P. Johnston, and K. J. Stevenson. Anion charge storage through oxygen intercalation in $LaMnO_3$ perovskite pseudocapacitor electrodes: Supplementary informaton. *Nature Materials*, 13(7):726–732, 2014.

[36] M. Hibino, T. Kimura, Y. Suga, T. Kudo, and N. Mizuno. Oxygen rocking aqueous batteries utilizing reversible topotactic oxygen insertion/extraction in iron-based perovskite oxides $Ca_{1-x}Cu_xFeO_{3-\delta}$: Supplementary information. *Scientific Reports*, 2(601):601, 2012.

[37] C.H. Hamann, A. Hamnett, and W. Vielstich. *Electrochemistry*. Wiley, 2007.

[38] X Wang, J. S. Lee, Zhu Q., Liu J., Wang Y., and Dai S. Ammonia-treated ordered mesoporous carbons as catalytic materials for oxygen reduction reaction. *Chemistry of Materials*, 22(7):2178–2180, 2010.

[39] V. Budarin, J. H. Clark, R. Luque, and R. White. Starbons™: Cooking up nanostructured mesoporous materials. *Material Matters*, 4(1):19–22, 2009.

[40] K. B. Oldman, J. C. Myland, and Bond A. M. *Electrochemical Science and Technology*. Wiley, 2002.

[41] J Wang, J. Polleux, J Lim, and B Dunn. Pseudocapacitive contributions to electrochemical energy storage in TiO_2 (anatase) nanoparticles. *The Journal of Physical Chemistry C*, 111(40):14925–14931, 2007.

[42] Sigma Aldrich. Carbon, mesoporous. `http://www.sigmaaldrich.com/catalog/product/aldrich/702102?lang=en&region=NO`, 2016. [Online; accessed 29-May-2016].

[43] Sigma Aldrich. Carbon, mesoporous. `http://www.sigmaaldrich.com/catalog/product/aldrich/702110?lang=en&region=NO`, 2016. [Online; accessed 29-May-2016].

[44] S. M. Hoggen. Development of oxygen-permeable membranes based on hexagonal manganites. Specialization project, 2015.

[45] Bruker Corporation. DIFFRAC.SUITE TOPAS 5. Software.

[46] A. S. Gibbs, K. S. Knight, and P. Lightfoot. High-temperature phase transitions of hexagonal $YMnO_3$. *Physical Review B*, 83(9):094111, 2011.

[47] Gamry Instruments. Gamry framework. Software.

[48] EDAX. Interactive periodic table of elements. `http://www.edax.com/periodic-table/index.aspx`, 2016. [Online; accessed 10-June-2016].

[49] E. Bjartnes. Oxygen evolution on $La_{1-x}Sr_xCoO_3$ pellet electrodes in alkaline solution. Master's thesis, NTNU, 2012.

[50] K. B. Oldman, J. C. Myland, and A. M. Bond. Web 1331. `http://bcs.wiley.com/he-bcs/Books?action=mininav&bcsId=7004&itemId=`

0470710845&assetId=270618&resourceId=26691&newwindow=true, 2016. [Online; accessed 29-May-2016].

[51] Western Oregon University. Pourbaix diagrams. http://www.wou.edu/las/physci/ch412/pourbaix.htm, 2016. [Online; accessed 01-June-2016].

Appendix A

Troubleshooting

In order to ensure that all the electrochemical equipment was functioning, it was attempted to record a voltammogram of a Pt(s) rotating disc electrode in 1 M KOH with a Pt(s) counter electrode and a Ag/AgCl reference electrode (Radiometer REF201). This was not entirely successfull. The results were dominated by semi-periodic noise of high amplitude, and the equipment had to be checked. The initial recorded voltammogram of Pt are shown in Figure A.1. The noise was in mA. When the y-axis was restricted to µA, the characteristic voltammogram for Pt in KOH was visible.

The potentiostat was then calibrated with a dummy-cell, but this did not give a different result. Neither did using a different potentiostat or polishing of all the electrical contacts. It was attempted to use 4 other Ag/AgCl-electrodes of the same type (REF201), but the noise in the measurements did not decrease.

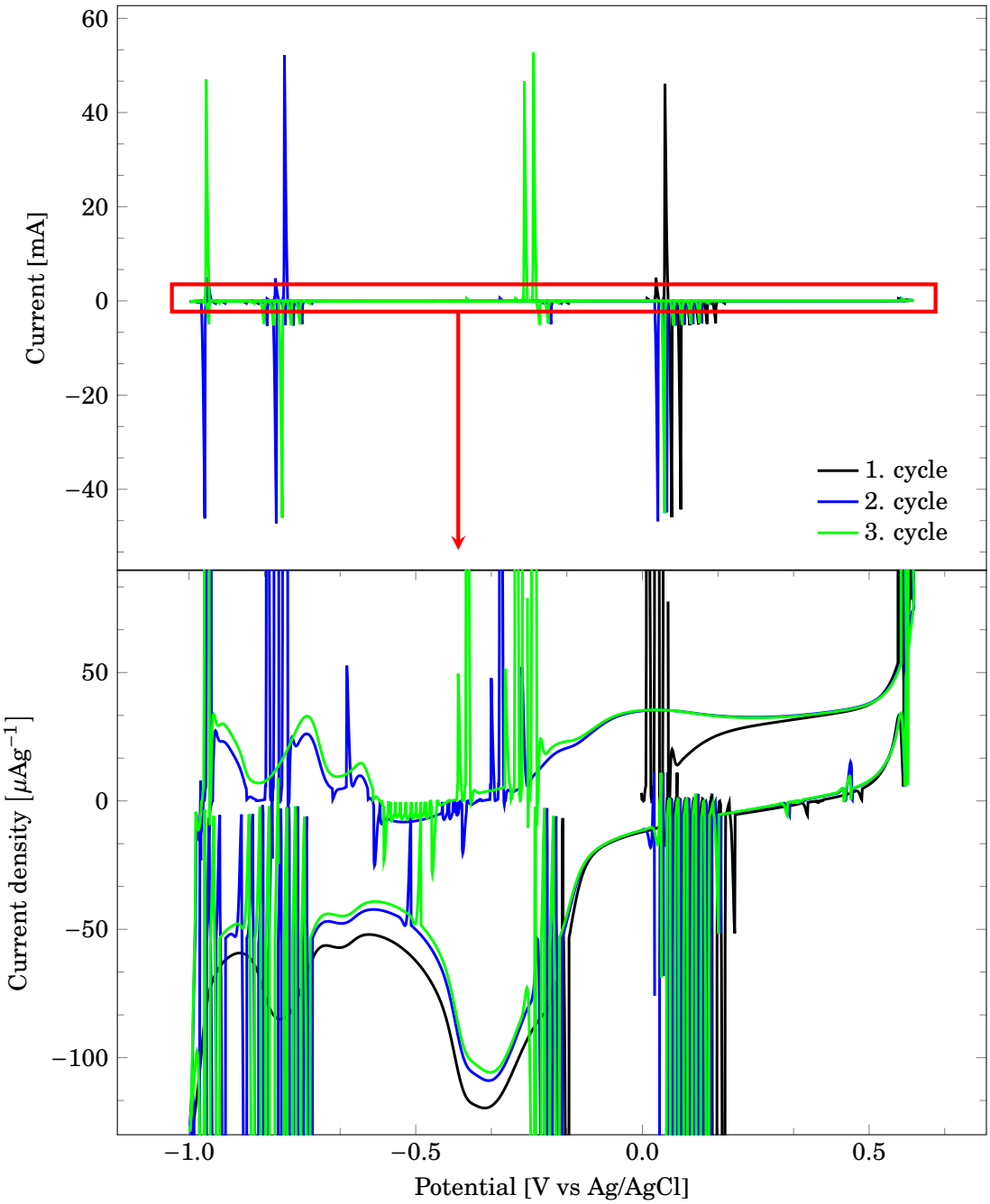

Figure A.1: The initial voltammogram recorded of Pt in 1M KOH at 100 mV s^{-1}. The noise was in mA. When the y-axis was restricted to µA, the characteristic voltammogram for Pt in KOH was visible.

The open circuit voltage of the Ag/AgCl-Pt-Pt in 1 M KOH system was measured for 300s, as shown in Figure A.2. The noise in the graph indicates when the laborettes moved inside the room.

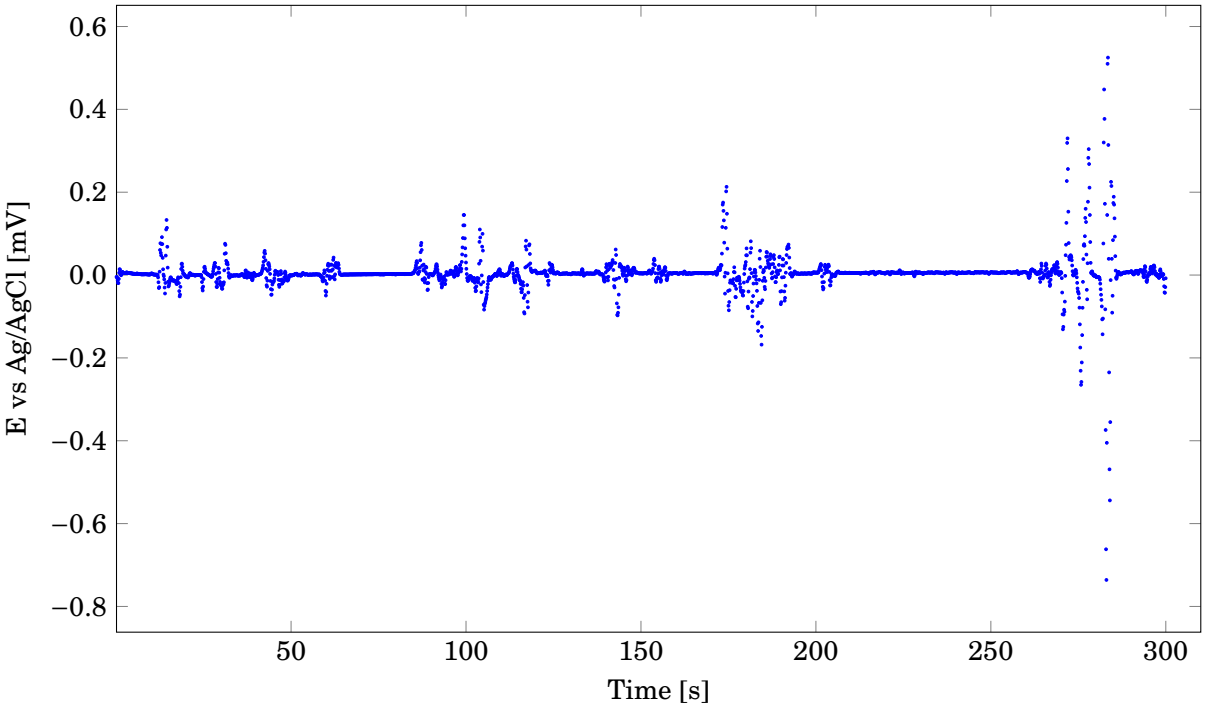

Figure A.2: Open circuit potential of the Ag/AgCl-Pt-Pt system in 1M KOH for 300s. The noise indicates when the laborettes made the slightest movement.

Due to the unsuccessful attempts to change the reference electrode, it was suspected that the platina RDE was broken. The electrode was changed, a reversible hydrogen electrode was used as a reference electrode and the electrolyte was changed to 0.5M H_2SO_4. The measurements was then stable and predictable. In order to check if the original Pt-working electrode was indeed broken, a voltammogram was recorded for both the original and a new Pt-RDE. The resulting voltammograms are shown in Figure A.3.

When the reference electrode was changed from RHE to Ag/AgCl, a voltammogram could not be recorded. The corresponding potential-time graphs are shown in Figure A.4

Due to the apparent faulty Ag/AgCl reference electrode, it was attempted to create a hydrogen electrode with KOH as the electrode filling. The open circuit potential of this electrode was measured against a RHE in 0.5M H_2SO_4, and is shown in Figure A.5. The potential was as expected unstable, so the electrode could not be used.

The saturated KCl-solution in the original Ag/AgCl electrode from Figure A.1 was replaced. This lead to the successful recording a voltammogram of Pt in 1 M KOH, as shown in Figure 4.5.

The equipment was deemed as functioning and the characterization of $YMn_{1-x}Ti_xO_{3\pm\delta}$ could begin.

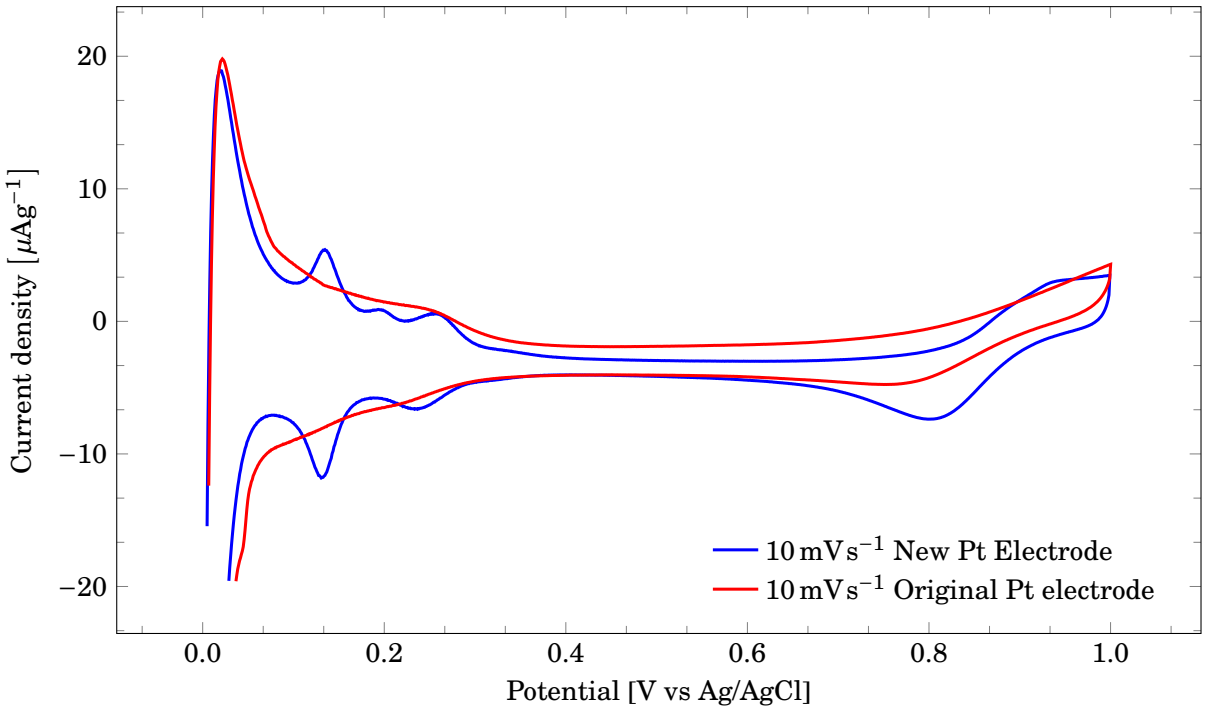

Figure A.3: Voltammogram of two different Pt-RDE in 0.5 M H_2SO_4

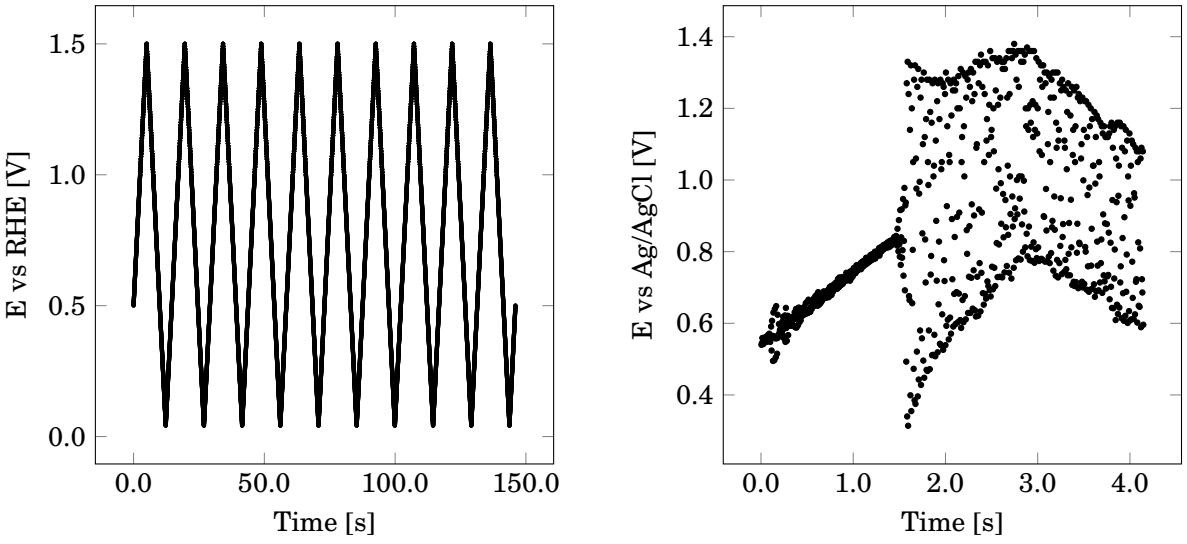

(a) RHE electrode

(b) Ag/AgCl electrode

Figure A.4: Potential-time graph when it was attempted to cycle the potential between 0 V and 1.5 V.

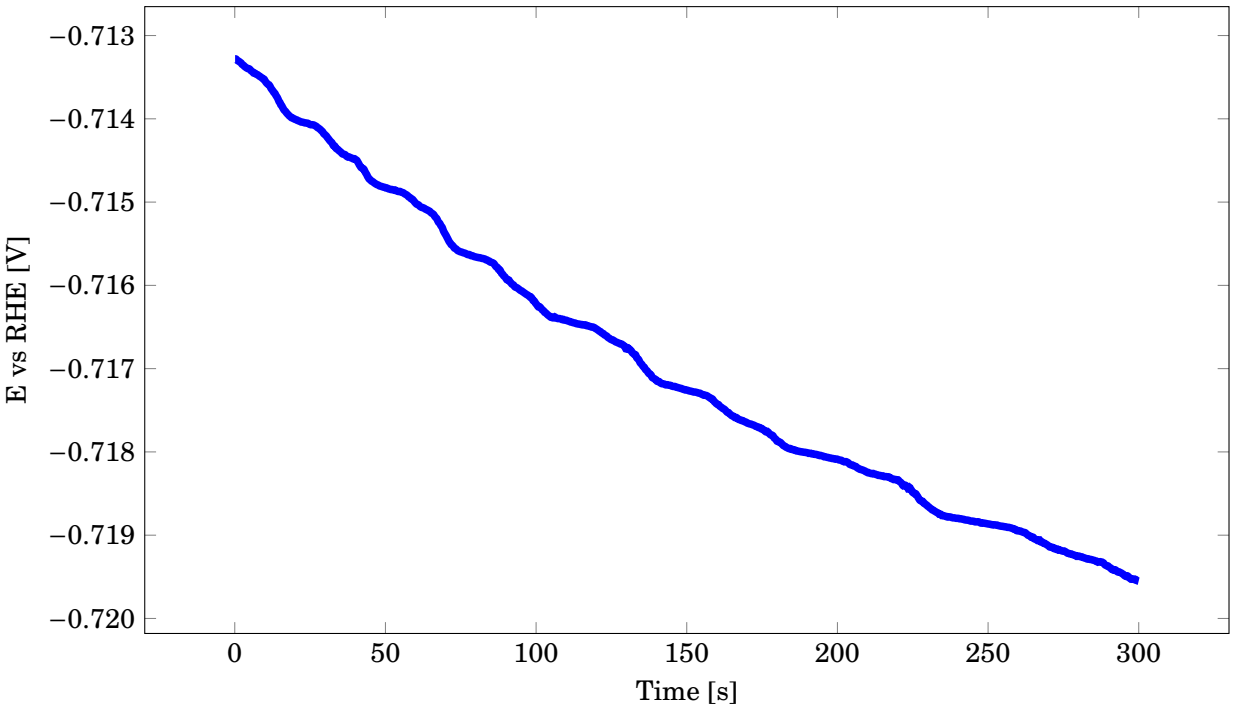

Figure A.5: Open circuit potential of a reversible hydrogen electrode with 1M KOH as the electrode filling, recorded in 0.5M H_2SO_4. The potential was not stable.

Appendix B

Development of electrode setup

B.1 Hot pressed composite electrode

A hot pressed composite disc of $YMn_{1-x}Ti_xO_{3\pm\delta}$ and mesoporous carbon could have been adhered to the glassy carbon electrode surface by e.g. carbon tape. The disc could then have been removed without damaging the surface, which would have made further analysis after electrochemical characterization possible. It was attempted to hot press a mixture of 30wt% $YMnO_3$ and 70wt% mesoporous carbon at various temperatures and loads as in table B.1, but none resulted in densification. It was used a custom die, which consisted of a thin bottom plate for heat transfer, a cylinder and a piston, all in stainless steel. The diameter of the piston and the cylinder hole was 1cm. The hot press could not reach a higher temperature, and a higher load would most likely damage the equipment. After attempt number 6, the piston was stuck inside the die. The reason for why a high temperature hot press was not used was simply that it was not available.

Table B.1: Table of the parameters adjusted in the hot-pressing.

#	1	2	3	4	5	6[(a)]
T [°C]	150	150	150	175	175	175
P [MPa]	4	4	125	125	125	125
t [min]	15	30	30	30	60	60

B.2 Using carbon tape for adhesion

It was attempted to use a piece of conducting carbon tape to adhere a sintered disc, as synthesized in Section 3.2, to the glassy carbon electrode. When in air, this method appeared very promising. The disc was strongly adhered to the carbon tape, and the tape was easy to remove from the glassy carbon surface. However, when the electrode was lowered into the electrolyte, the disc would always fall off. After a few minutes, the carbon tape was strongly adhered to the glassy carbon surface. Removal of the carbon tape involved the risk of damaging the glassy carbon surface. Also, large amounts of leftover glue had to be polished off from the glassy carbon surface. This method was not further explored. Not only due to the carbon tape's inability to be used in the alkaline electrolyte, but also due to the risk of damaging the electrode

[(a)] 100% Bulk $YMnO_3$

surface. It was also attempted to deposit particles directly onto the carbon tape, but the tape would have had to be removed from the GCRDE here as well.

Appendix C

Separation of faradic and non-faradic currents: Derivaton of the equation

By using the definition that the measured current is the sum of faradic and non-faradic components, as in Equation (C.1), where v is the sweep rate in $\mathrm{mV\,s^{-1}}$.

$$I_{meas} = I_{nf} + I_f = \beta v + \alpha\sqrt{v} \tag{C.1}$$

and defining Equations (C.2) and (C.3):[50]

$$\alpha = \frac{I_f}{\sqrt{v}} \tag{C.2}$$

$$\beta = \frac{I_{nf}}{v} \tag{C.3}$$

the ratio between non-faradic and faradic currents can be established in Equations (C.4) to (C.6).

$$\frac{I_{nf}}{I_f} = \frac{\beta v}{\alpha\sqrt{v}} \tag{C.4}$$

$$= \frac{\beta}{\alpha}\sqrt{v} \tag{C.5}$$

$$= K \tag{C.6}$$

The non-faraduc current can then be set equal to Equation (C.7).

$$I_{nf} = I_f K \tag{C.7}$$

Combining with $I_{meas} = I_f + I_{nf}$ gives Equation (C.9).

$$I_{nf} = \left(I_{meas} - I_{nf}\right)K \tag{C.8}$$

$$I_{nf} = I_{meas}\left(\frac{K}{1+K}\right) \tag{C.9}$$

And consequently Equation (C.12).

$$I_f = I_{meas} - I_{nf} \tag{C.10}$$

$$I_f = I_{meas} - I_{meas}\left(\frac{K}{1+K}\right) \tag{C.11}$$

$$I_f = I_{meas}\left(1 - \left(\frac{K}{1+K}\right)\right) \tag{C.12}$$

Appendix D

Voltammograms

The faradic and non-faradic voltammograms not presented in Chapter 4 are presented in the following sections.

D.1 Unsupported particles on the GCRDE

Due to the absolute lack of adhesive properties and low amount of collected data of bulk $YTi_{0.12}Mn_{0.88}O_{3\pm\delta}$ on the glassy carbon RDE, it was not processed further. However, the nanocrystalline $YTi_{0.15}Mn_{0.85}O_{3\pm\delta}$ was processable, and the separated currents are given i Figures D.1 to D.3.

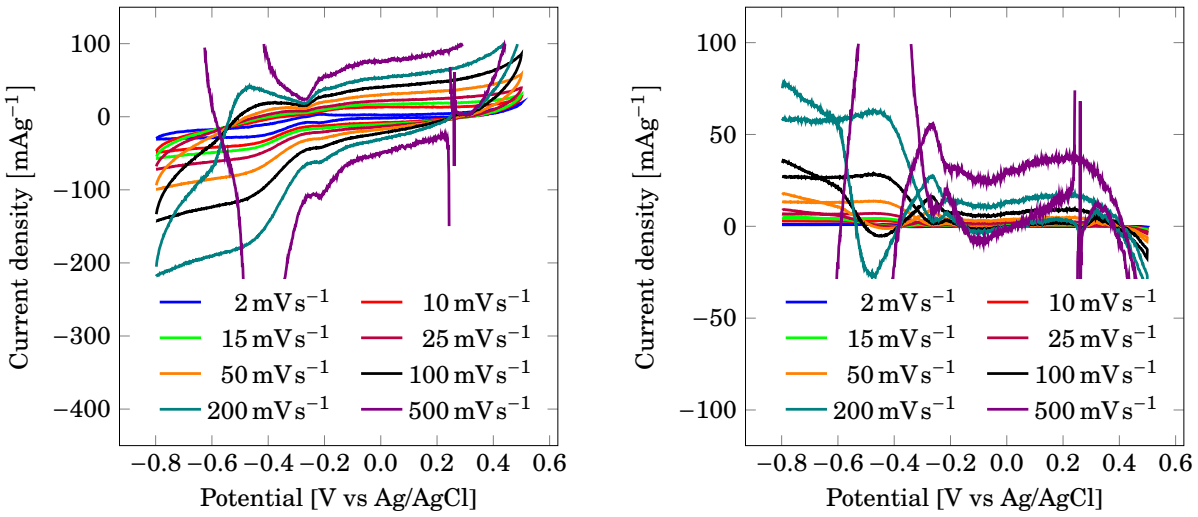

Figure D.1: The separated faradic (**a**) and non-faradic (**b**) current contributions from Figure 4.7 parallel 1

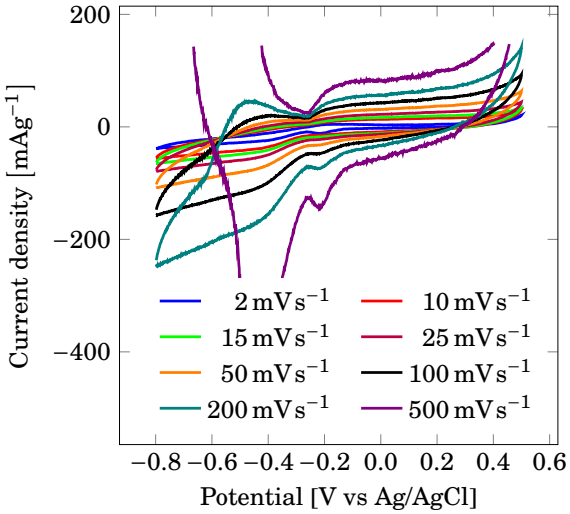

(a) Faradic current envelope of Figure 4.9.

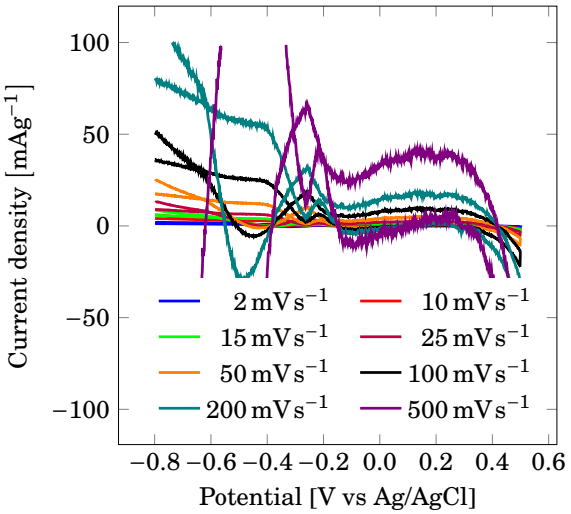

(b) Faradic current envelope of Figure 4.9.

Figure D.2: The separated faradic (**a**) and non-faradic (**b**) current contributions from Figure 4.7 parallel 2

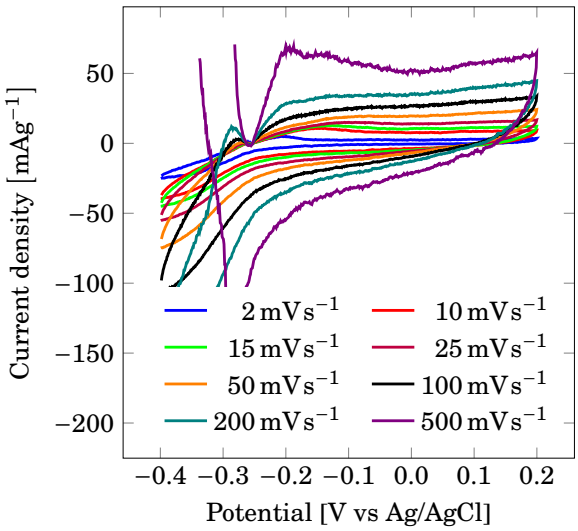

(a) Faradic current envelope of Figure 4.9.

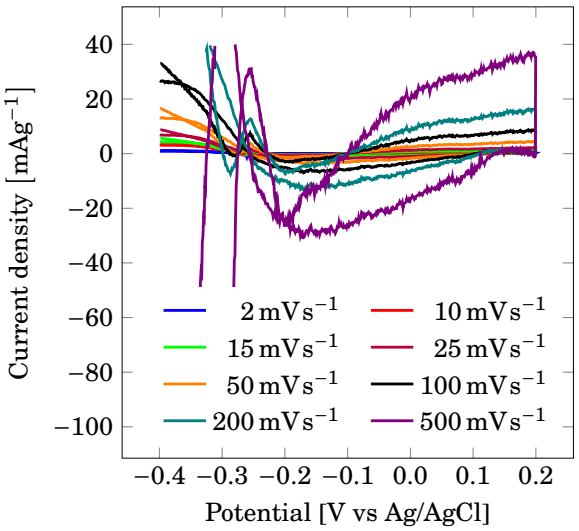

(b) Faradic current envelope of Figure 4.9.

Figure D.3: The separated faradic (**a**) and non-faradic (**b**) current contributions from Figure 4.8

D.2 Bulk $YTi_{0.12}Mn_{0.88}O_{3\pm\delta}$ on GC rod

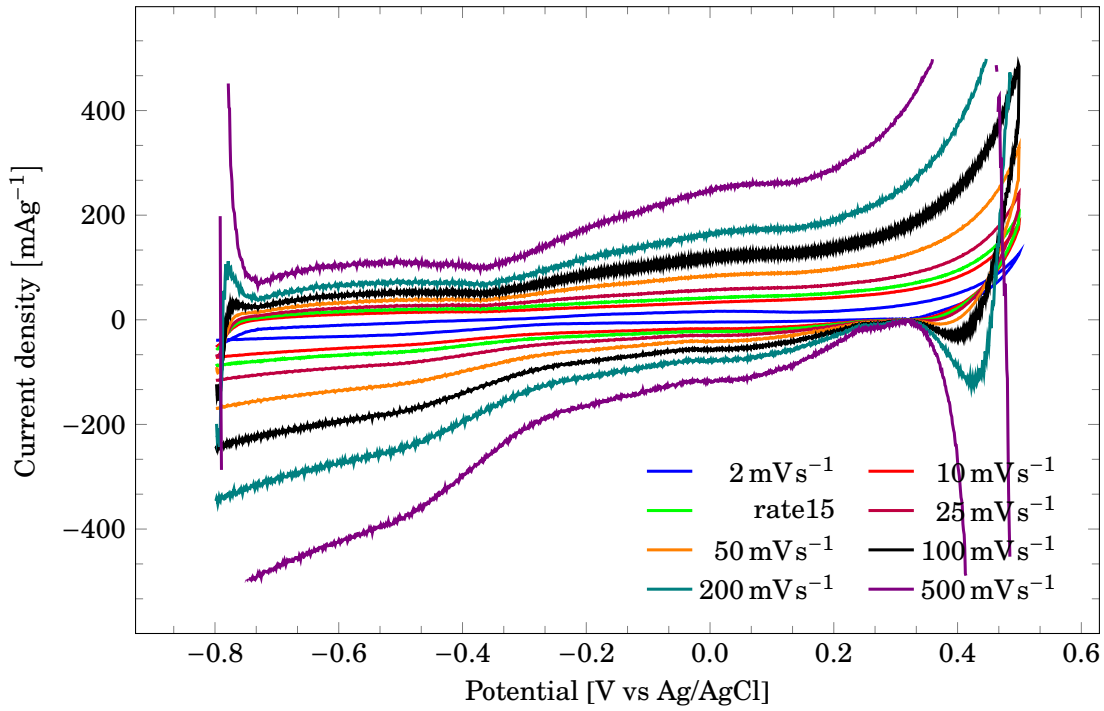

Figure D.4: The non-faradic current extracted from Figure 4.29

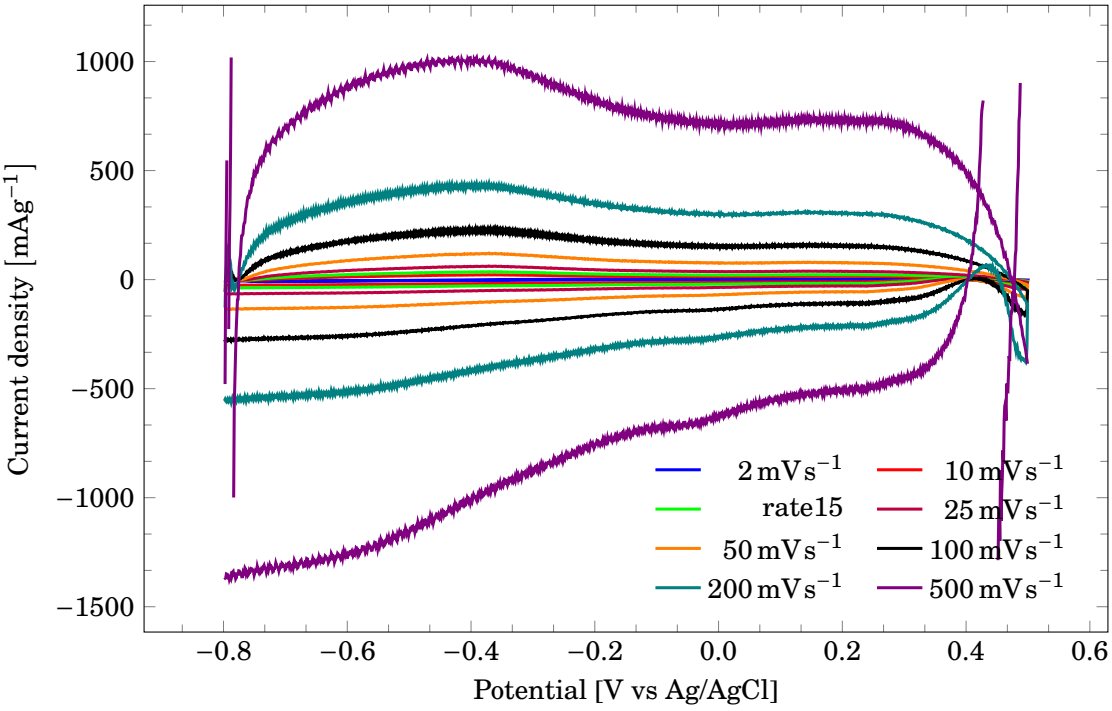

Figure D.5: The non-faradic current extracted from Figure 4.29

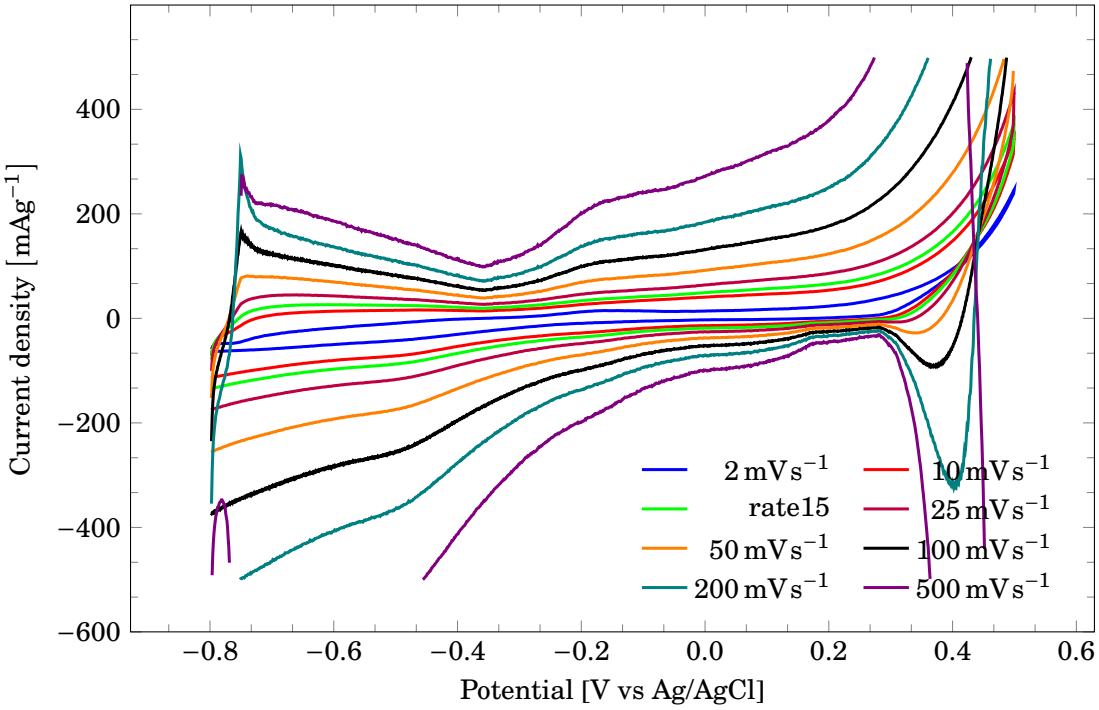

Figure D.6: The non-faradic current extracted from Figure 4.29

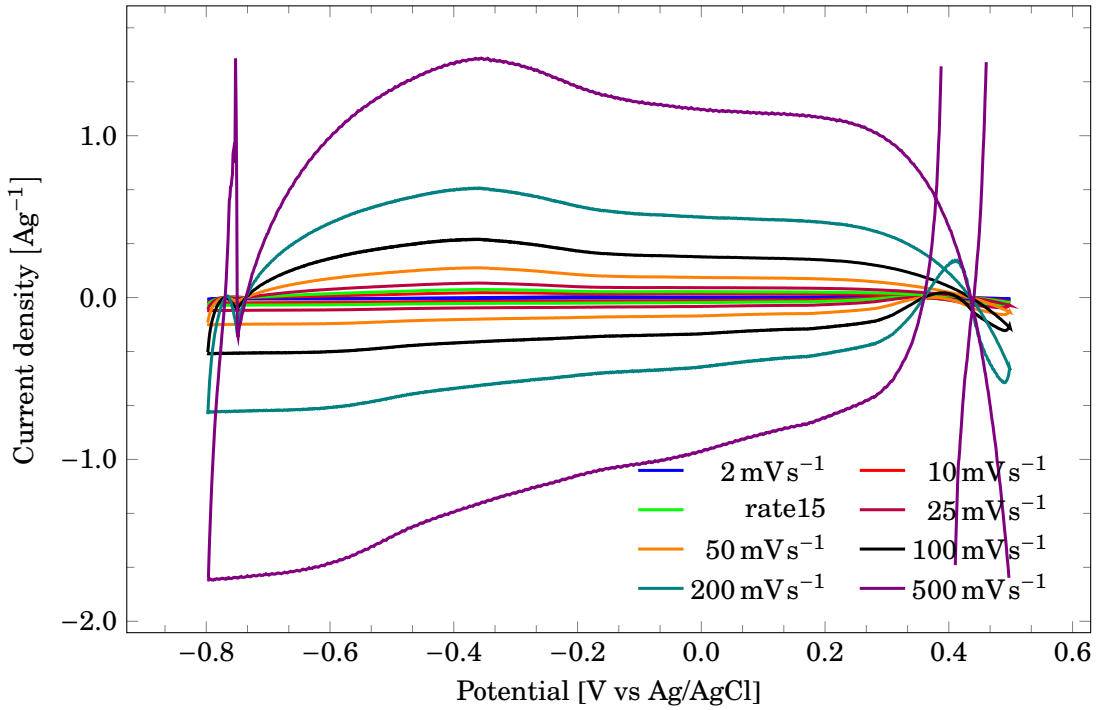

Figure D.7: The non-faradic current extracted from Figure 4.29

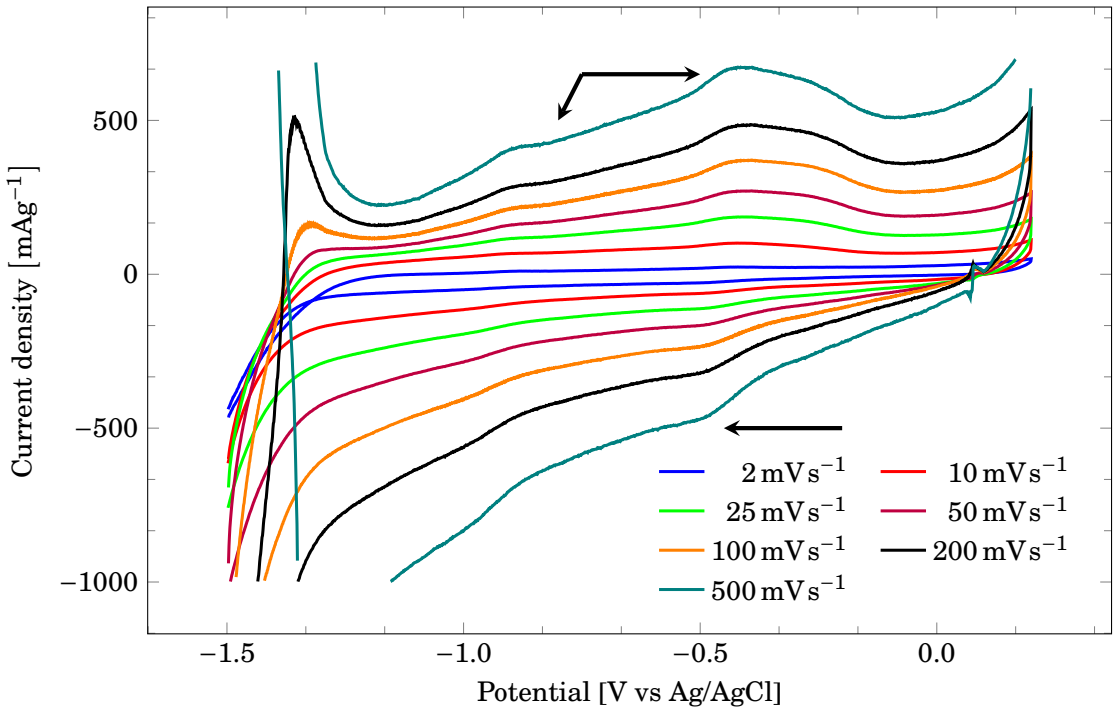

Figure D.8: The faradic current extracted from Figure 4.28

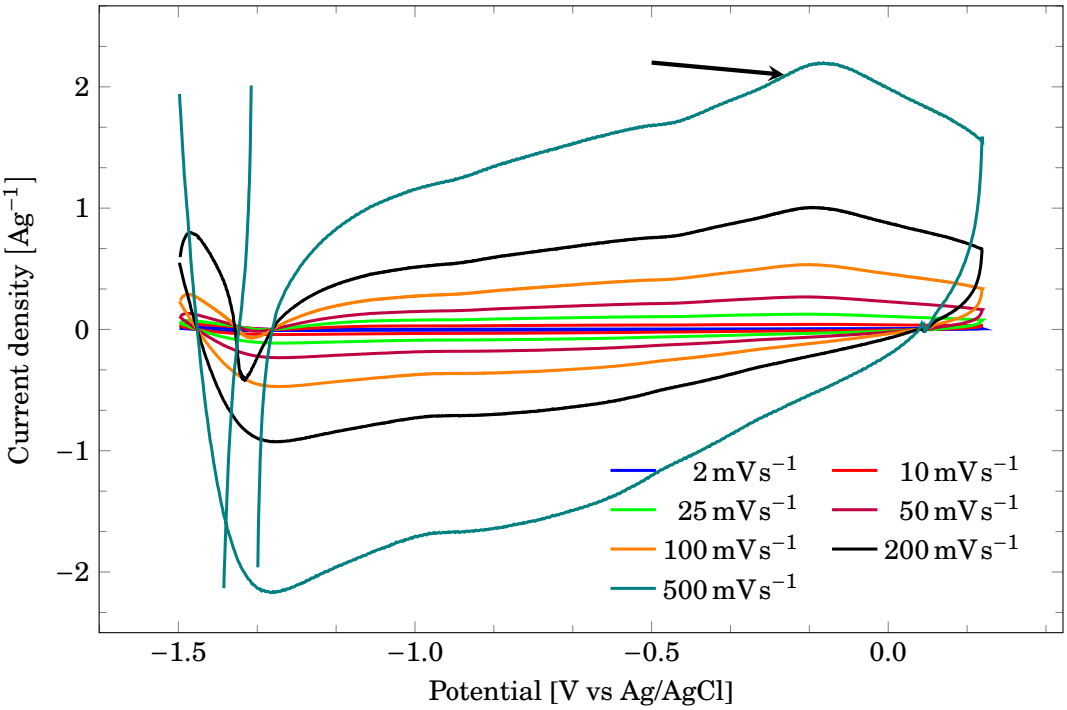

Figure D.9: The non-faradic current extracted from Figure 4.28

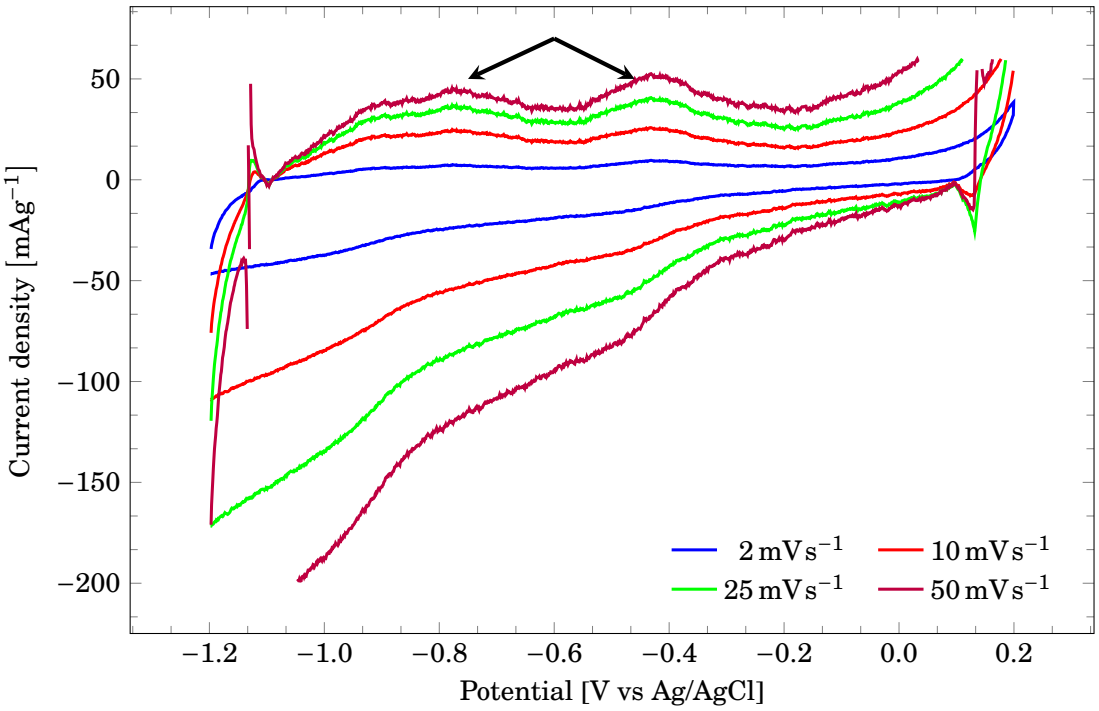

Figure D.10: The faradic current extracted from Figure 4.29

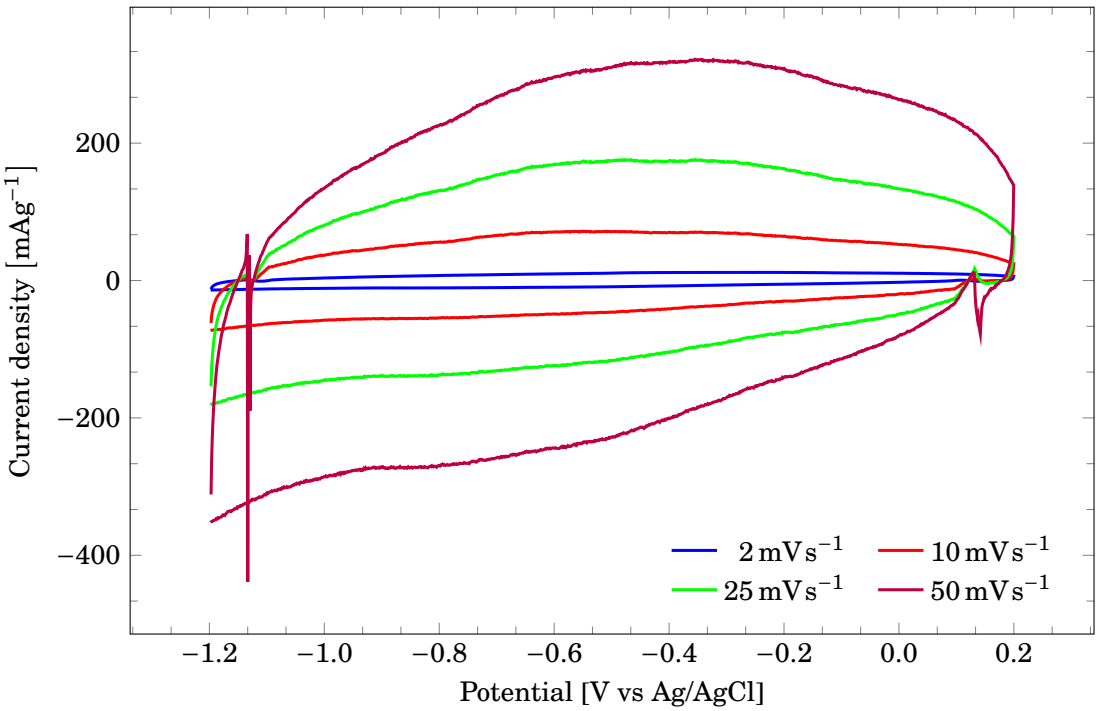

Figure D.11: The non-faradic current extracted from Figure 4.29

D.3 Glassy carbon rod

The CV curves of the GC rod in both O_2(g) saturated and N_2(g) purged 3 M KOH are given in Figures D.12 and D.13

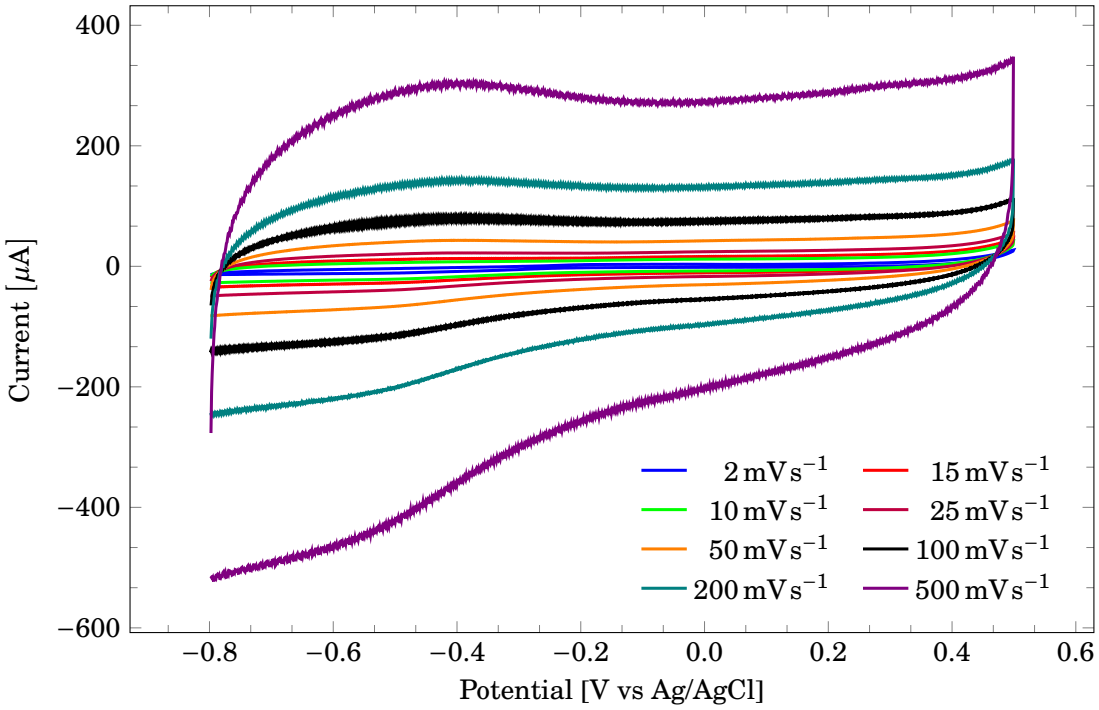

Figure D.12: Rod in N_2(g) purged 3 M KOH

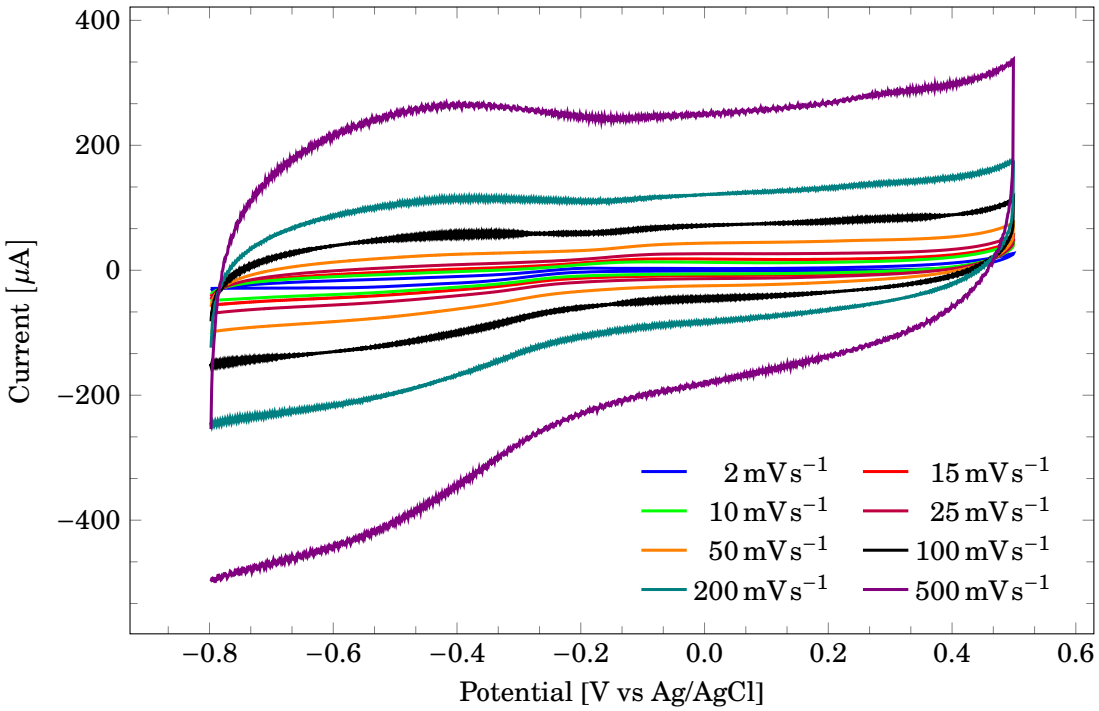

Figure D.13: Rod in O_2(g) saturated 3 M KOH

D.4 Nano $YTi_{0.15}Mn_{0.85}O_{3\pm\delta}$ on GC rod

Faradic and non-faradic separation of Figure 4.32 gives the faradic signal presented in Figure D.14. The diverging points are a results from the algorithm failing when I=0 for many sweep rates, and the linear regression gives a very low value of α or β.

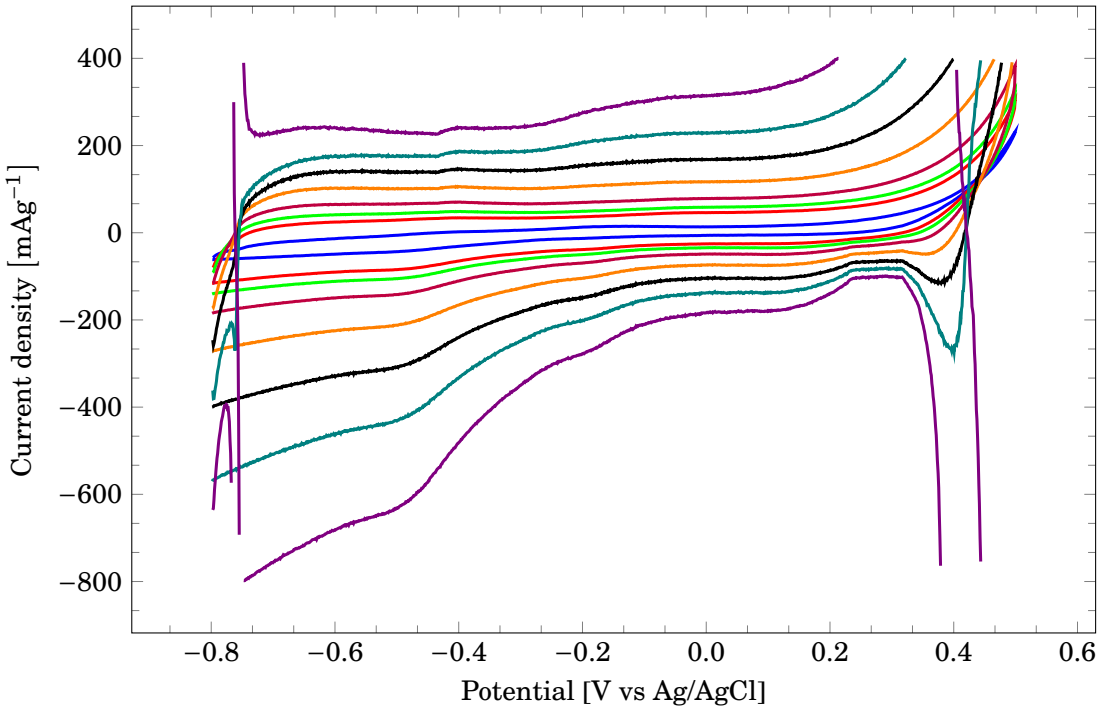

Figure D.14: Faradic currents of nanocrystalline $YTi_{0.15}Mn_{0.85}O_{3\pm\delta}$ deposited on the GC rod, scanned in N_2(g) purged 3 M KOH.

D.5 Nafion™ in O_2(g) saturated electrolyte

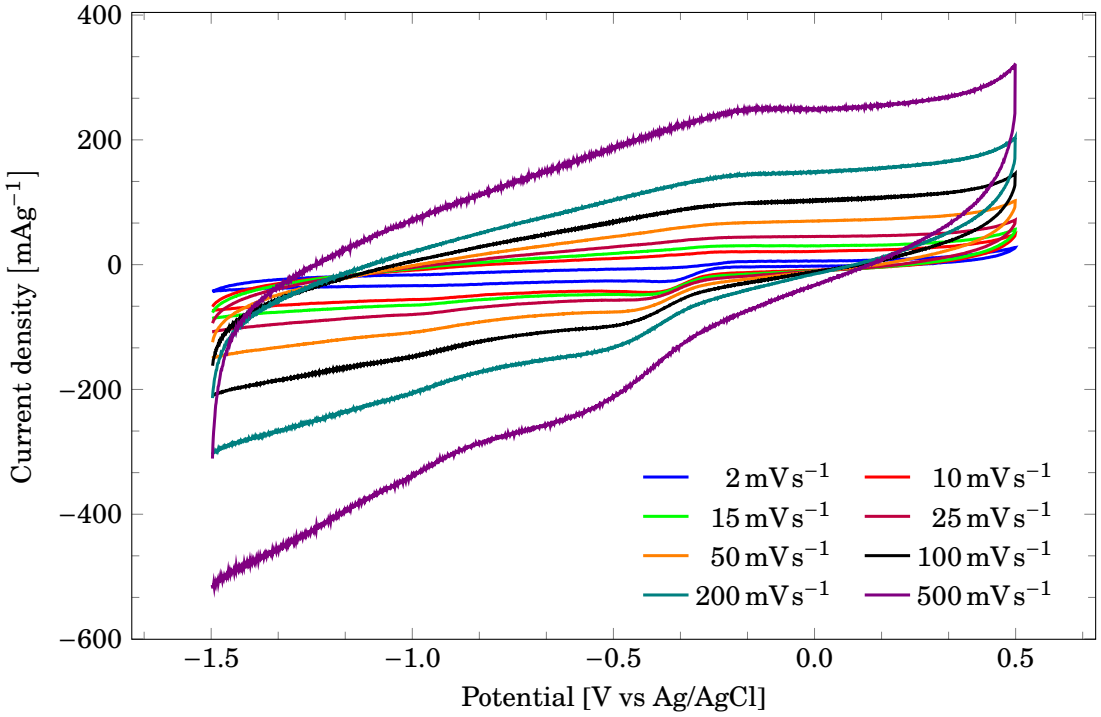

Figure D.15: Cyclic voltammogram of bulk $YTi_{0.12}Mn_{0.88}O_{3\pm\delta}$ deposited on a glassy carbon RDE, with a mass loading of 1 mg cm^{-2}. The deposition was made from a suspension of 0.05wt% Nafion™ in ethanol, with bulk $YTi_{0.12}Mn_{0.88}O_{3\pm\delta}$ suspended at 20 mg mL^{-1}. N_2(g) purged 3 M KOH was used as the electrolyte.

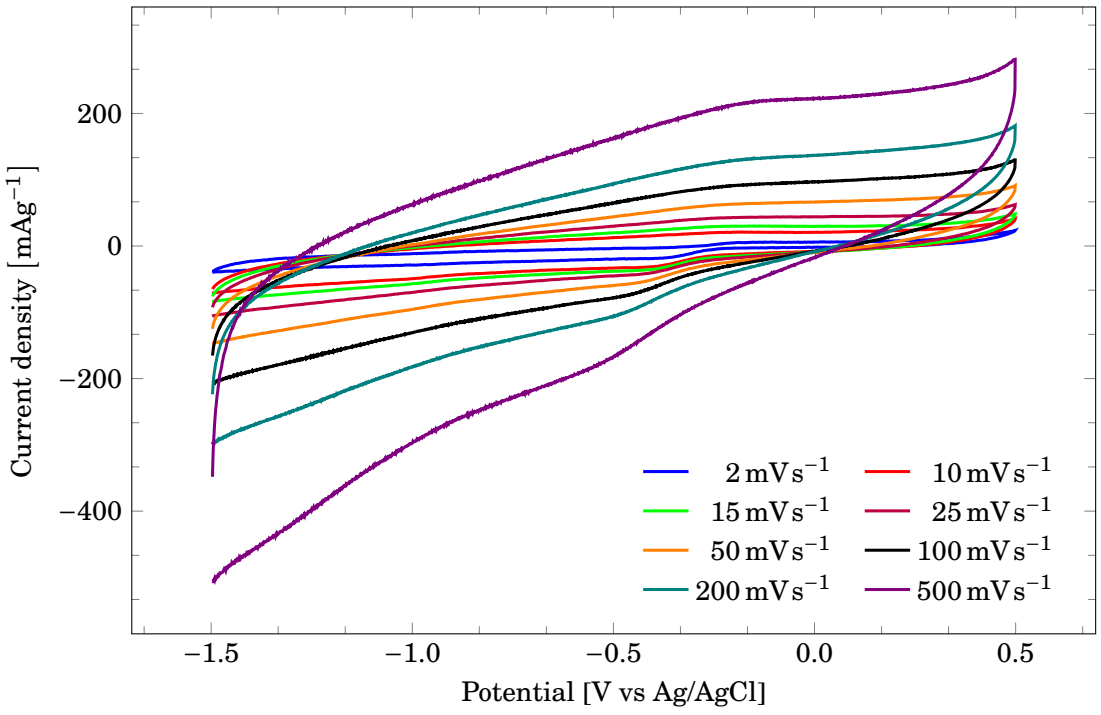

Figure D.16: Cyclic voltammogram of bulk $YTi_{0.12}Mn_{0.88}O_{3\pm\delta}$ deposited on a glassy carbon RDE, with a mass loading of 1 mg cm^{-2}. The deposition was made from a suspension of 0.025wt% Nafion™ in ethanol, with bulk $YTi_{0.12}Mn_{0.88}O_{3\pm\delta}$ suspended at 20 mg mL^{-1}. 3 M KOH was used as the electrolyte, both oxygen saturated and N_2(g) purged.

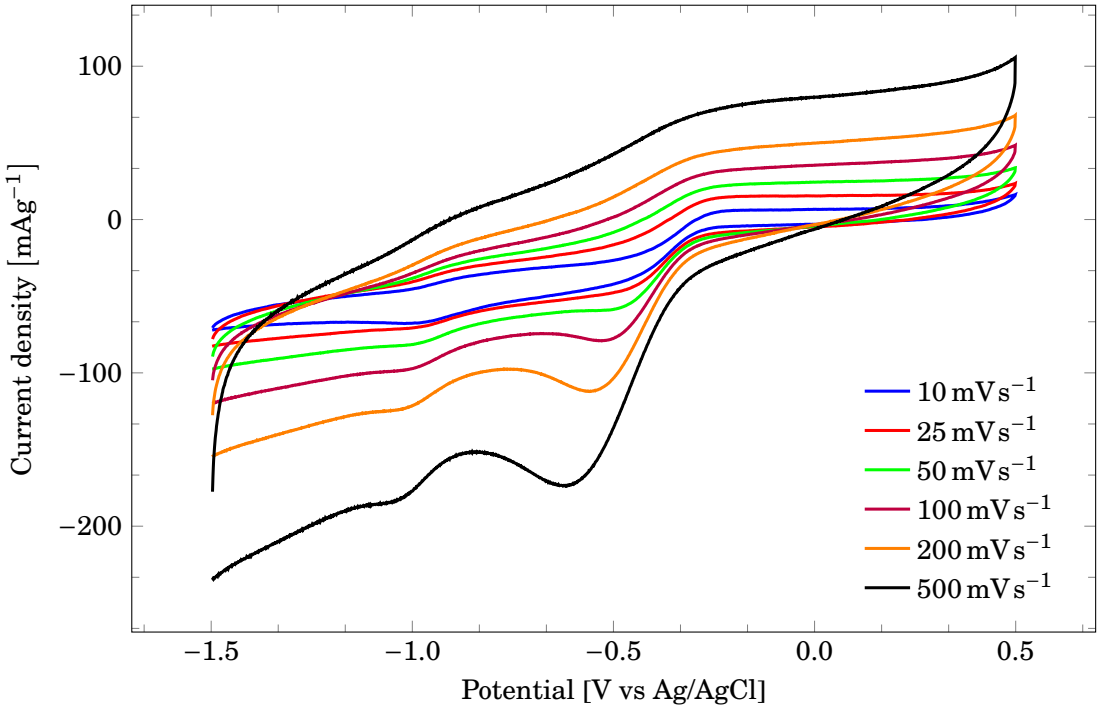

Figure D.17: Cyclic voltammogram of bulk $YTi_{0.12}Mn_{0.88}O_{3\pm\delta}$ deposited on a glassy carbon RDE, with a mass loading of 1 mg cm^{-2}. The deposition was made from a suspension of 0.1wt% Nafion™ in ethanol, with bulk $YTi_{0.12}Mn_{0.88}O_{3\pm\delta}$ suspended at 50 mg mL^{-1}. 3 M KOH was used as the electrolyte, both oxygen saturated and N_2(g) purged.

D.6 Nanocrystalline $YMnO_3$ on the GC rod

The zoomed-in area of Figure 4.35 are given in Figure D.18.

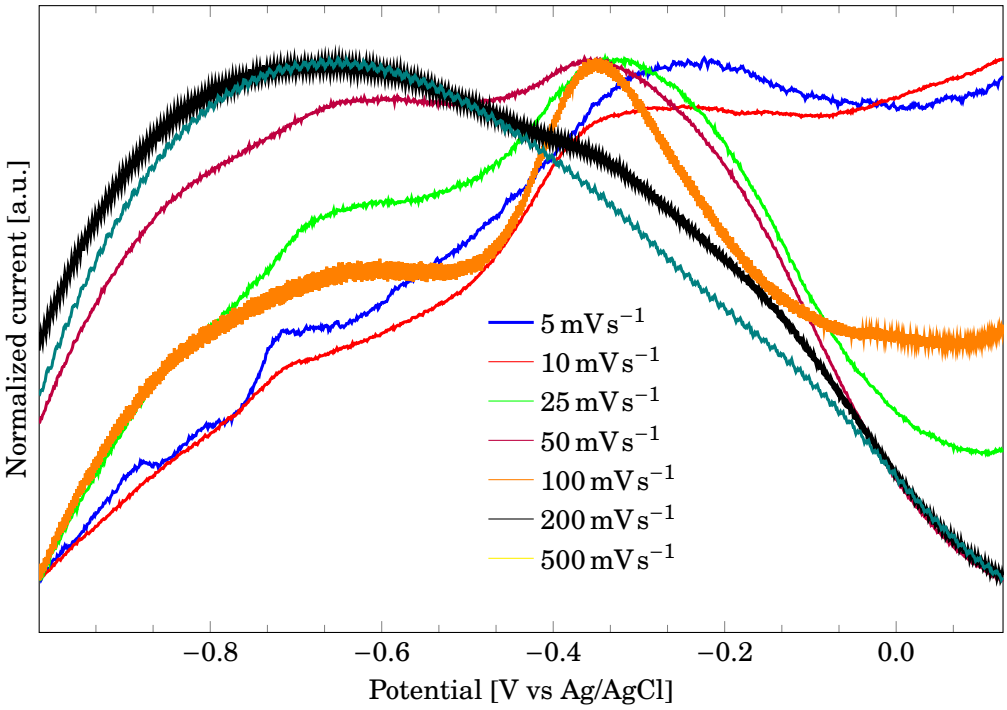

Figure D.18: A zoom-in of the peaks present in the CV curves for $YMnO_3$ on MC ST8 on the GC rod. The current has arbitrary units in order to see all the peaks at once.

D.7 Fractured disc in flat specimen electrode

Small air bubbles could be seen coming out from the fracture in the disc. Further voltammograms had a different shape than fig. 4.38a, as shown in Figure D.19. The peak current increased over time. The steel backing plate showed at brown-red colour when the electrode was dismounted. The cycles show peaks in the area between -1 and -0.5V. Both the peak position and discolouring correspond well with the formation of ferrous hydroxide[51].

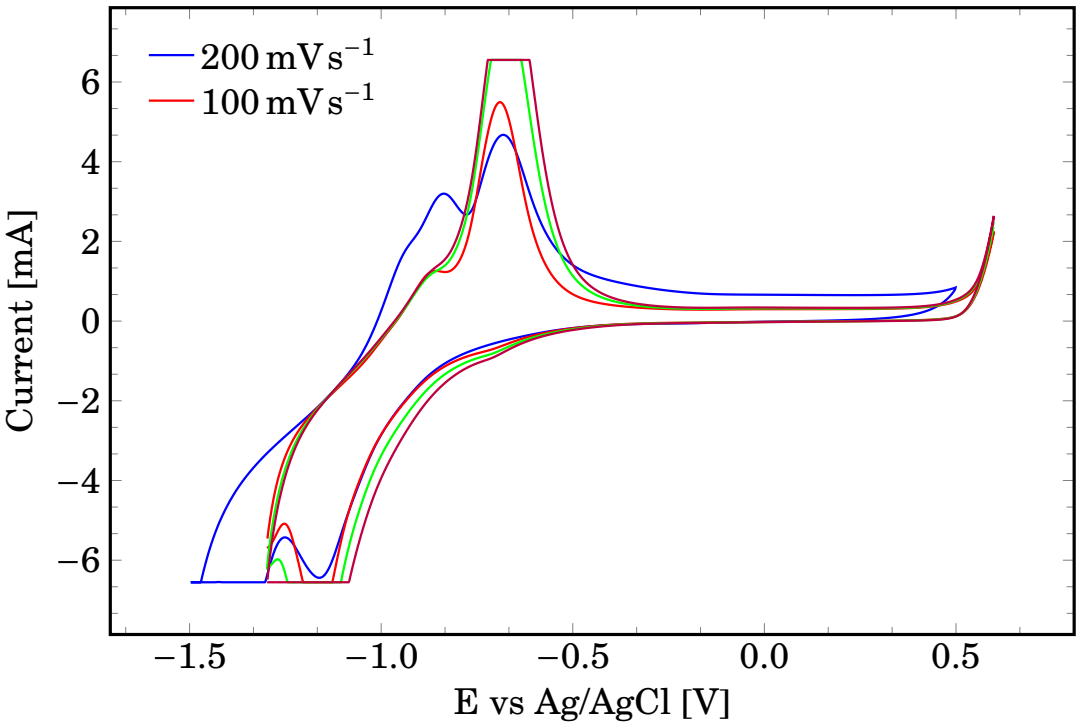

Figure D.19: Further cycles after the one performed in Figure 4.38a resulted in a different voltammogram, with clear oxidation peaks. The peaks most likely correspond to oxidation of the steel backing plate.

Appendix E

X-ray diffractograms

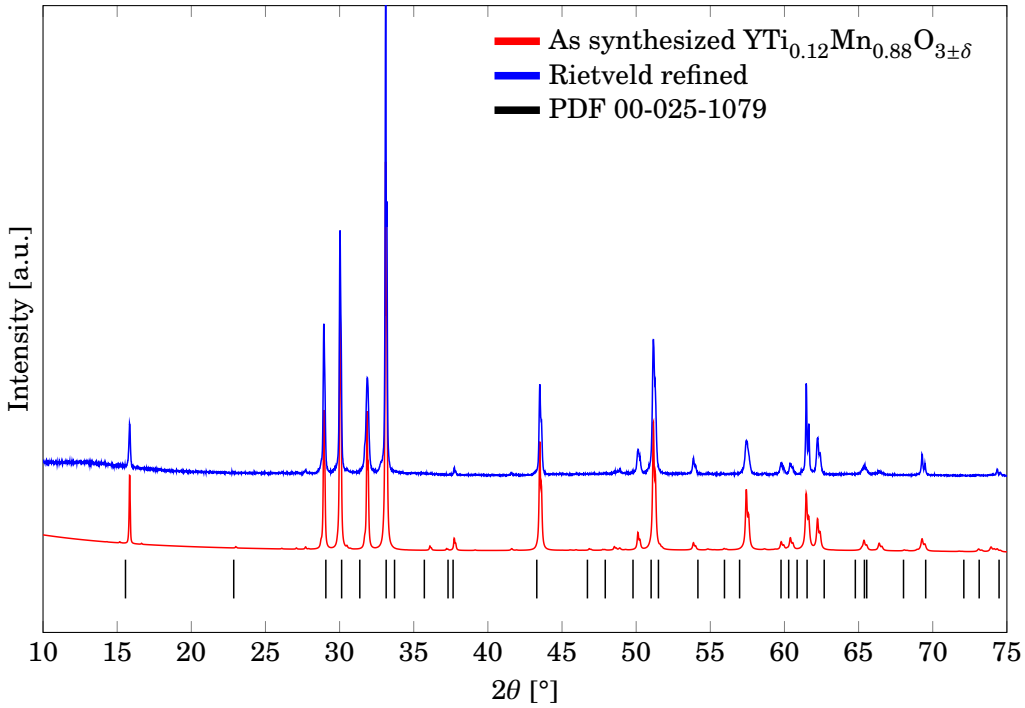

Figure E.1: Bulk $YTi_{0.12}Mn_{0.88}O_{3\pm\delta}$

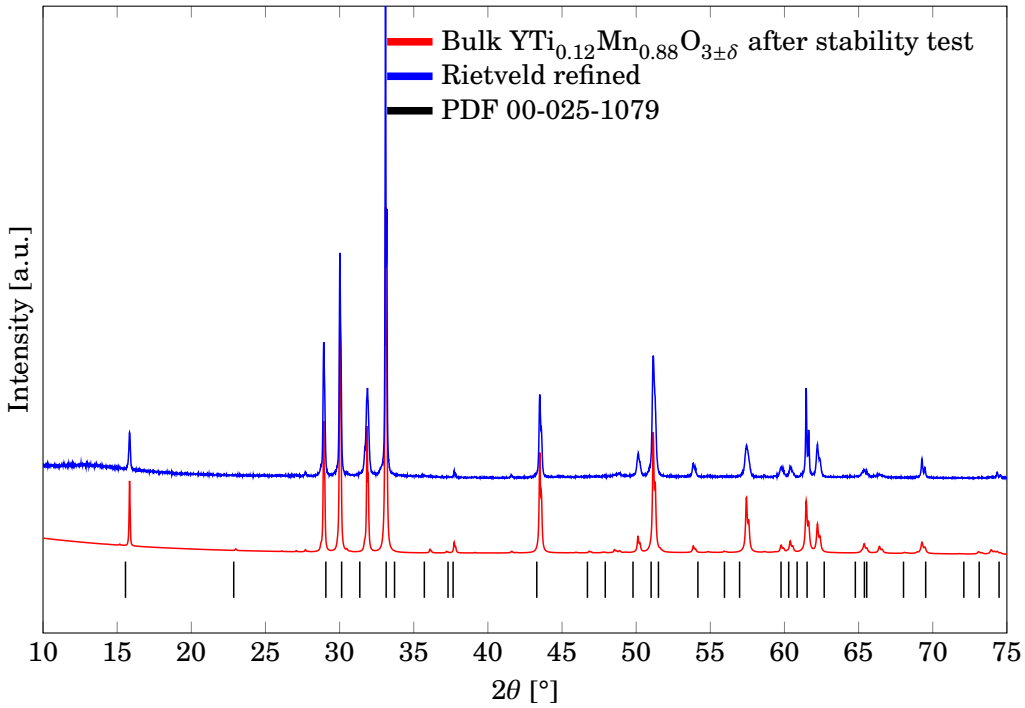

Figure E.2: Bulk $YTi_{0.12}Mn_{0.88}O_{3\pm\delta}$ after stability test

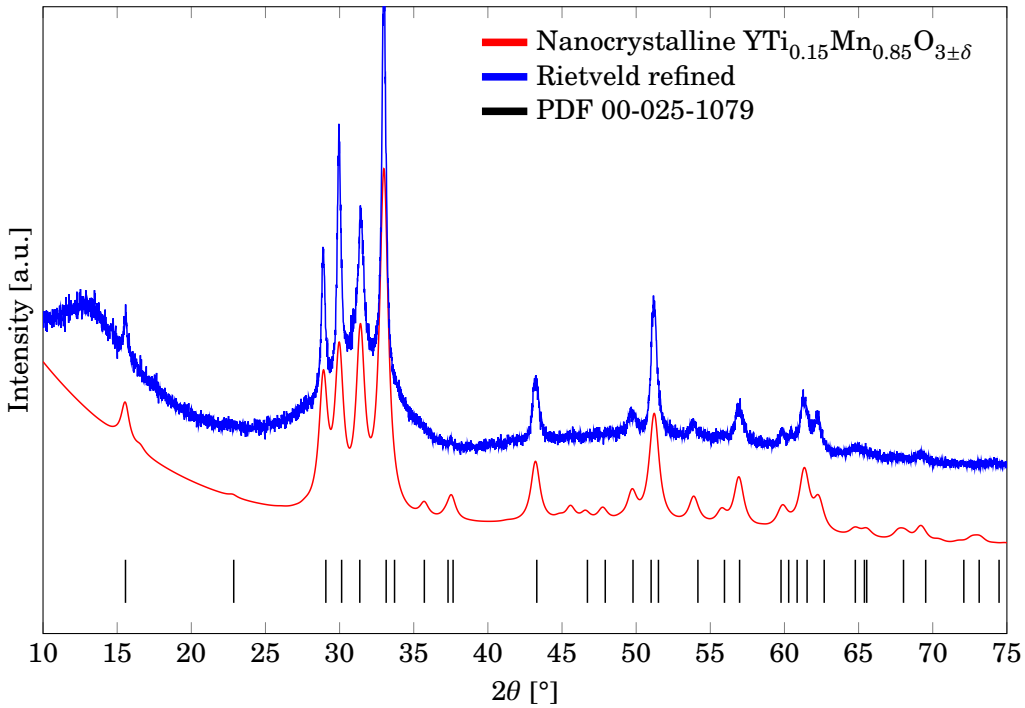

Figure E.3: Nanocrystalline $YTi_{0.15}Mn_{0.85}O_{3\pm\delta}$

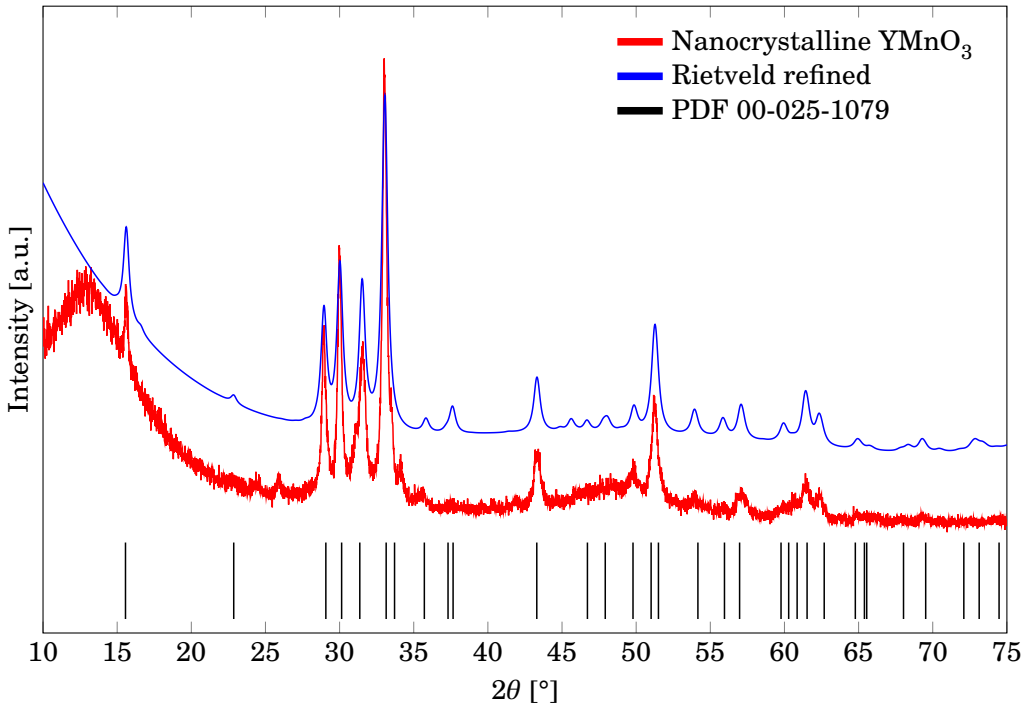

Figure E.4: Nanocrystalline $YMnO_3$

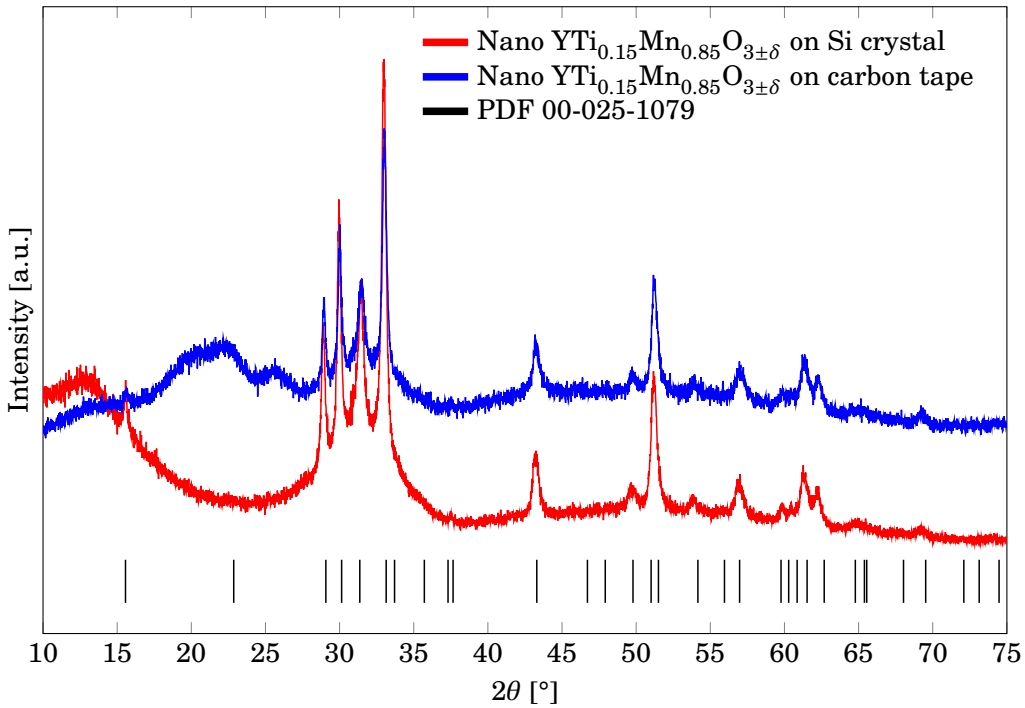

Figure E.5: Nanocrystalline $YMn_{1-x}Ti_xO_{3\pm\delta}$ on Si-single crystal compared to on carbon tape

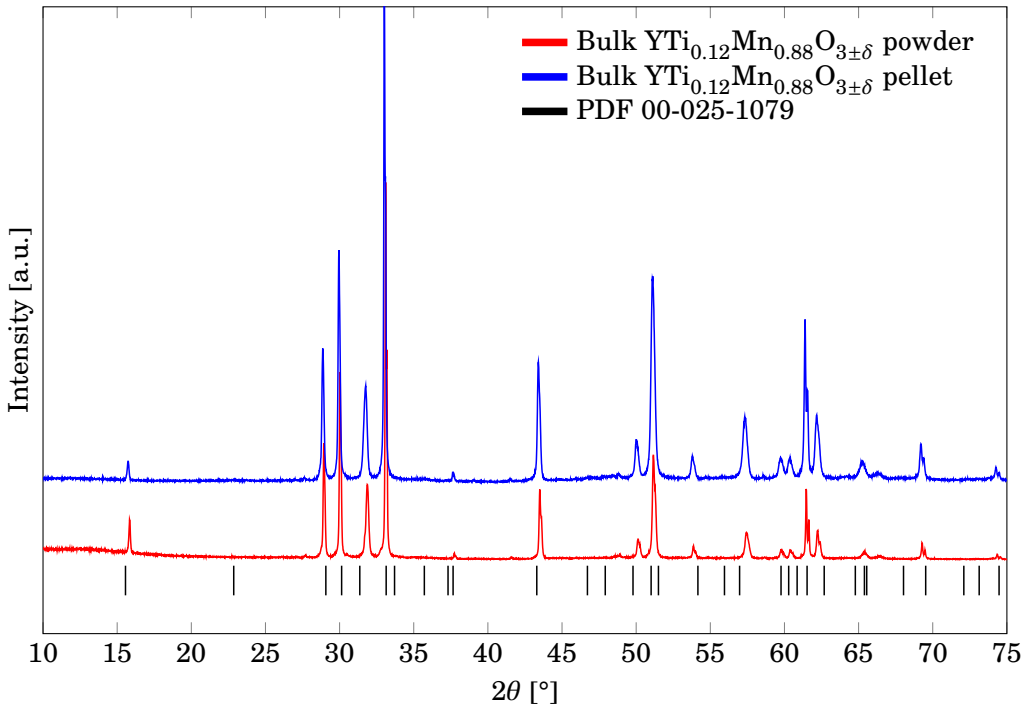

Figure E.6: Bulk $YTi_{0.12}Mn_{0.88}O_{3\pm\delta}$ in the form of pellet and disc. The samples were from the same batch. The disc was scanned with a constant 6mm illuminated area by mistake, resulting in higher intensity at high 2θ.

Appendix F

Matlab scripts

F.1 Subtraction of background current

```
clear all
close all
clc

r = [10 25 50 100 200];
n = length(r);
MC = cell(1,n);
YM = cell(1,n);
subtr=cell(1,n);

x=5;
y=6;
%Subtract MC
for i=1:n
    MCfile = strcat('p04m14_',num2str(r(i)),'mvsMC.txt');
    YMfile = strcat('p04m14_',num2str(r(i)),'mvsYM.txt');

    MC{i} = load(MCfile);
    YM{i} = load(YMfile);

    [row,col] = size(YM{i});

    for j=1:2:col-1
       subtr{i}(:,j)   = YM{i}(:,j);
       subtr{i}(:,j+1) = YM{i}(:,j+1) - MC{i}(:,j+1);
    end

    figure(1)
    plot(subtr{i}(:,x),subtr{i}(:,y));
    hold on

    dlmwrite(strcat(num2str(r(i)),'subtr.txt'),subtr{i},'\t');
end
```

F.2 Separation of faradic and non-faradic currents

```
%Clear everything
clear all
```

```
close all
clc
format long

%This script will separate faradic and non-faradic currents based on the
%equation I =a*sqrt(v) + b*v

%Sweep rates
rates =[2 10 15 25 50 100 200 500];
%Square root of sweep rates
rootV=sqrt(rates);
%Number of rates and vector 1 to number of rates
n = length(rates);
m=1:n;

%Load data from file
data=load('CurvesNoheader.txt');

%Find number of rows and columns
[row,col]=size(data);
%Columns x corresponding to potential E and y to current I
x = 1:2:col-1;
y=2:2:col;

%Extract potentials and currents
E = data(:,x);
I = data(:,y);

%Preallocate for speed I/sqrt(v(
IrootV=zeros(row,n);

%Preallocate coefficients a and b in (I/sqrt(v) = a + b*sqrt(v)
coeff = zeros(row,2);


%Create matrice for K-values K = (b/a)*sqrt(v)
Kmat = zeros(row,n);

%for each sweep rate
for i=m;
    %Calculate I/sqrt(v)
    IrootV(:,i)= abs(I(:,i))./rootV(i);
end

    %For each point on the curve
for j=1:row
%    Calculate coeffisients from linear regression of I/sqrt(v) =
%    k1*sqrt(v) k2 = capacitive + faradic
     coeff(j,:) = polyfit(rootV,IrootV(j,:),1);
     %Calculate the K-value for each point on each curve
     Kmat(j,m) = (coeff(j,1)/coeff(j,2))*rootV(m);
end

%Preallocate faradic and capacitive currents
Icap=zeros(row,n);
Ifar=zeros(row,n);

%Headers for the output-file
headers=cell(1,3*n);

%Preallocate data for file
outdata=zeros(row,3*n);
```

```
%insert potentials
outdata(:,1:n)=E;

%For each sweep rate
for i=m;
    %For each point on the curve
    for j=1:row
        %Calculate K
        K = Kmat(j,i);

        %Calculate currents
        Icap(j,i) = I(j,i)*K/(K+1);
        Ifar(j,i) =I(j,i)*(1-K/(K+1));
    end

    %Visualize to check calculations
figure(1)
subplot(2,4,i);
hold on
plot(E(:,i),I(:,i),'b')
ylim([min(I(:,i)),max(I(:,i))]);
plot(E(:,i),Icap(:,i),'r')
plot(E(:,i),Ifar(:,i),'m')
legend('Experimental','Capacitive','Faradic','Location','best')
title(num2str(rates(i)))

%Create headers for outdata file
headers{i} = strcat('E',num2str(rates(i)));
headers{i+n}    = strcat('Ifar',num2str(rates(i)));
headers{i+2*n}    = strcat('Icap',num2str(rates(i)));
end

%Put currents in out-data
outdata(:,(n+1):(2*n))=Ifar;
outdata(:,(2*n+1):(3*n))=Icap;

%Check that calculations are correct
%Dividing Ifar/sqrt(rates) should make all the curves equal. Icap/rates is
%the same.

Inorm=outdata;
j=1;
for i=(n+1):2*n
Inorm(:,i) = outdata(:,i)/rootV(j);
j=j+1;
end
j=1;
for i=(2*n+1):3*n
Inorm(:,i) = outdata(:,i)/rates(j);
j=j+1;
end

%Write with headers for pgfplots to read
HeaderWrite('IrootV.txt',headers,outdata);

%write without headers for matlab to read
dlmwrite('IrootVNoheader.txt',outdata,'\t');
```

Appendix G

Order confirmation mesoporous carbon ST8

SIGMA-ALDRICH®

sigma-aldrich.com

c/o Aker Brygge Business Center PB 1433 Vika
0115 Oslo Tlf : 23 17 60 00
Fax : +47 2317 6050

ORDREBEKREFTELSE

NTNU
N-7491 TRONDHEIM

ORDRENUMMER: 8019574445
Dato: 01.06.2015
Kundenummer: 35261506
Organisasjonsnummer:

Side: 1 / 2

Deres referanse: N1535952 av 01.06.2015

Fax No:
E-post: dehlia.e.brennhaugen@ntnu.no
https://www.sigmaaldrich.com/webapp/wcs/stores/servlet/GetOrderDetails?storeId=11001&langId=-1&salesOrderNumber=8019574445

Takk for ordren. Se nedenfor for priser og leveringstider.

Posisjon	Produktreferanse	Rabatt	Antall	Enhetspris	Totalpris	MVA	Deres ref.
000010	702102-5G		EA	NOK	NOK		
- 1							
CARBON, MESOPOROUS, HYDROPHOBIC PORE SU			1	1.619,25 /EA	1.619,25	25,0	
Estimert leveringsdato		07.08.2015	1				

OVERSIKT OMKOSTNINGER
TOTAL OMKOSTNINGER 0,00 NOK

MVA TOTALT
Utgående mva 25,0 % - Total verdi: 1.619,25 x 25,0 % 404,81 NOK

Contact person / Caller: . .

Varene vil bli levert til følgende adresse:
NTNU
KJEMIBLOKK 2, ROM 134
--
BRENNHAUGEN, DEHLIA EIDE
SEM SÆLANDS VEI 12
N-7034 TRONDHEIM

Betalingsbetingelser: Netto 30 dager fra fakturadato

Overføres..... 1.619,25 NOK